The Dissertation Committee for Vivek Subramanian Certifies that this is the approved version of the following dissertation:

Envelope Tracking Integral Equation Based Hybrid Electromagnetic Circuit Simulators

Committee:

Ali Yılmaz, Supervisor

Dean Neikirk

Hao Ling

Andrea Alu

Swagato Chakraborty

Envelope Tracking Integral Equation Based Hybrid Electromagnetic Circuit Simulators

by

Vivek Subramanian, B.E., M. Tech.

Dissertation

Presented to the Faculty of the Graduate School of

The University of Texas at Austin

in Partial Fulfillment

of the Requirements

for the Degree of

Doctor of Philosophy

The University of Texas at Austin

December 2016

Dedication

Dedicated to

Amma, Appa, Sadhguru, Adi Yogi and Bhagwa Dhwaj

Acknowledgements

I want to take this opportunity to thank the people who have helped in making this dissertation happen. I thank my dissertation committee members for their technical discussions and their time. I also thank TACC for providing the necessary computing resources and software support that made this dissertation possible. I thank Dr. Kiran Gullapalli for sharing his experiences and insights about harmonic balance simulations and device modeling for envelope tracking simulators.

I am indebted to Prof. Dean Neikirk for his empathy and for sharing his wisdom during the course of the work. I also thank him for introducing me to Dr. Kiran Gullapalli. I thank Prof. Hao Ling for his diligent and a conscientious approach at my work and needs. I thank Prof. Andrea Alu for being flexible and accommodating. I thank Dr. Swagato Chakraborty for imparting his industry perspective and experience.

I would like to acknowledge Dr. Jaideva Goswami for motivating me to pursue this work in the first place.

I am indebted to my friends Dr. Praveenkumar Pasupathy and Dr. Melissa Popowski for their constant reassurance and being the safety net I could always rely on. I also thank them for putting me up in their home and practically caretaking me over the last year. Praveen and Melissa, without your emotional and logistical support, I couldn't have finished this work successfully.

I thank my fellow group members Dr. Mingfeng Wu, Fangzhou Wei, Dr. Kai Yang, Dr. Guneet Kaur, Dr. Tahir Malas, Cemil Geyik, Jackson Massey, Chang Liu, Anton Menshov and Dr. Yaniv Brick for the meaningful relationships we had developed over the past years. I especially thank Dr. Guneet Kaur for all her assistance and support

which contribute greatly to this work. I thank .Dr. Yaniv Brick for his approachability, caring and constant encouragement. I thank Dr. Jason Soric for our conversations that helped me gain a broader perspective.

I thank my friends Dr. Parag Singla, Dr. Manohar Shamaiah, Dr. Vaidyanathan Krishnamurthy, Sunil Kowlgi, Saurabh Sardeshpande, Tanuj Trivedi, Raghunandan K Ranganathan, Somsubhra Barik, and Akhil Kulkarni for their support through the duration of the work.

I thank my cousin Rajesh Neelakandan for always providing the bigger picture and bringing a "real life" perspective. Finally, but most importantly, I am greatly indebted to my *Appa* N Subramanian and *Amma* S Thylambal for their sacrifices and care. Appa and Amma, it has been the strength and backing you have given me that has helped me throughout my life. I thank them for letting me do what I wanted and the care and meticulous efforts to not distract me from this research work over the last 7 years.

Envelope Tracking Integral Equation Based Hybrid Electromagnetic Circuit Simulators

Vivek Subramanian, Ph.D.

The University of Texas at Austin, 2016

Supervisor: Ali E. Yılmaz

This dissertation presents envelope-tracking hybrid field-circuit simulator for efficiently analyzing narrowband scattering from distributed structures loaded with nonlinear devices. The simulator models the interactions of fields with distributed structures and lumped elements by coupling and simultaneously solving the electric field integral equation and Kirchhoff's equations, respectively. The coupled nonlinear system of equations is iteratively solved by a time marching scheme that represents the fields, voltages, and currents of interest (signals) as a truncated series of harmonic sinusoids (carriers) multiplied with complex-valued time-varying coefficients (envelopes). Unlike time-domain simulators, which sample the signals at a rate proportional to their maximum frequency content, the proposed envelope-tracking simulator samples the envelopes at a rate proportional to their maximum bandwidth; thus, it requires significantly fewer time steps when solving narrowband problems. Moreover, the envelope-tracking simulator is generally more accurate than its time-domain counterpart because of smaller integration and interpolation errors. Numerical results demonstrate that the proposed simulator improves the tradeoff between accuracy and computational cost, especially when analyzing distributed structures excited by narrowband signals

or/and loaded with weakly nonlinear devices. Although the Fourier envelope simulator uses smaller number of time steps, there are other issues relating to the Fourier envelope simulator which are addressed in this thesis: (i) lumped element models that relate voltage envelopes and current envelopes for nonlinear elements are generally unavailable and the approximations used in the simulator to find them are inaccurate for broader band excitations. Higher order interpolation schemes were used in this dissertation to improve the accuracy of these approximations. Numerical results that demonstrate the ability to solve for problems with broader bandwidth of excitation are presented. (ii) As in its time-domain counterpart, adaptive integral method is used to reduce the computational cost of the simulator thus enabling the simulation of larger problems and (iii) Sparse preconditioners are used to improve the convergence of the solution algorithms. Finally, the Fourier envelope method is extended to the analysis of infinitely periodic arrays containing lumped nonlinear loads. Numerical results are presented to highlight the .features of this algorithm.

Table of Contents

LIST OF TABLES

LIST OF FIGURES

CHAPTER 1

INTRODUCTION

Electrically large structures loaded with nonlinear devices are becoming increasingly common in electromagnetic engineering; e.g., radio-frequency identification (RFID) tags [1] , phased array radar transmitter and receiver systems used in lane change avoidance/ collision avoidance vehicular systems [2], front-end of radio communication systems composed of antennas, mixers, low-noise amplifiers etc. [3], sub-millimeter wave signal sources and detectors [4], [5], all employ nonlinear loads, typically to increase power applied, increase bandwidth (modulate/demodulate) or enable frequency tuning [6], [7]. Efficient methods are needed to predict the performance of nonlinearly loaded electromagnetic (EM) modules and to improve their computer-aided design. In order to adhere with the strict spectrum/channel restrictions, most of these designs are typically mildly nonlinear and narrowband in frequency. This dissertation is an attempt to improve the analysis methods used in the computer-aided design of these structures.

1.1. PORT MODEL VS HYBRID EM-CIRCUIT SIMULATIONS

The dominant paradigm used to analyze these hybrid modules is "port extraction" [8]–[17]. In this approach, the structure of interest (Fig. 1.1(a)) is decomposed into N_{D} nonlinear circuits connected to an $N_{\mathrm{P}} = N_{\mathrm{D}} + N_{\mathrm{imp}}$ port linear system — one port for each of the N_{D} lumped loads and one port for each of the N_{imp} independent impressed source/plane-wave excitation of interest [9]; multiport network parameters relating the signals at the ports are extracted using a pure EM simulator (Fig 1.1(b)); these parameters [10]–[12] or their reduced-order models [13]–[17] are connected to the lumped-circuit models of the devices; and the resulting system is analyzed by a pure circuit (CKT) simulator (solves a nonlinear system of equations) (Fig 1.1(c)). Up to N_{P} EM

simulations (each simulation solves a linear system of equations) are needed to extract all the multiport network parameters and the computational costs for extracting these parameters are typically much higher than analyzing the equivalent system with a CKT simulator because, typically, EM system of equations has larger number of unknowns than the CKT system of equations.

An alternative paradigm is the "hybrid EM-CKT simulation" approach [18]–[30]. Here, the structure of interest is represented as N_{D} nonlinear lumped-circuit models of devices connected to an EM module at N_{D} ports. The EM module and devices are coupled at these N_{D} ports and analyzed simultaneously. This involves one (expensive) simulation solving a nonlinear system of equations.

The port-extraction approach is popular partly because it separates the EM and CKT simulations, which enables separate development/optimization of each simulator as

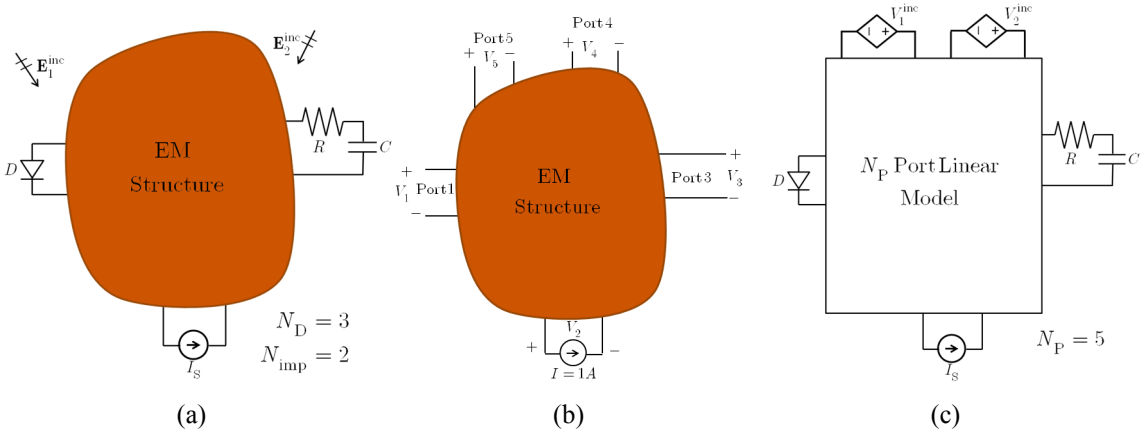

Fig. 1.1. Port-extraction approach. (a) Scattering from a nonlinearly loaded electromagnetic module. (b) One of the N_{P} scenarios analyzed by a pure EM simulator to extract multiport network parameters. (c) Equivalent system analyzed by a pure CKT simulator.

a black box, and partly because it requires the solution of a (significantly) smaller set of

unknowns/equations during nonlinear CKT analysis, which enables fast analysis and optimization of device parameters, once EM simulations are completed. There are two major disadvantages of the port-extraction approach, however, compared to hybrid EM-CKT simulation: (i) It becomes prohibitive when the number of ports increases or when the variations that affect the EM simulations are of interest, e.g., any change in the location of the devices connected to the EM module would require N_{P} (time-domain/frequency-swept, expensive) EM simulations plus one or more (cheap) CKT simulations in the port-extraction approach, compared to one or more (most expensive) hybrid EM-CKT simulations. (ii) Port-extraction approach is prone to additional errors and costs. On the one hand, these (time-domain) multiport network parameters (impulse responses) in the CKT simulation are often aliased or non-causal, which can lead to non-convergence in the nonlinear CKT simulations [15], [16]. On the other hand, ensuring the causality, stability, and passivity of reduced-order models for a prescribed bandwidth/accuracy has been an elusive goal and remains an open research problem [16], [31]. The more complex is the EM module compared to the device models, the more variations need to be studied in the EM module rather than in the devices, and the more ports there are (especially for impressed sources/plane waves), the more advantageous is the hybrid EM-CKT simulation approach compared to port-extraction approach, and vice versa.

This dissertation focuses on improving the performance of hybrid EM-CKT simulators by exploiting the mild nonlinearity and narrow bandwidth commonly encountered in these hybrid EM-CKT modules e.g., typical cell phone signals have a 30 MHz bandwidth around a 1-2 GHz carrier [3].

1.2. CLASSIFICATION OF HYBRID EM-CKT SIMULATORS

Existing hybrid EM-CKT simulators can be categorized as differential-equation [18]–[23] or integral-equation [24]–[30] simulators based on whether they formulate the EM system of equations using partial differential or integro-differential EM equations and solve them for fields or currents. Differential-equation based simulators either discretize the Maxwell's equations using central-difference/backward difference approximations for the space-time derivatives [18]–[20] or use variational methods to obtain and minimize an error function [21]–[23]. Integral-equation based simulators formulate and solve an integral equation by applying EM equivalence principles and enforcing boundary conditions [24]–[30].

Hybrid EM-CKT simulators can also be categorized as *frequency-domain (harmonic balance)* [26], [27] or *time-domain* [18]–[25] simulators based on their temporal discretization method. In time-domain EM-CKT simulators, the signals (fields, currents, voltages) of interest are expressed in terms of their temporal samples using local interpolants (sub-domain temporal basis functions), the governing equations are formulated in terms of these samples, and these equations are solved for the sample values - one set of samples at a time by time marching [18]–[25] . In harmonic-balance EM-CKT simulators, the signals are expanded using a truncated Fourier series (entire-domain temporal basis functions), the governing equations are formulated in terms of the series coefficients, and these equations are solved for the coefficients simultaneously [26], [27]. It is well known that time-domain (harmonic-balance) simulators are more suitable for analyzing transient (steady-state) responses due to broadband (single-frequency) signal sources [32]–[34].

Neither time-domain nor harmonic-balance simulators are suitable, however, for analyzing transient or steady-state responses due to narrowband sources that generate narrow bandwidth modulated signals commonly encountered in electromagnetic engineering; On the one hand, time-domain EM-CKT simulators are inefficient: The time step size used by these simulators must be inversely proportional to the maximum frequency present in the signals according to the Nyquist sampling theorem, whereas the duration for which the signals are significant (the duration of the analysis) is inversely proportional to the bandwidth of the signals; thus, the narrower is the bandwidth of the modulation, the more time steps they require and the less efficient they become [35]. On the other hand, harmonic balance EM-CKT simulators are inapplicable: Existing single-tone methods [26], [27] can only account for the carrier frequency and its harmonics and not for the modulation; moreover, even if these methods are extended to perform multi-tone analysis similar to pure CKT solvers [36], [37], their costs would increase and become prohibitive as the number of frequencies in the analysis increases.

1.3. ENVELOPE TRACKING SIMULATORS

A hybrid EM-CKT simulator that is effective for finding system responses due to narrowband sources is proposed in this research. The proposed simulator belongs to neither time-domain nor harmonic-balance categories; indeed, it should be classified into a third group: *envelope-tracking simulators*.

Various envelope-tracking methods already exist for pure EM or pure CKT simulation: (i) *Envelope-tracking EM simulators* [35], [38]–[44]. In these simulators, the fields of interest are expressed as complex-valued time-varying envelopes modulated by a sinusoidal carrier, the envelopes are represented in terms of their samples using local interpolants, and the resulting equations are solved for these samples by time marching.

The time step size is inversely proportional to the bandwidth of the fields, which makes the simulators potentially very efficient for narrowband excitations. There are complications for envelope-tracking EM simulators, however, because the spatial discretization must still resolve the minimum wavelength in the original fields. This implies that explicit time-marching methods, which are limited by the Courant-Friedrisch-Levy constraint, must still use very small time steps and do not benefit significantly from envelope tracking [39], [40]. Indeed, implicit time-marching solvers must be used for EM simulators to take advantage of envelope tracking [38], [41]–[44].

(ii) *Fourier-envelope CKT simulators* [45]–[50] . In these simulators, multiple envelopes are used to express the voltages/currents of interest because nonlinear circuit elements force these signals to have significant components at various bands in the frequency spectrum. These simulators target the prevalent case for narrowband modulated signals, where the signal components are primarily in the frequency band around a fundamental carrier frequency and in various other bands around frequencies that are integer multiples of this carrier frequency. Thus, in Fourier-envelope CKT simulators, the signals of interest are expressed as a truncated series of harmonic sinusoids multiplied with envelopes. Each of the envelopes are sampled using a common time step size that is inversely proportional to the maximum bandwidth around all the harmonic frequencies of interest, Kirchhoff's laws are enforced in terms of these samples, and the resulting nonlinear equations are solved for the sample values at each time step, one time step at a time. However, there is an issue similar to the one in harmonic balance methods — when nonlinear loads are modeled, the formulas that relate the envelopes of currents through nonlinear CKT elements to the envelopes of voltages across them are generally unavailable in closed form; thus, these formulas must be approximated by using existing time-domain CKT element models that relate currents through nonlinear elements to the

voltages across them. This makes the implementation not straightforward and special techniques need to be used to approximate the nonlinear currents and the Jacobian entries [45]–[50].

1.4. MAJOR CONTRIBUTIONS OF THIS DISSERTATION

This dissertation introduces novel envelope-tracking integral-equation based hybrid EM-CKT simulators which can perform efficient and accurate analysis of nonlinearly loaded electrically large structures. The major contributions are described in the following subsections.

1.4.1. Hybrid EM-CKT Simulator for Nonlinearly loaded Wires

A hybrid EM-CKT simulator is developed for the analysis of nonlinearly loaded wire antennas and wire antenna arrays. Just like Fourier-envelope CKT simulators, in the proposed simulator, the relevant signals are represented as truncated series of harmonic sinusoids modulated by complex envelopes (N_{H} terms). An EM system of equations governing the field interactions with the wire is obtained in three steps: (i) A thin-wire electric-field integral-equation is formulated in terms of the envelopes of the current on the wire. (ii) Each current envelope is sampled at times $\Delta t,\ldots,N_{\mathrm{T}}\Delta t$ and expanded using N_{EM} spatial basis functions with unknown coefficients. The unknown coefficients at time $l\Delta t$ are stored in a $N_{\mathrm{H}}N_{\mathrm{EM}}$ sized vector. (iii) The resulting equation is converted to a set of $N_{\mathrm{H}}N_{\mathrm{EM}}$ equations by Galerkin testing it at times $\Delta t,\ldots,N_{\mathrm{T}}\Delta t$. A CKT system of equations governing the device model is also obtained in three steps: (i) Kirchhoff's laws are applied through modified nodal analysis [45]–[51] to relate the envelopes of the node voltages and branch currents. (ii) The unknown envelopes of the N_{CKT} node voltages and branch currents of voltage sources are sampled at the same time instants as the wire current; the samples at time $l\Delta t$ are stored in $N_{\mathrm{H}}N_{\mathrm{CKT}}$ sized

vector. (iii) The differential equations relating branch currents to node voltages are converted to a set of $N_{\mathrm{H}}N_{\mathrm{CKT}}$ nonlinear equations by using trapezoidal integration at times $\Delta t,\ldots,N_{\mathrm{T}}\Delta t$ [45]–[51]. The two systems of equations are coupled using the lumped port model described in [24], [25], which enforces the integral of the electric field across the port to be equal to the voltage drop between its two terminals and the current through the device terminals to be equal to the wire current at the port. This yields a nonlinear system of equations which is solved using a multi-dimensional Newton's algorithm. The formulas relating the envelopes of currents through nonlinear CKT elements to the envelopes of voltages across them are approximated using a three step procedure: At each time step l (i) approximate the (unavailable) voltage samples at several time instants between the present and the previous time step by interpolating the (available) voltage-envelope samples, (ii) substitute these (approximate) voltage samples in CKT element models to find current samples at the same time instants, and (iii) use these (inaccurate) current samples to approximate the current-envelope samples at time step l [45]-[51]. For narrowband problems, this discretization of the integral equations and their nonlinear solution requires $O(N_{\mathrm{H}}[N_{\mathrm{EM}}^2+N_{\mathrm{CKT}}])$ computations and $O(N_{\mathrm{H}}[N_{\mathrm{EM}}^2+N_{\mathrm{CKT}}])$ bytes to fill and store the impedance matrices. The nonlinear solution algorithm requires $O(N_{\mathrm{T}}\bar{N}_{\mathrm{N}}\bar{N}_{\mathrm{I}}[N_{\mathrm{H}}N_{\mathrm{EM}}^2+N_{\mathrm{H}}^2N_{\mathrm{CKT}}])$ computations. Here, $\bar{N}_{\mathrm{N}}$ and $\bar{N}_{\mathrm{I}}$ are respectively the average number of Newton iterations per time step and the average number of iterations required by the iterative linear solver per Newton iteration per time step. Unlike time-domain simulators, which sample the signals at a rate proportional to their maximum frequency content, the proposed envelope-tracking simulator samples the envelopes at a rate proportional to their maximum bandwidth; thus, it requires significantly fewer time steps N_{T} when solving narrowband problems making it more efficient than its time-domain counterparts. Moreover, the envelope-tracking

simulator is generally more accurate than its time-domain counterpart because of smaller integration and interpolation errors [52].

1.4.2. Extension of Hybrid EM-CKT Simulator to Broader-band Excitations

When excited with broad-band excitations, the aforementioned three step approximation relating the envelope of the nonlinear CKT currents to the CKT voltage become invalid and cause the nonlinear solution to fail as the bandwidth broadens. Novel temporal sampling and interpolation schemes are implemented in the procedure for finding the nonlinear current envelopes from voltage envelopes. These schemes enable broader band simulations to be performed by expanding the range of validity of expressions that relate the envelopes of currents through nonlinear circuit elements to the envelopes of the voltages across them. Moreover, these schemes do not significantly increase the cost of the hybrid EM-CKT simulation.

1.4.3. Hybrid EM-CKT Simulator for Microwave Circuits and Antennas

Next, the EM part of the simulator is extended to include perfect electrically conducting (PEC) and dielectric bodies. Here, similar to the wire antenna case, (i) the surface and volume EFIEs are formulated in terms of the envelopes, (ii) the envelopes of the surface currents on perfectly electrically conducting (PEC) surfaces and envelopes of polarization currents in the dielectric body are sampled at time-instants $\Delta t,\ldots,N_{\mathrm{T}}\Delta t$ and discretized in space using N_{EM} divergence-conforming sub-domain basis functions, and (iii) the resulting equations are Galerkin tested at times $\Delta t,\ldots,N_{\mathrm{T}}\Delta t$ to obtain a block system of equations. The CKT equations and the lumped model used for the coupling of EM and CKT equations are identical to the hybrid EM-CKT simulator for the wire case.

A finite-gap non-radiating port model is introduced to accurately model the EM scattering from the port where the EM and CKT are connected. These ports are modeled as finite rectangular gaps. The current continuity across the port is assumed (the currents in the port gap are not radiated) and the line integral of the E-field in the gap is enforced to be equal to the port voltage.

For narrowband problems, the computational cost requirement is also identical to the previous case (typically, with a much larger N_{EM}). Just as for time-domain EM-CKT simulators [24], [25], this computational cost is prohibitive and fast methods are needed to alleviate it. In this dissertation, a Fourier-Envelope Adaptive Integral Method (FE-AIM) is implemented to approximate the EM equations and reduce the computational cost requirement of these problems by exploiting the translational invariance of the Green function. Here, An extension of the envelope tracking AIM (ET-AIM) scheme [52].is implemented, i.e. FE-AIM approximates the N_{H} harmonics instead of just one carrier as in ET-AIM scheme. As in the case of its time-domain [25], [53] and frequency domain [54] counterparts, this is achieved by using a regular auxiliary grid covering the EM module (with N_{C} points). For a given source point, each envelope of the scattered field for observer point beyond a given distance is approximated by using equivalent point sources at the auxiliary grid points and radiating them using the space-time invariant Green function. This result in a block-Toeplitz matrix which can be computed efficiently using 4-D space-time FFTs. For narrowband problems, AIM will require $O(N_{\mathrm{H}}(N_{\mathrm{C}}+N_{\mathrm{EM}}))$ computations to compute the unique entries of the necessary matrices and $O(N_{\mathrm{H}}(N_{\mathrm{C}}+N_{\mathrm{EM}}))$ bytes to store these entries [52]. As most of the EM-CKT modules are planar, AIM method will require $O(N_{\mathrm{T}}\bar{N}_{\mathrm{N}}\bar{N}_{\mathrm{I}}[N_{\mathrm{H}}N_{\mathrm{C}}\log N_{\mathrm{C}}+N_{\mathrm{H}}^{2}N_{\mathrm{CKT}}])$ computations for the nonlinear solution

algorithm. Here again, $\bar{N}_{\mathrm{N}}$ and $\bar{N}_{\mathrm{I}}$ are the average number of Newton iterations per time step and the average number of iterative solve iterations per Newton iteration, respectively. Sparse near-field preconditioners [55]–[57] are implemented to improve the convergence of the nonlinear solution algorithm. Although these preconditioners do a lot more computations at each iteration compared to the diagonal preconditioner, they have a lot lesser iterations. Thereby, reducing the overall computational cost.

1.4.4. Hybrid EM-CKT Simulator for Nonlinear Periodic Structures

Large arrays of nonlinearly loaded EM modules are common in phased arrays, frequency selective surfaces and metasurfaces [6], [7]. Efficient analysis can be performed by approximating these arrays as infinite arrays. Next, envelope-tracking hybrid EM-CKT simulator is extended for analyzing scattering from infinite nonlinearly loaded periodic structures excited by an incident plane-wave. The signals (fields, currents, voltages) in any cell are temporally shifted copies of those in a reference cell. The EM equations used in the hybrid simulator are obtained using an envelope tracking integral-equation technique equivalent of the time-domain method published in [58]: Surface-volume EFIE are formulated in terms of envelopes of the unknown currents in the reference cell using the periodic Green function. The unknown N_{H} envelopes of currents are discretized using $N_{\mathrm{EM}}N_{\mathrm{T}}$ space-time basis functions and the resulting equations are Galerkin tested in space at N_{T} different time instants. In the case of obliquely incident plane wave, future values of the envelopes of current are needed to find the envelopes of the scattered fields on the reference cell at each time instant, which requires the use of an extrapolation scheme. To reduce the number of future samples of currents that are extrapolated, the testing instants and the temporal basis functions are time shifted (depending on the location of the spatial basis functions in the cell) [58];

moreover, bandlimited temporal basis functions are used to facilitate the extrapolation scheme [59]. The CKT equations in each unit cell is independent of one other. Therefore, the CKT equations and the coupling of EM and CKT equations are identical to the envelope tracking hybrid simulators in the previous sections.

1.4.5. Envelope-Tracking AIM for lossy medium

In geophysical applications, the EM modules are in lossy (conductive) medium. This thesis presents a preliminary work towards that end. The transient scattering from PEC in conductive backgrounds is modeled using an ET-AIM simulator. Further research needs to be performed to make it useful for modeling subsurface environments.

1.5. ORGANIZATION OF THE THESIS

The rest of this dissertation is organized as follows. Chapter 2 presents in detail the CKT component of all the simulators described in Chapters 3-6. Chapter 3 presents the hybrid EM-CKT for nonlinearly loaded wires. The formulation illustrates: (i) the envelope-tracking solution of the wire integral equation using the classical MOT scheme, (ii) coupling of CKT and EM simulators, and (iii) Newton solution of the resulting equations. Numerical results validate and show the advantages of the proposed simulator over their time-domain counterparts. Chapter 4 presents an increased accuracy nonlinear solution algorithm for broader-band excitations. Chapter 5 presents the extension of the hybrid EM-CKT simulator to model the planar microwave circuits and antennas. Chapter 5 illustrates: (i) the envelope-tracking integral-equation solution using the classical MOT method for surface/volume integral equation arising in PEC/lossless dielectric volumes, (ii) new port model for realistic models of excitations/ports, (iii) FE-AIM method acceleration, and (iv) sparse near field preconditioners for improving the convergence of the nonlinear solution algorithm. Numerical results that show the comparison between the

performance of this simulator with its time-domain counterparts and the performance of the preconditioner are presented. Chapter 6 formulates the time-domain and envelope-tracking simulator for infinitely nonlinearly loaded periodic structures and compare it with their time-domain counterparts. Chapter 7 presents an envelope tracking AIM simulator for modeling the scattering from PEC structures in conductive medium. .Chapter 8 summarizes the findings of this research and also presents the future extensions of this research work

CHAPTER 2

FOURIER ENVELOPE CKT SIMULATOR

This chapter describes a Fourier envelope circuit (FE-CKT) simulator that is used to model the devices connected to the EM structures. Each device is modeled as a lumped circuit that includes linear elements (resistors, inductors, and capacitors), independent voltage and current sources, and nonlinear elements (diodes, transistors etc.). Each of the lumped circuits are formulated separately using the modified nodal analysis (MNA) procedure similar to the classical time domain one [60], [61]. However, it is formulated not in terms of node voltages and branch currents but in terms of their envelopes [34], [51]. In each circuit, Kirchhoff's current laws at all circuit nodes (except one reference node) and the branch constitutive relations for voltage source branches are applied through MNA to relate the envelopes of the branch currents to the envelopes of the node voltages (and its time derivative) in the circuit. Resulting ordinary differential equations are discretized by sampling in time and a trapezoidal integration scheme is used to approximate the differential equation to a nonlinear system of equations at each time step. The nonlinear system of equations are solved using a Newton-Raphson scheme.

The MNA and its numerical formulation for a lumped circuit is presented in section 2.1 and the nonlinear solution scheme is presented in section 2.2. Numerical examples describing the capability of the simulator for analysis of circuits involving various passive and active components is presented in Section 2.3. Finally, the extension of this formulation to the concurrent analysis multiple circuits is presented in Section 2.4.

2.1 MNA FORMULATION

Consider a circuit consisting of N_{nod} nodes, N_{b} branches, N_{vs} voltage sources and N_{is} current sources. One of the nodes in the circuit is identified as the reference node, numbered as the zeroth node, and assigned zero potential. For notational simplicity, let the first branch numbers be assigned to the branches containing voltage sources. The instantaneous voltages at all the non-reference nodes, currents through each branch and the source values are expanded using a truncated series with N_{H} terms (harmonics):

$$\begin{aligned}
V_n(t) &\cong \mathrm{Re}\left(\sum_{h=0}^{N_{\mathrm{H}}-1} \tilde{V}_n^h(t) e^{jh\omega_0 t}\right) \quad \text{for } n=1,\ldots,N_{\mathrm{nod}}-1 N_{\mathrm{vs}} \\
I_b(t) &\cong \mathrm{Re}\left(\sum_{h=0}^{N_{\mathrm{H}}-1} \tilde{I}_b^h(t) e^{jh\omega_0 t}\right) \quad \text{for } b=1,\ldots,N_{\mathrm{b}} \\
VS_i(t) &\cong \mathrm{Re}\left(\sum_{h=0}^{N_{\mathrm{H}}-1} \widetilde{VS}_i^h(t) e^{jh\omega_0 t}\right) \text{ for } i=1,\ldots,N_{\mathrm{vs}} \\
IS_i(t) &\cong \mathrm{Re}\left(\sum_{h=0}^{N_{\mathrm{H}}-1} \widetilde{IS}_i^h(t) e^{jh\omega_0 t}\right) \text{ for } i=1,\ldots,N_{\mathrm{is}}
\end{aligned} \tag{2.1}$$

Henceforth, $\tilde{V}_n^h$, $\tilde{I}_b^h$, $\widetilde{VS}_i^h$ and $\widetilde{IS}_i^h$ are referred to as the h^{th} envelope of the non-reference node voltages, branch currents, voltage source and current source values respectively. Note that all the envelope quantities are complex-valued except for the 0^{th} envelopes which are real-valued.

Next, some of the notations used to express quantities used in the MNA here and its nonlinear solution in Section 2.2 are described. The unknown functions that are found in the classical time-domain MNA procedure are listed in a vector i.e., voltages at the non-reference nodes and currents through voltage-source branches are listed in the $N_{\mathrm{CKT}} \times 1$ (where $N_{\mathrm{CKT}} = N_{\mathrm{nod}} + N_{\mathrm{vs}}$) vector $\mathbf{V} = [V_1(t),\ldots, V_{N_{\mathrm{nod}}-1}(t), I_1(t),\ldots,I_{N_{\mathrm{vs}}}(t)]^T$. The $N_{\mathrm{H}} N_{\mathrm{CKT}}$ envelopes of these functions are the unknowns in this FE-CKT MNA procedure; i.e. in the following, they are identified using the vectors

$\tilde{\mathbf{V}}^h = [\tilde{V}_1^h(t),\ldots,\tilde{V}_{N_{\text{nod}}-1}^h(t),\tilde{I}_1^h(t),\ldots,\tilde{I}_{N_{\text{vs}}}^h(t)]^T$ and their concatenation $\tilde{\mathbf{V}}[hN_{\text{CKT}}+1 : (h+1)N_{\text{CKT}}] = \tilde{\mathbf{V}}^h[1 : N_{\text{CKT}}]$ for $h = 0,\ldots,N_{\text{H}}-1$ that contains all the envelopes. To formulate the MNA procedure concisely, the currents through the nonlinear elements are listed in another vector of functions $\mathbf{I}^{\text{nl}} = [I_1^{\text{nl}}(t),\ldots, I_{N_{\text{nod}}-1}^{\text{nl}}(t),0,\ldots,0]^T$, where $I_n^{\text{nl}}(t)$ denotes the current exiting node n through all the nonlinear elements connected to it and the vector is zero-padded such that $\mathbf{I}^{\text{nl}}$ is the same size as $\mathbf{V}$. The hth envelopes of these currents are listed in the vector $\tilde{\mathbf{I}}^{\text{nl},h} = [\tilde{I}_1^{\text{nl},h}(t),\ldots,\tilde{I}_{N_{\text{nod}}-1}^{\text{nl},h}(t),0,\ldots,0]^T$ and concatenating all N_{H} such vectors forms the vector $\tilde{\mathbf{I}}^{\text{nl}}$ where $\tilde{\mathbf{I}}^{\text{nl}}[hN_{\text{CKT}}+1 : (h+1)N_{\text{CKT}}] = \tilde{\mathbf{I}}^{\text{nl},h}[1 : N_{\text{CKT}}]$ for $h = 0,\ldots,N_{\text{H}}-1$.

To find the unknown voltage and current envelopes, Kirchhoff's current law is enforced at all the non-reference nodes, Kirchhoff's voltage law is enforced on branches containing voltage sources, and the equations governing the circuit elements are used to represent the branch currents in terms of node voltages [51]. This procedure results in $N_{\text{H}}N_{\text{CKT}}$ nonlinear ordinary differential equations.

For example, the above procedure applied to a rectifier circuit (Fig. 2.1) used for energy harvesting [62] results in the system of equations:

$$\left[\begin{array}{c|c|c} C(d_t + jh\omega_0) & 0 & -1 \\ \hline 0 & \dfrac{1}{R} & 1 \\ \hline -1 & 1 & 0 \end{array}\right]\begin{bmatrix}\tilde{V}_1^h \\ \tilde{V}_2^h \\ \tilde{I}_1^h\end{bmatrix} + \begin{bmatrix}0 \\ -\tilde{I}_3^h \\ 0\end{bmatrix} = \begin{bmatrix}0 \\ -\widetilde{IS}_1^h \\ \widetilde{VS}_1^h\end{bmatrix} \tag{2.2}$$

for $h = 0,\ldots,N_{\text{H}}-1$. Here, d_t denotes the time derivative operator, $\tilde{\mathbf{V}}^h = [\tilde{V}_1^h(t),\tilde{V}_2^h(t),\tilde{I}_1^h(t)]^T$, and $\tilde{\mathbf{I}}^{\text{nl},h} = [0,-\tilde{I}_3^h(t),0]^T$.

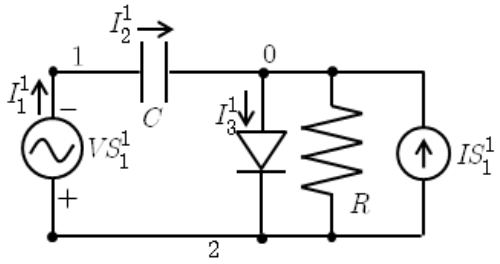

Fig. 2.1. A simple rectifier circuit that can be used for energy harvesting.

In (2.2), the hth envelope of the current through the diode must be represented as a function of all the envelopes of the voltage across it. It is important to observe that nonlinear circuit elements are commonly defined using equations that relate the (time-domain) voltage and current across them., e.g., $I_3(t) = I_{\mathrm{SD}}(\exp(-V_2(t) / V_{\mathrm{TH}}) - 1)$ for the diode in Fig. 2.1, where I_{SD} and V_{TH} are known constants. Unfortunately, such nonlinear equations do not generally yield closed-form equations that relate the envelopes; thus, the relationship among the envelopes must be estimated numerically from the time-domain expression. This procedure is detailed in Section 2.2. In general, if the current through an element is a nonlinear function of the voltage across it, then each envelope of the current will be a nonlinear function of all the envelopes of the voltage. In the rest of this document, the dependence among the envelopes is shown by using the notation $\tilde{\mathbf{I}}^{\mathrm{nl},h}(\tilde{\mathbf{V}}, t)$; similarly, the nonlinear equations that relate the (time domain) currents and voltages are expressed as $\mathbf{I}^{\mathrm{nl}}(\mathbf{V}, t)$.

To numerically solve the MNA equations, the voltage and current envelopes are sampled uniformly in time (at the same time instances used for discretizing the EM equations). Let the vectors $\tilde{\mathbf{V}}_l^{\mathrm{CKT},h} = \tilde{\mathbf{V}}^h(l\Delta t)$ denote the samples at time $l\Delta t$ of the hth envelopes of the circuit unknowns; their concatenation is denoted as $\tilde{\mathbf{V}}_l^{\mathrm{CKT}}$, which is a vector containing $N_{\mathrm{H}} N_{\mathrm{CKT}}$ numbers. To find these numbers, the trapezoidal rule is

used to approximate the equations governing the circuit elements. This is a straightforward operation for linear elements; e.g., the relevant equation, which is $\tilde{I}_2^h(t) = C(d_t + jh\omega_0)\tilde{V}_1^h(t)$, for the capacitor in Fig. 2 is approximated as

$$\tilde{I}_2^h(l\Delta t) \approx C(\frac{2}{\Delta t} + jh\omega_0)\tilde{V}_1^h(l\Delta t) - \tilde{I}_2^h([l-1]\Delta t) - C(\frac{2}{\Delta t} - jh\omega_0)\tilde{V}_1^h([l-1]\Delta t) \quad (2.3)$$

for $l = 1,\ldots,N_{\mathrm{T}}$. This equation can be interpreted as a constant impedance in parallel with a dependent current source whose values are obtained from the past samples of the envelopes. Similar equations that relate the samples at time $l\Delta t$ of the hth envelope of the current through the element to the present and past samples of the hth envelope of the voltage across and the current through the element can be formulated for all linear circuit elements. In contrast, for nonlinear elements, the samples of the hth envelope of the current through the element must be related to the present and past samples of all N_{H} envelopes of the voltage across it, e.g., $\tilde{I}_3^h(l\Delta t) \approx f(\tilde{V}_2^0(l\Delta t),...,\tilde{V}_2^{N_H-1}(l\Delta t), l\Delta t)$ for the diode in Fig. 2. Equations similar to (2.3) that relate the samples at time $l\Delta t$ of the envelopes of the current flowing through the elements to the envelopes of the present and past samples of the voltage across them for various linear and nonlinear elements are described in Appendix I. In the following, the dependence among the samples of the envelopes are highlighted by using the notation $\tilde{\mathbf{I}}_l^{\mathrm{nl},h}(\tilde{\mathbf{V}}_l^{\mathrm{CKT}})$, which denotes the samples at time $l\Delta t$ of the hth envelope of the currents through the nonlinear elements; and their concatenation is denoted as $\tilde{\mathbf{I}}_l^{\mathrm{nl}}(\tilde{\mathbf{V}}_l^{\mathrm{CKT}})$. Using this notation, the nonlinear system of algebraic equations that result from the application of trapezoidal rule in each circuit can be expressed as

$$\begin{aligned} \tilde{\mathbf{Y}}^0\tilde{\mathbf{V}}_l^{\mathrm{CKT},0} + \tilde{\mathbf{I}}_l^{\mathrm{nl},0}(\tilde{\mathbf{V}}_l^{\mathrm{CKT}}) &= \tilde{\mathbf{I}}_l^{\mathrm{CKT},0} \\ &\vdots \\ \tilde{\mathbf{Y}}^{N_{\mathrm{H}}-1}\tilde{\mathbf{V}}_l^{\mathrm{CKT},N_{\mathrm{H}}-1} + \tilde{\mathbf{I}}_l^{\mathrm{nl},N_{\mathrm{H}}-1}(\tilde{\mathbf{V}}_l^{\mathrm{CKT}}) &= \tilde{\mathbf{I}}_l^{\mathrm{CKT},N_{\mathrm{H}}-1} \end{aligned} \quad (2.4)$$

or more compactly as

$$\tilde{\mathbf{Y}}\tilde{\mathbf{V}}_l^{\mathrm{CKT}} + \tilde{\mathbf{I}}_l^{\mathrm{nl}}(\tilde{\mathbf{V}}_l^{\mathrm{CKT}}) = \tilde{\mathbf{I}}_l^{\mathrm{CKT}} \tag{2.5}$$

for $l = 1,\ldots,N_{\mathrm{T}}$. Here, the vector $\tilde{\mathbf{I}}_l^{\mathrm{CKT}}$ stores the samples at time $l\Delta t$ of the envelopes of current and voltage sources. The matrix $\tilde{\mathbf{Y}}$ is an $N_{\mathrm{H}}N_{\mathrm{CKT}} \times N_{\mathrm{H}}N_{\mathrm{CKT}}$ block-diagonal matrix that relates the samples of the envelopes of the branch currents to those of node voltages for linear elements (modified with Kirchhoff's voltage law for branches with voltage sources). Note that, the CKT equations that correspond to the different harmonics are coupled by the nonlinear current $\tilde{\mathbf{I}}_l^{\mathrm{nl}}$; thus, they must be solved for all N_{H} envelopes simultaneously at each time step.

2.2 SOLUTION OF NONLINEAR EQUATION – NEWTON RAPHSON SCHEME

The solution algorithm used in the pure Fourier envelope circuit simulator is presented here. At each time step, the Newton-Raphson algorithm is used to solve (2.5) for the vector $\tilde{\mathbf{V}}_l^{\mathrm{CKT}}$. Although the solution procedure for the proposed Fourier-envelope CKT simulator is similar to that for the time-domain CKT simulator, there are important modifications here because the unknown vector $\tilde{\mathbf{V}}_l^{\mathrm{CKT}}$ and the equations (2.5) are complex valued and closed-form equations that relate the current and voltage envelopes are generally not available for nonlinear elements. The solution procedure can be cast into five stages at each time step $l\Delta t$.

Stage 1: Compute the right hand side $\tilde{\mathbf{I}}_l$ of (2.5)

Stage 2: At each Newton iteration $p = 1,2,\ldots$, compute the residual vector $\tilde{\mathbf{r}}_{l,p-1} = \tilde{\mathbf{Y}}\tilde{\mathbf{V}}_{l,p-1}^{\mathrm{CKT}} + \tilde{\mathbf{I}}_l^{\mathrm{nl}}(\tilde{\mathbf{V}}_{l,p-1}^{\mathrm{CKT}}) - \tilde{\mathbf{I}}_l^{\mathrm{CKT}}$ using $\tilde{\mathbf{V}}_{l,p-1}^{\mathrm{CKT}}$, the solution vector guessed in the previous Newton iteration. The first guess is set to the solution at the previous time step: $\tilde{\mathbf{V}}_{l,0}^{\mathrm{CKT}} = \tilde{\mathbf{V}}_{l-1}^{\mathrm{CKT}}$. To compute the residual vector, the vectors $\tilde{\mathbf{I}}_l^{\mathrm{nl}}(\tilde{\mathbf{V}}_{l,p-1}^{\mathrm{CKT}})$ must be

evaluated, i.e., the N_{H} envelopes of the currents through nonlinear elements at time $l\Delta t$ must be evaluated given the previous guess. When closed-form expressions are not available, these samples are approximated in three steps; these are detailed next.

First, the samples of the CKT unknowns are estimated from the samples of their envelopes at $M+1$ different times $t_{l,0},...,t_{l,M}$. These estimates are denoted with $\mathbf{V}_{l,m,p-1}$, which are defined as

$$\begin{aligned}\mathbf{V}(t_{l,m}) &= \mathrm{Re}\left(\sum_{h=0}^{N_{\mathrm{H}}-1}\tilde{\mathbf{V}}^{h}(t_{l,m})e^{jh\omega_0 t_{l,m}}\right)\\ &\approx \mathrm{Re}\left(\sum_{h=0}^{N_{\mathrm{H}}-1}\tilde{\mathbf{V}}^{\mathrm{CKT},h}_{l,p-1}e^{jh\omega_0 t_{l,m}}\right)\doteq \mathbf{V}_{l,m,p-1}\end{aligned} \tag{2.6}$$

for $m=0,...,M$. Notice that the above expression does not use the correct values of the envelopes at the times of evaluation but sets them to the guessed value at time $l\Delta t$, i.e., it approximates the envelopes as piecewise constant functions. This approximation is accurate only if the envelopes are varying slowly compared to the carrier frequency; thus, it constraints the accuracy of the nonlinear solution procedure for broadband excitations and limits the proposed method to problems with relatively narrow bandwidths of interest.

Second, the nonlinear element equations are evaluated to estimate the values of the currents through the nonlinear elements at the same time instances. These are defined as $\mathbf{I}^{\mathrm{nl}}_{l,m,p-1}\doteq\mathbf{I}^{\mathrm{nl}}(\mathbf{V}_{l,m,p-1},t_{l,m})$ for $m=0,...,M$.

Third, these estimated current samples are expressed in terms of the samples of envelopes at time $l\Delta t$, i.e.,

$$\mathbf{I}^{\mathrm{nl}}_{l,m,p-1}\approx\mathrm{Re}\left(\sum_{h=0}^{N_H-1}\tilde{\mathbf{I}}^{\mathrm{nl},h}_{l}(\tilde{\mathbf{V}}^{\mathrm{CKT}}_{l,p-1})e^{jh\omega_0 t_{l,m}}\right) \tag{2.7}$$

for $m = 0,\ldots,M$. Once again, the envelopes are approximated as piecewise constant functions here. In effect, these three stages approximate both sides of the equation

$$\mathbf{I}^{\mathrm{nl}}(\mathbf{V},t) = \mathrm{Re}\left(\sum_{h=0}^{N_{\mathrm{H}}-1} \tilde{\mathbf{I}}^{\mathrm{nl},h}(\tilde{\mathbf{V}},t)e^{jh\omega_0 t}\right) \tag{2.8}$$

and enforces the (incorrect) equations

$$\begin{aligned}
\mathbf{I}^{\mathrm{nl}}(\mathbf{V}_{l,0,p-1},t_{l,0}) &\approx \mathrm{Re}\left(\sum_{h=0}^{N_H-1} \tilde{\mathbf{I}}_l^{\mathrm{nl},h}(\tilde{\mathbf{V}}_{l,p-1}^{\mathrm{CKT}})e^{jh\omega_0 t_{l,0}}\right) \\
&\vdots \\
\mathbf{I}^{\mathrm{nl}}(\mathbf{V}_{l,M,p-1},t_{l,M}) &\approx \mathrm{Re}\left(\sum_{h=0}^{N_H-1} \tilde{\mathbf{I}}_l^{\mathrm{nl},h}(\tilde{\mathbf{V}}_{l,p-1}^{\mathrm{CKT},D})e^{jh\omega_0 t_{l,M}}\right)
\end{aligned} \tag{2.9}$$

Solving these $M+1$ real-valued linear equations results in an estimate for the desired vectors $\tilde{\mathbf{I}}_l^{\mathrm{nl},0},\ldots\tilde{\mathbf{I}}_l^{\mathrm{nl},\mathrm{N_H}-1}$. Notice that in (2.9), $N_{\mathrm{H}}-1$ of the unknown samples are complex and one of them is real (that of the 0th harmonic) By choosing $M = 2N_{\mathrm{H}}-1$ and $t_{l,m} = l\Delta t - 2\pi(M-m)/(M+1)\omega_0$, (2.9) can be solved efficiently with FFTs [34], [51]. Accuracy of this procedure can be increased by employing different time sampling instants $t_{l,0},\ldots,t_{l,M}$ and higher order interpolation schemes like piecewise-linear and piecewise-quadratic functions for approximating envelopes in (2.6) and (2.8). These improvements and their implications on the bandwidth of analysis are investigated for the hybrid EM-CKT simulators and presented in Chapter 4.

Stage 3: If $\left\|\tilde{\mathbf{r}}_{l,p-1}\right\| < tol \times \left\|\tilde{\mathbf{I}}_l^{\mathrm{CKT}}\right\|$, where tol is a predefined tolerance, then set $\tilde{\mathbf{V}}_l^{\mathrm{CKT}} = \tilde{\mathbf{V}}_{l,p-1}^{\mathrm{CKT}}$ and stop the Newton iterations; else, calculate the next Newton step as follows.

Stage 4: Find the Jacobian. Because $\tilde{\mathbf{I}}^{\mathrm{nl}}$ depends on complex variables, the Jacobian must be computed with respect to the real and imaginary parts of these variables, i.e., $2N_{\mathrm{H}}^2$ matrices must be formed [51]; the entries of these matrices are

$$\begin{aligned}
\tilde{\mathbf{J}}_{l,p}^{\mathrm{Rnl},h,h'}[n,n'] &= \left.\frac{\partial \tilde{\mathbf{I}}^{\mathrm{nl},h}[n]}{\partial \operatorname{Re}\{\tilde{\mathbf{V}}^{h'}[n']\}}\right|_{\tilde{\mathbf{V}}^{h'}[n']=\tilde{\mathbf{V}}_{l,p-1}^{\mathrm{CKT},h'}[n']} \\
\tilde{\mathbf{J}}_{l,p}^{\mathrm{Inl},h,h'}[n,n'] &= \left.\frac{-\partial \tilde{\mathbf{I}}^{\mathrm{nl},h}[n]}{\partial \operatorname{Im}\{\tilde{\mathbf{V}}^{h'}[n']\}}\right|_{\tilde{\mathbf{V}}^{h'}[n']=\tilde{\mathbf{V}}_{l,p-1}^{\mathrm{CKT},h'}[n']}
\end{aligned} \tag{2.10}$$

for $n,n' = 1,\ldots,N_{\mathrm{CKT}}$ and $h,h' = 0,\ldots,N_{\mathrm{H}}-1$. Note that $\tilde{\mathbf{J}}_{l,p}^{\mathrm{Inl},h,0}$ is a null matrix because the envelope of the 0th harmonic is a real function. Similar to step 2, the entries of the Jacobian matrices are found approximately; i.e., the derivative of (2.9) rather than (2.8) is computed with respect to the real and imaginary parts of $\tilde{\mathbf{V}}_l^{\mathrm{CKT},h'}$:

$$\begin{aligned}
\mathbf{J}_{l,0,p}^{\mathrm{nl}}[n,n']\cos(h'\omega_0 t_{l,0}) &\approx \operatorname{Re}\left(\sum_{h=0}^{N_{\mathrm{H}}-1}\tilde{\mathbf{J}}_{l,p}^{\mathrm{Rnl},h,h'}[n,n']e^{jh\omega_0 t_{l,0}}\right) \\
&\vdots \\
\mathbf{J}_{l,M,p}^{\mathrm{nl}}[n,n']\cos(h'\omega_0 t_{l,M}) &\approx \operatorname{Re}\left(\sum_{h=0}^{N_{\mathrm{H}}-1}\tilde{\mathbf{J}}_{l,p}^{\mathrm{Rnl},h,h'}[n,n']e^{jh\omega_0 t_{l,M}}\right) \\
\mathbf{J}_{l,0,p}^{\mathrm{nl}}[n,n']\sin(h'\omega_0 t_{l,0}) &\approx \operatorname{Re}\left(\sum_{h=0}^{N_{\mathrm{H}}-1}\tilde{\mathbf{J}}_{l,p}^{\mathrm{Inl},h,h'}[n,n']e^{jh\omega_0 t_{l,0}}\right) \\
&\vdots \\
\mathbf{J}_{l,M,p}^{\mathrm{nl}}[n,n']\sin(h'\omega_0 t_{l,M}) &\approx \operatorname{Re}\left(\sum_{h=0}^{N_{\mathrm{H}}-1}\tilde{\mathbf{J}}_{l,p}^{\mathrm{Inl},h,h'}[n,n']e^{jh\omega_0 t_{l,M}}\right)
\end{aligned} \tag{2.11}$$

Here, $\mathbf{J}_{l,m,p}^{\mathrm{nl}} = \partial\mathbf{I}^{\mathrm{nl}} / \partial\mathbf{V}\big|_{\mathbf{V}=\mathbf{V}_{l,m,p-1}}$ denotes the Jacobian obtained from the nonlinear equations in time domain. These equations can also be solved efficiently by using FFTs if M and $t_{l,m}$ are chosen as mentioned in stage 2.

Stage 5: Find the Newton step $\tilde{\mathbf{s}}_{l,p}$ and update the guess as $\tilde{\mathbf{V}}_{l,p}^{\mathrm{CKT}} = \tilde{\mathbf{V}}_{l,p-1}^{\mathrm{CKT}} - \tilde{\mathbf{s}}_{l,p}$. To find $\tilde{\mathbf{s}}_{l,p}$, which is a complex vector, its real and imaginary parts are stored in a real-

valued vector denoted as $\tilde{\tilde{\mathbf{s}}}_{l,p}$ and a set of $(2N_{\mathrm{H}}-1)N_{\mathrm{CKT}}$ real-valued equations are constructed and solved:

$$(\tilde{\tilde{\mathbf{Y}}}+\tilde{\tilde{\mathbf{J}}}^{\mathrm{nl}}_{l,p})\tilde{\tilde{\mathbf{s}}}_{l,p}=\tilde{\tilde{\mathbf{r}}}_{l,p-1} \tag{2.12}$$

Here, the vectors and matrices are formed by separating the real and imaginary parts of the corresponding vectors and matrices in (2.12) and (2.11). This system of equation is solved iteratively. In (2.12), $\tilde{\tilde{\mathbf{s}}}_{p}$ is a size $(2N_{\mathrm{H}}-1)N_{\mathrm{CKT}}$ vector that stores the real and imaginary parts of the Newton step $\tilde{\mathbf{s}}_{p}=\left[\tilde{\mathbf{s}}_{p}^{0\,T},\mathrm{Re}(\tilde{\mathbf{s}}_{p}^{\mathrm{CKT},1})^{T},\mathrm{Im}(\tilde{\mathbf{s}}_{p}^{1})^{T},\right.$ $\left.\cdots,\mathrm{Re}(\tilde{\mathbf{s}}_{p}^{N_{\mathrm{H}}-1})^{T},\mathrm{Im}(\tilde{\mathbf{s}}_{p}^{N_{\mathrm{H}}-1})^{T}\right]^{T}$. The real residual vector $\tilde{\tilde{\mathbf{r}}}_{l,p-1}$ is similarly expressed in terms of the complex one $\tilde{\mathbf{r}}_{l,p-1}$.The matrices $\tilde{\tilde{\mathbf{Y}}}$and $\tilde{\tilde{\mathbf{J}}}^{\mathrm{nl}}_{l,p}$ are of size $(2N_{\mathrm{H}}-1)N_{\mathrm{CKT}}\times(2N_{\mathrm{H}}-1)N_{\mathrm{CKT}}$ that have sub-blocks of size $N_{\mathrm{CKT}}\times N_{\mathrm{CKT}}$ sub-blocks; each sub-block represents coupling between two envelopes. Thus $\tilde{\tilde{\mathbf{Y}}}$is a block-diagonal matrix and $\tilde{\tilde{\mathbf{J}}}^{\mathrm{nl}}_{l,p}$ is dense and their block-matrices are expresses as:

$$\begin{aligned}
\tilde{\tilde{\mathbf{Y}}}^{0,0}&=\tilde{\mathbf{Y}}^{0,0}\\
\tilde{\tilde{\mathbf{Y}}}^{h,h}&=\begin{bmatrix}\mathrm{Re}(\tilde{\mathbf{Y}}^{h}) & -\mathrm{Im}(\tilde{\mathbf{Y}}^{h})\\ \mathrm{Im}(\tilde{\mathbf{Y}}^{h}) & \mathrm{Re}(\tilde{\mathbf{Y}}^{h})\end{bmatrix}\\
\tilde{\tilde{\mathbf{J}}}^{\mathrm{nl},0,0}&=\tilde{\mathbf{J}}^{\mathrm{Rnl},0,0}\\
\tilde{\tilde{\mathbf{J}}}^{\mathrm{nl},0,h'}&=\begin{bmatrix}\mathrm{Re}(\tilde{\mathbf{J}}^{\mathrm{Rnl},0,h'}) & -\mathrm{Re}(\tilde{\mathbf{J}}^{\mathrm{Inl},0,h'})\end{bmatrix}\\
\tilde{\tilde{\mathbf{J}}}^{\mathrm{nl},h,0}&=\begin{bmatrix}\mathrm{Re}(\tilde{\mathbf{J}}^{\mathrm{Rnl},h,0})\\ \mathrm{Im}(\tilde{\mathbf{J}}^{\mathrm{Rnl},h,0})\end{bmatrix}\\
\tilde{\tilde{\mathbf{J}}}^{\mathrm{nl},h,h'}&=\begin{bmatrix}\mathrm{Re}(\tilde{\mathbf{J}}^{\mathrm{Rnl},h,h'}) & -\mathrm{Re}(\tilde{\mathbf{J}}^{\mathrm{Inl},h,h'})\\ \mathrm{Im}(\tilde{\mathbf{J}}^{\mathrm{Rnl},h,h'}) & -\mathrm{Im}(\tilde{\mathbf{J}}^{\mathrm{Inl},h,h'})\end{bmatrix}
\end{aligned} \tag{2.13}$$

for $h,h'=1,\ldots,N_{\mathrm{H}}-1$.

2.3 NUMERICAL EXAMPLES

Four example circuits including, a series RLC circuit, a diode voltage multiplier circuit [62],a bipolar junction transistor (BJT) tuned amplifier and a metal-semiconductor field effect transistor (MESFET) amplifier are analyzed using the FE-CKT simulator. The results are compared with those obtained its time-domain counterpart [60]

2.3.1 Series RLC Circuit

In the first example, a series RLC circuit connected to a time-varying voltage source is analyzed; their component values are $R = 50\ \Omega$, $L = 0.1$ nH and $C = 1$ nF (Fig. 2.2(a)). The circuit is excited by a modulated Gaussian voltage source given by

$$VS(t) = e^{-(t-t_{\mathrm{d}})^2/2\sigma^2}\cos(\omega_0(t-t_{\mathrm{d}})) \tag{2.14}$$

Here, $\omega_0 / 2\pi = 500$ MHz, $\sigma = 30/\pi$ ns and $t_{\mathrm{d}} = 46.4$ ns. Less than 0.1% of the pulse power is $\omega_0 \pm \omega_0 / 10$. There are three non-reference nodes and one voltage source branch, i.e. $N_{\mathrm{CKT}} = 4$. As the circuit is linear, only the fundamental carrier is used and the time step size is chosen to be $\Delta t = \pi / \omega_0$ The current found from this simulation is compared to a time-domain simulation with time-step size $\pi / 20\omega_0$ [60] in Figs. 2.2(b)

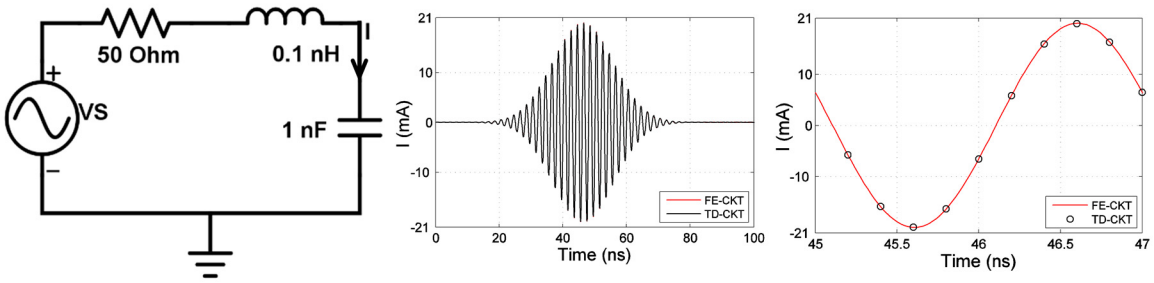

(a) (b) (c)

Fig. 2.2. Series RLC (a) CKT (b) Current in the circuit. (c) Current near the peak value.

and 2.2(c). The results agree well for the entire duration of the simulations.

.

2.3.2 Diode Voltage Multiplier

The DC voltage buildup in a three-stage differential voltage multiplier circuit used in energy-harvested RFID systems [62] is quantified (Fig. 2.3(a)). The diodes in the rectifier are modeled as an exponential current source, where $I_{\mathrm{S}} = 0.1\,\mu A$ and $V_{\mathrm{TH}} = 0.0346\,\mathrm{V}$, connected in parallel to a nonlinear capacitor, where $F_C = (1 - F(1+M) + MV_D^- \,/\, V_J)$, $C_{\mathrm{JO}} = 4.2902\,\mathrm{fF}$, TT=$39.386\,\mathrm{ps}$, $V_J = 0.21\,\mathrm{V}$, $F = 0.5$, and $M = 0.5$, and in series to a $R_{\mathrm{S}} = 0.2\ \Omega$ resistor (Fig. 2.3(b)). The series and parallel capacitors in Fig. 2.3(a) are 1 pF each $(C_{\mathrm{S}} = C_{\mathrm{P}} = 1\ \mathrm{pF})$, inductor L is $54.3\,\mathrm{nH}$, capacitor C is $0.55\,\mathrm{pF}$ and the DC current source I_{DC} is set to $1\ \mu\mathrm{A}$. The diode model parameters were obtained from a least square fit of the measured diode current and capacitance characteristics reported in [62] . The voltage multiplier is excited by a slowly ramping up sinusoidal voltage source connected to a 50 Ω series $(R_{\mathrm{S}} = 50\ \Omega)$ resistance [62] given as

$$V_{\mathrm{S}}(t) = 0.5 f(t \,/\, \tau_0)\sin(\omega_0 t)$$
$$f(t) = \begin{cases} 0 & \text{for } t \le 0 \\ 10t^3 - 15t^4 + 6t^5 & \text{for } 0 \le t < 1 \\ 1 & \text{for } 1 \le t \end{cases} \tag{2.15}$$

where $\tau_0 = 1000\pi \,/\, \omega_0$ and $\omega_0 \,/\, 2\pi = 915\ \mathrm{MHz}$. Less than $\sim 0.1\%$ of the pulse power is outside the frequency band of $\omega_0 \pm \omega_0 \,/\, 75$. There are 15 non-reference nodes and 1 voltage source i.e. $N_{\mathrm{CKT}} = 16$ and the number of harmonics was chosen to be 4 i.e. $N_{\mathrm{H}} = 4$. The time step size for FE-CKT are set to $15\pi \,/\, \omega_0 \approx 8\,\mathrm{ns}$. It is observed in Fig. 2.3(c) that the output voltage found from the FE-CKT simulation agrees well with

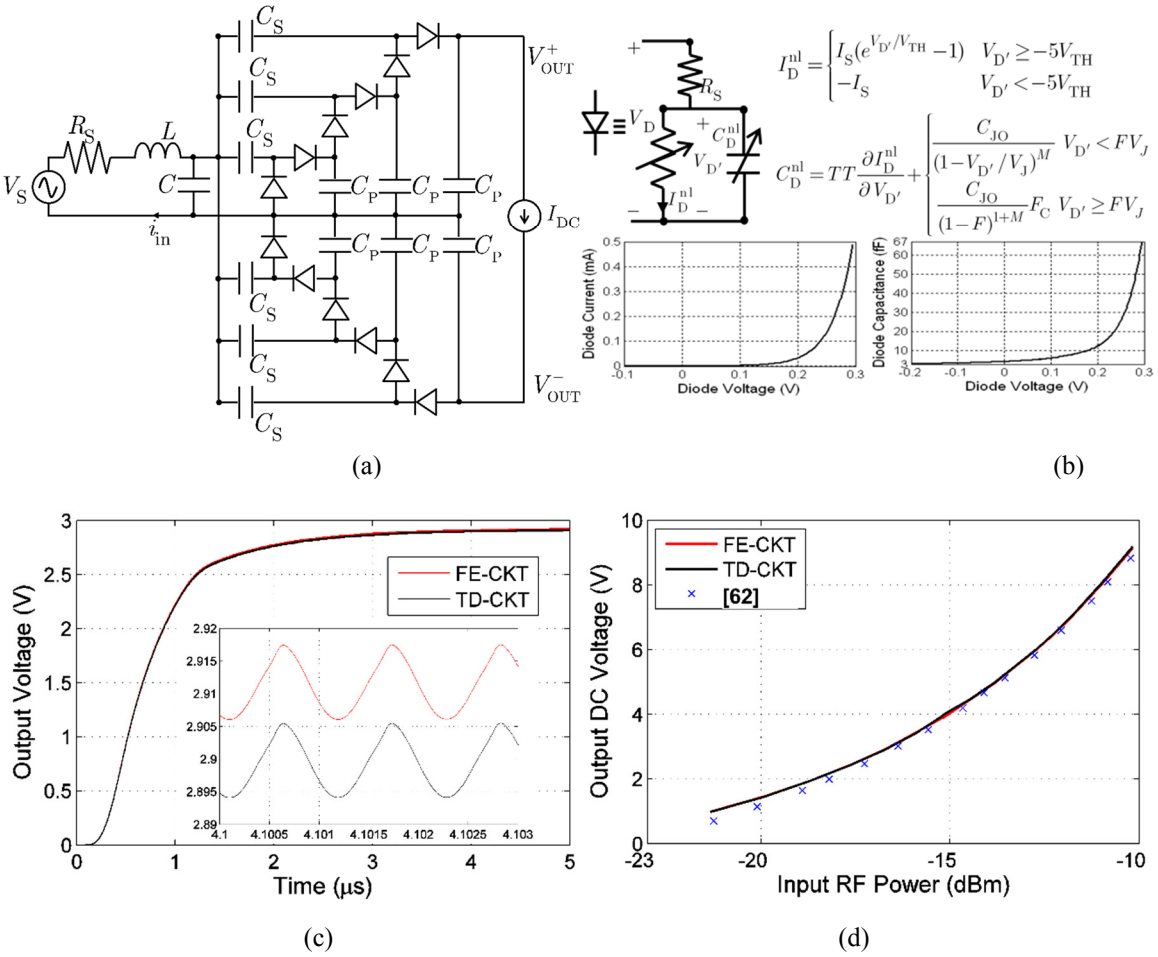

Fig. 2.3. Rectifier (a) Three-stage differential voltage multiplier. (b) Diode circuit model (derived from [62]). (c) Time-domain output voltage (inset: steady-state portion of voltage). (d) Output dc voltage versus the input power.

that found from the TD-CKT simulation with time step size $\pi / 20\omega_0 \approx 27$ ps for both the ramp-up duration and the steady state results. The difference between the TD-CKT and FE-CKT voltages are less than 1%.

Next, the simulations are repeated for different source voltage amplitudes (varied from 0.35 V to 1.1V) and the output DC voltage (average value of the steady state output voltage) is plotted in Fig. 2.3(d) as a function of the time-average power available at the source port given as

$$\bar{P}_{\text{in}} = \frac{\omega_0}{2\pi} \int_{t}^{t+2\pi/\omega_0} V_{\text{S}}(t') i_{\text{in}}(t') dt' \tag{2.16}$$

The results from the Fourier-envelope CKT and the TD-CKT simulation agree well with each other. The FE-CKT results also agree well with the results in [62]; the small discrepancies can be attributed to the differences in the diode model parameters.

2.3.3 BJT Tuned Amplifier

A tuned amplifier designed using BJT (Fig. 2.4(a)) is analyzed using the FE-CKT simulator The BJT is modeled using the large-signal Eber Moll's model [63] (Fig. 2.4(b)). The model parameters used are $I_{\text{S}} = 0.1 \text{ fA}$, $BF = 80$, $BR = 3$, $TF = TR = 0.5 \text{ ps}$, $C_{\text{JEO}} = 0.06 \text{ pF}$, $C_{\text{JCO}} = 0.18 \text{ pF}$, $V_{\text{JE}} = V_{\text{JC}} = 0.6 \text{ V}$ and $M_{\text{JE}} = M_{\text{JC}} = 0.33$. The tuning circuit parameters in Fig. 2.4(a) are $C_{\text{T}} = 1 \text{ nF}$, $R_{\text{T}} = 200 \ \Omega$ and $L_{\text{T}} = 1 \ \mu\text{H}$. The DC bias circuit parameters in Fig. 2.4(a) are $C_1 = 1 \text{ nF}$, $R_1 = 1 \text{ k}\Omega$ $R_2 = 100 \ \Omega$ and $V_{\text{CC}} = 10 \text{ V}$. The voltage input to the circuit is a slowly ramping up amplitude modulated sinusoid wave given as

$$V_{\text{S}}(t) = 0.2 f(t \ / \ \tau_0) \sin(\omega_{\text{mod}} t) \sin(\omega_0 t) \tag{2.17}$$

Here, $f(t)$ is the same as in (2.15), $\omega_0 \ / \ 2\pi = 1 \text{ MHz}$, $\omega_{\text{mod}} \ / \ 2\pi = 10 \text{ kHz}$ and $\tau_0 = 0.2 \text{ ms}$. There are 4 non-reference nodes and 2 voltage sources i.e. $N_{\text{CKT}} = 6$ There are four harmonics used i.e. $N_{\text{H}} = 4$. The DC operating point analysis is done *apriori* and the voltages at the non-reference nodes and the current through the inductor and voltage sources are initialized to the DC value. i.e., the 0$^{\text{th}}$ envelope of the currents and voltages are initialized to the DC value. The time step size for the FE simulation is chosen to be $\Delta t = 5\pi \ / \ \omega_0 \approx 5 \ \mu\text{s}$. The output voltage from the FE-CKT simulations are plotted in Figs. 2.4(c) and 2.4(d). The output voltages are compared with the results

from time-domain simulator with time step size $50\ \mathrm{ns}$. The results agree really well and the differences between them are less than 0.1% .

2.3.4 MESFET Amplifier

An amplifier circuit designed using MESFET (Fig. 2.5(a)) is analyzed using the Fourier envelope circuit simulator. The MESFET model along with its parasitic elements (Fig. 2.5(b)) is derived from [64]. Here, the parameters used are $C_{\mathrm{GSO}} = 3\ \mathrm{pF}$,

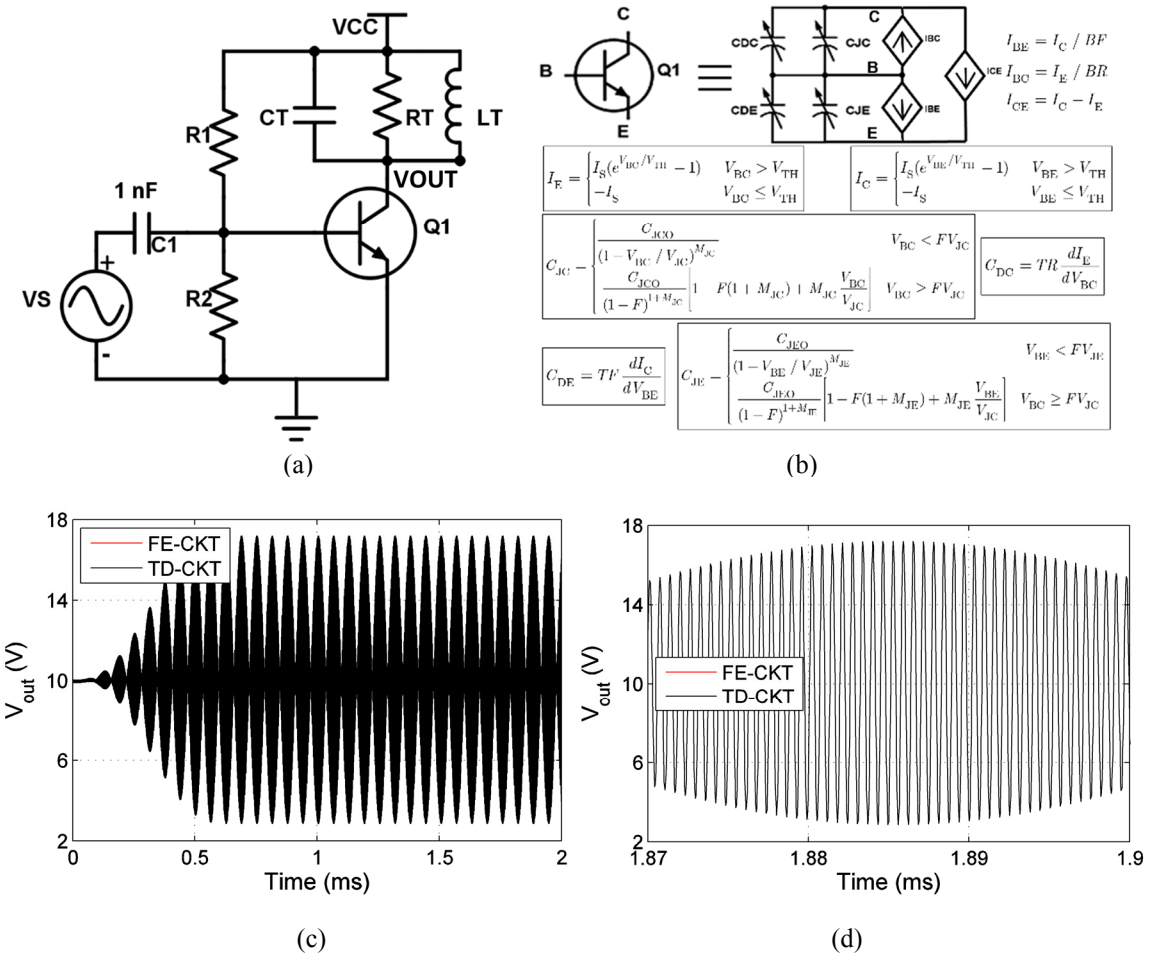

Fig. 2.4. Tuned Amplifier.(a) CKT (b) BJT circuit model – Eber Moll's static model. (c) Time-domain output voltage. (d) Steady state output voltage.

$V_{\mathrm{BI}} = 0.7\ \mathrm{V}$, $a_0 = 0.5304\ \mathrm{A}$, $a_0 = 0.2595\ \mathrm{A/V}$, $a_2 = -0.0542\ \mathrm{A/V^2}$, $a_3 = -0.0305\ \mathrm{A/V^3}$, and $GAMMA = 1.0\ \mathrm{V^{-1}}$.

The matching resistors in the circuit are 50 ohms i.e. $R_1 = R_2 = 50\ \Omega$ The dc bias voltages are set to $V_{\mathrm{GG}} = -0.81\ \mathrm{V}$ and $V_{\mathrm{DD}} = 18.96\ \mathrm{V}$ respectively. The input voltage is a modulated Gaussian pulse as given by (2.14). Here, $\omega_0 / 2\pi = 6\ \mathrm{GHz}$, $\sigma = 0.025 / \pi\ \mu\mathrm{s}$ and $t_0 = 39.577\ \mathrm{ns}$. There are 12 non-reference nodes and 3 voltage sources i.e. $N_{\mathrm{CKT}} = 15$ .and 4 harmonics were used The time step size of the simulation

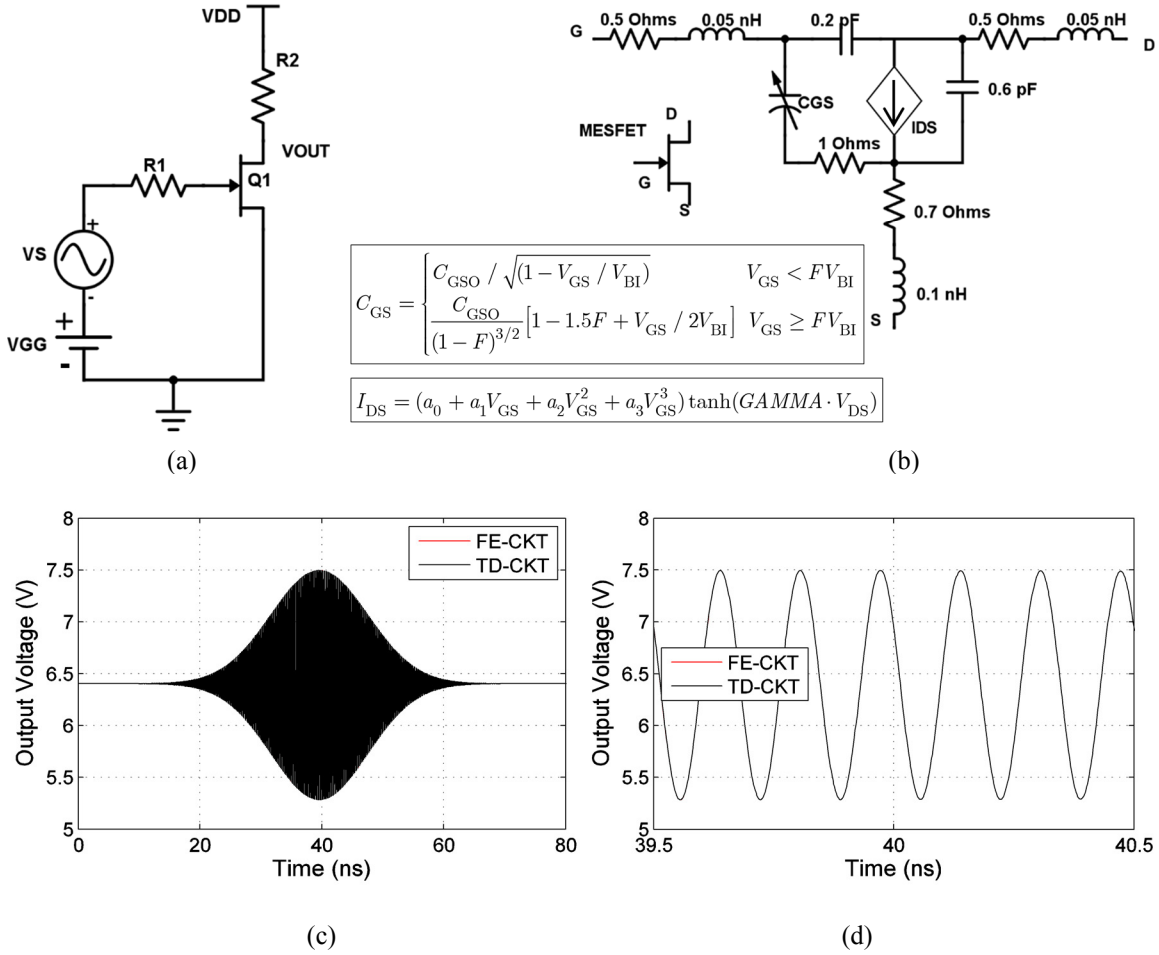

Fig. 2.5. MESFET Amplifier. (a) CKT. (b) MESFET circuit model. (c) Time-domain output voltage. (d) Steady state output voltage.

was set to be 50ps. The output voltage obtained from these simulations is plotted in Figs 2.5(c) and 2.5(d). As in the previous examples, The results are in excellent agreement with the result obtained from the time-domain simulations.

2.4 Combined Simulation of Multiple Circuits

Let circuits $D = 1,\ldots,N_{\mathrm{D}}$ consist of D_{n} nodes, D_{b} branches, D_{vs} voltage sources, and D_{is} current sources. As is typical, one of the nodes in each circuit is identified as the reference node for that circuit, (locally) numbered as the zeroth node, and assigned an zero voltage. Because each circuit is independent, the equations corresponding to the N_{D} different circuits are decoupled and each circuit can be analyzed separately. When the circuits are connected to EM module, however, the equations for the different circuits become coupled (through port currents and voltages); thus, the equations for all circuits must be solved simultaneously. For each circuit D, the voltages and currents are expressed in terms of N_{H} envelopes. Kirchhoff's current law and branch constitutive equations are enforced through MNA to relate the envelopes of voltages and currents. The number of unknowns for circuit D is denoted as N_{CKT}^{D}. For all circuits, the envelopes of voltages and currents are discretized using the same time step size. The ordinary differential equations are approximated in terms of the envelope samples using trapezoidal integration to obtain nonlinear system of equations

$$\begin{aligned} \tilde{\mathbf{Y}}^{1}\tilde{\mathbf{V}}_{l}^{\mathrm{CKT},1} + \tilde{\mathbf{I}}_{l}^{\mathrm{nl},1}(\tilde{\mathbf{V}}_{l}^{\mathrm{CKT},1}) &= \tilde{\mathbf{I}}_{l}^{\mathrm{CKT},1} \\ &\vdots \\ \tilde{\mathbf{Y}}^{N_{\mathrm{D}}}\tilde{\mathbf{V}}_{l}^{\mathrm{CKT},N_{\mathrm{D}}} + \tilde{\mathbf{I}}_{l}^{\mathrm{nl},N_{\mathrm{D}}}(\tilde{\mathbf{V}}_{l}^{\mathrm{CKT},N_{\mathrm{D}}}) &= \tilde{\mathbf{I}}_{l}^{\mathrm{CKT},N_{\mathrm{D}}} \end{aligned} \tag{2.18}$$

These equations can be expressed compactly by a system of equations (modifying (2.5)) as

$$\tilde{\mathbf{Y}}^{\mathrm{CKT}}\tilde{\mathbf{V}}_l^{\mathrm{CKT}} + \tilde{\mathbf{I}}_l^{\mathrm{nl}}(\tilde{\mathbf{V}}_l^{\mathrm{CKT}}) = \tilde{\mathbf{I}}_l^{\mathrm{CKT}} \tag{2.19}$$

where $N_{\mathrm{CKT}} = \sum_{D=1}^{N_{\mathrm{D}}} N_{\mathrm{CKT}}^{D}$, the vectors are the concatenations of all the N_{D} circuit vectors i.e. $\tilde{\mathbf{V}}_l^{\mathrm{CKT}} = \left[\tilde{\mathbf{V}}_l^{\mathrm{CKT},1^T}, \cdots, \tilde{\mathbf{V}}_l^{\mathrm{CKT},N_{\mathrm{D}}{}^T}\right]^T$, $\tilde{\mathbf{I}}_l^{\mathrm{nl}} = \left[\tilde{\mathbf{I}}_l^{\mathrm{nl},1^T}, \cdots, \tilde{\mathbf{I}}_l^{\mathrm{nl},N_{\mathrm{D}}{}^T}\right]^T$ and $\tilde{\mathbf{I}}_l^{\mathrm{CKT}} = \left[\tilde{\mathbf{I}}_l^{\mathrm{CKT},1^T}, \cdots, \tilde{\mathbf{I}}_l^{\mathrm{CKT},N_{\mathrm{D}}{}^T}\right]^T$. The matrix $\tilde{\mathbf{Y}}^{\mathrm{CKT}}$ is a block-diagonal matrix given by

$$\tilde{\mathbf{Y}}^{\mathrm{CKT}} = \begin{bmatrix} \tilde{\mathbf{Y}}^{1} & 0 & 0 \\ 0 & \ddots & 0 \\ 0 & 0 & \tilde{\mathbf{Y}}^{N_{\mathrm{D}}} \end{bmatrix} \tag{2.20}$$

The nonlinear solution scheme described in section 2.2 can be used to solve (2.19) instead of (2.5). However, if there is no EM module, these CKT equations can be solved independently. The coupling and the nonlinear solution algorithm for the hybrid EM-CKT simulation will be presented in the next chapter.

CHAPTER 3

FOURIER ENVELOPE EM-CKT SIMULATOR FOR NONLINEARLY LOADED WIRE ANTENNAS[1]

In this chapter, the envelope tracking hybrid EM-CKT simulator for nonlinearly loaded wire antennas is explained in detail. The formulation and the computational complexity of simulator are presented in Section 3.1. Numerical results validating the method and comparing the performance to time-domain method is presented in Section 3.2.

3.1 FORMULATION

Consider arbitrarily shaped wire antennas that are loaded with nonlinear time-invariant devices at various locations (Fig. 3.1). The antennas are assumed to reside in an unbounded homogeneous medium with permittivity ε and permeability μ, their wires are assumed to be PEC thin wires, whose cross sectional dimensions are much smaller than all wavelengths of interest, and the devices are assumed to be small enough to be accurately modeled as lumped circuits. The structure is excited by a combination of an electric field due to external impressed sources $\mathbf{E}^{\mathrm{inc}}(\mathbf{r},t)$ and voltage sources $VS_1(t)$, $VS_2(t),\ldots$ and current sources $IS_1(t), IS_2(t),\ldots$ within the lumped circuits. The incident electric field on the wires is assumed to be zero for $t \leq 0$ and essentially bandlimited to the angular frequency band $[\omega_0 - \omega_{\mathrm{bw}}, \omega_0 + \omega_{\mathrm{bw}}]$, where ω_0 is the fundamental carrier frequency and ω_{bw} is the single-sided bandwidth.

[1] This chapter is written based on the work published in the journal paper V. Subramanian and A. E. Yılmaz, "An envelope tracking hybrid field-circuit simulator for narrowband analysis of nonlinearly loaded wire antennas," *IEEE Trans. Microw. Theory Techn.*, vol. 62, no. 2, Feb 2014. All the research reported in the paper was performed by the author of this dissertation Vivek Subramanian. Prof. Ali Yılmaz's contribution to the paper was purely advisory.

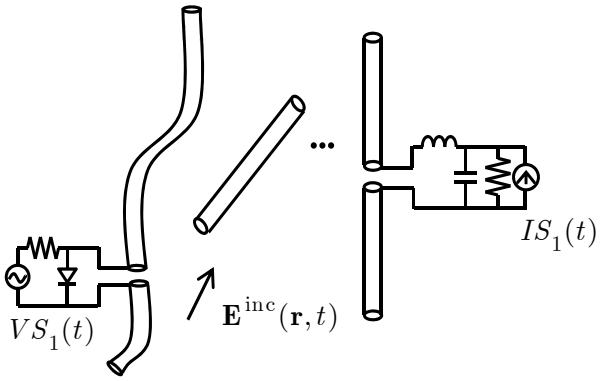

Fig. 3.1. Problem description. Wire antennas loaded with N_{D} devices.

All sources within the devices are assumed to be either DC sources or initially zero and essentially bandlimited just like the incident electric field.

3.1.1 EM Equations

To model the field interactions with the wires, the standard thin wire approximations [65] are made: (i) The azimuthal component of the current induced on the surface of the wires is assumed negligible compared to the axial component. (ii) The axial component of the current denoted as $\mathbf{I}_{\mathrm{s}}(\mathbf{r},t)$ is assumed to have no azimuthal variation. (iii) The currents at the caps of the wires are ignored. By discretizing the wires into piecewise cylindrical segments, enforcing the time derivatives of the axial component N_{W} of electric field on the axis of these segments to be zero, decomposing the electric field into incident and scattered components, and expressing the scattered field in terms of $\mathbf{I}_{\mathrm{s}}$, the reduced form of the thin-wire EFIE/Pocklington's equation [65], [66] is obtained, i.e.,

$$\hat{l}_u \bullet \partial_t \mathbf{E}^{\mathrm{inc}}(\mathbf{r},t) = \hat{l}_u \bullet [\nabla \partial_t \phi(\mathbf{r},t) + \partial_t^2 \mathbf{A}(\mathbf{r},t)] \tag{3.1}$$

for $u = 1,\ldots,N_{\mathrm{W}}$. Here, ∂_t denotes the partial time derivative operator, $\{\phi, \mathbf{A}\}$ denotes the {electric scalar, magnetic vector} potential, and $\hat{l}_u$ denotes the unit-vector along that axis. This equation is valid for all positions $\mathbf{r}$ on the axis of the u^{th} segment.

Next, the incident field and induced current are expanded using a truncated series with N_{H} harmonics:

$$\begin{aligned}\mathbf{E}^{\mathrm{inc}}(\mathbf{r},t) &\cong \mathrm{Re}\left(\sum_{h=0}^{N_{\mathrm{H}}-1} \tilde{\mathbf{E}}^{\mathrm{inc},h}(\mathbf{r},t)e^{jh\omega_0 t}\right)\\ \mathbf{I}_{\mathrm{s}}(\mathbf{r},t) &\cong \mathrm{Re}\left(\sum_{h=0}^{N_{\mathrm{H}}-1} \tilde{\mathbf{I}}_{\mathrm{s}}^{h}(\mathbf{r},t)e^{jh\omega_0 t}\right)\end{aligned} \tag{3.2}$$

Henceforth, $\tilde{\mathbf{E}}^{\mathrm{inc},h}$ and $\tilde{\mathbf{I}}_{\mathrm{s}}^{h}$ are referred as the h^{th} envelope of the incident electric field and induced current, respectively. By substituting (3.2) in (3.1), the EFIE is converted to N_{H} independent integral equations; each equation relates one of the envelopes of the current and the incident field. They are expressed as

$$\begin{aligned}\hat{l}_u \bullet (\partial_t + jh\omega_0)\tilde{\mathbf{E}}^{\mathrm{inc},h} = \hat{l}_u \bullet [&\nabla(\partial_t + jh\omega_0)\tilde{\phi}^h\\ &+ (\partial_t^2 + 2jh\omega_0\partial_t - h^2\omega_0^2)\tilde{\mathbf{A}}^h]\end{aligned} \tag{3.3}$$

for $h = 0,\ldots,N_{\mathrm{H}}-1$, $u = 1,\ldots,N_{\mathrm{W}}$, and $\mathbf{r}$ on the axis of the u^{th} segment. Here,

$$\begin{aligned}(\partial_t + jh\omega_0)\tilde{\phi}^h(\mathbf{r},t) &= -\iint_S \left[\nabla' \bullet \frac{\tilde{\mathbf{I}}_{\mathrm{s}}^h(\mathbf{r}', t - R/c)}{2\pi a(\mathbf{r}')}\right]\frac{e^{-jhk_0R}}{4\pi\varepsilon R}\,ds'\\ \tilde{\mathbf{A}}^h(\mathbf{r},t) &= \mu\iint_S \frac{\tilde{\mathbf{I}}_{\mathrm{s}}^h(\mathbf{r}', t - R/c)}{2\pi a(\mathbf{r}')}\frac{e^{-jhk_0R}}{4\pi R}\,ds'\end{aligned} \tag{3.4}$$

In (3.4), $R = |\,\mathbf{r} - \mathbf{r}'\,|$ is the distance between the source and the observer point, a is the wire radius, $c = (\mu\varepsilon)^{-1/2}$ is the speed of light in the background medium, and $k_0 = \omega_0 / c$ is the wave number at the fundamental carrier frequency.

In order to solve (3.3) numerically, the envelopes of the induced current are approximated as

$$\tilde{\mathbf{I}}_{\mathrm{s}}^{h}(\mathbf{r},t) \cong \sum_{l'=1}^{N_{\mathrm{T}}} \sum_{k'=1}^{N_{\mathrm{EM}}} \tilde{\mathbf{I}}_{l'}^{\mathrm{EM},h}[k']\mathbf{W}_{k'}(\mathbf{r})T_{l'}(t) \tag{3.5}$$

Here, $\tilde{\mathbf{I}}_{l'}^{\mathrm{EM},h}$ is an $N_{\mathrm{EM}} \times 1$ vector that stores unknown coefficients, $\mathbf{W}_{k'}$ are the spatial and $T_{l'}(t) = T(t - l'\Delta t)$ are the temporal basis functions, N_{EM} is the number of spatial and N_{T} is the number of temporal basis functions, and Δt is the time step size. In general, each envelope can be discretized using different spatial and temporal basis functions; here, identical basis functions are used to simplify the coupling with the CKT equations. Because the wires are assumed thin, the spatial basis functions are defined as triangle functions over two adjacent segments that are directed tangential to the axes of the wire segments [65], i.e., the vector basis have no azimuthal component and variation. The temporal basis functions are chosen as causal piecewise polynomial interpolatory functions [67]. Because the basis functions are interpolatory in space and time, the entries of the vector $\tilde{\mathbf{I}}_{l'}^{\mathrm{EM},h}$ are the samples of the h^{th} envelope of the induced current at N_{EM} different positions on the wires at time $l'\Delta t$.

Substituting (3.5) in (3.3) and Galerkin testing the resulting equations at times $\Delta t,\ldots,N_{\mathrm{T}}\Delta t$ yields:

$$\tilde{\mathbf{Z}}_0\tilde{\mathbf{I}}_{l}^{\mathrm{EM}} = \tilde{\mathbf{V}}_{l}^{\mathrm{EM}} - \sum_{l'=1}^{l-1} \tilde{\mathbf{Z}}_{l-l'}\tilde{\mathbf{I}}_{l'}^{\mathrm{EM}} \text{ for } l = 1,\ldots,N_{\mathrm{T}} \tag{3.6}$$

Here, $\tilde{\mathbf{I}}_{l'}^{\mathrm{EM}}$ is an $N_{\mathrm{H}}N_{\mathrm{EM}} \times 1$ vector that concatenates the unknown samples of the current envelopes at time $l'\Delta t$, i.e., $\tilde{\mathbf{I}}_{l'}^{\mathrm{EM}}[hN_{\mathrm{EM}}+1:(h+1)N_{\mathrm{EM}}] = \tilde{\mathbf{I}}_{l'}^{\mathrm{EM},h}[1:N_{\mathrm{EM}}]$ for $h = 0,\ldots,N_{\mathrm{H}}-1$. Similarly, $\tilde{\mathbf{V}}_{l}^{\mathrm{EM}}$ is the vector that contains all the incident electric field envelopes tested at time $l\Delta t$. The matrices $\tilde{\mathbf{Z}}_{l-l'}$, which are of size

$N_{\mathrm{H}}N_{\mathrm{EM}} \times N_{\mathrm{H}}N_{\mathrm{EM}}$, give the scattered field envelopes tested at time $l\Delta t$ due to the current envelope samples at time $l'\Delta t$. The entries of the matrices and vectors in (3.6) are given in Appendix II. Due to the linearity of the thin-wire EFIE, the equations corresponding to different harmonics in (3.6) are decoupled (each $\tilde{\mathbf{Z}}_{l-l'}$ matrix is block diagonal); thus, the samples of each current envelope can be found independently, one envelope at a time. When the wires are loaded by nonlinear devices, however, the equations for the different harmonics become coupled (through port currents and voltages); thus, the full system of equations (3.6) must be solved simultaneously at each time step; i.e., the samples of all current envelopes at each time step must be found together.

3.1.2 CKT Equations

Each of the N_{D} device is modeled as a lumped circuit. The circuit system of equations is obtained by (i) enforcing Kirchhoff's current laws and branch equations through MNA to relate the envelopes of the currents and the envelope voltages; and (ii) sampling the envelopes of the circuit quantities and discretizing the ordinary differential equations using trapezoidal rule. This procedure is detailed in Chapter 2. The resulting $N_{\mathrm{H}}N_{\mathrm{CKT}}$ system of equations at each time step is repeated here as

$$\tilde{\mathbf{Y}}^{\mathrm{CKT}}\tilde{\mathbf{V}}_l^{\mathrm{CKT}} + \mathbf{I}_l^{\mathrm{nl}}(\tilde{\mathbf{V}}_l^{\mathrm{CKT}}) = \tilde{\mathbf{I}}_l^{\mathrm{CKT}} \tag{3.7}$$

3.1.3 Coupling EM and CKT Equations

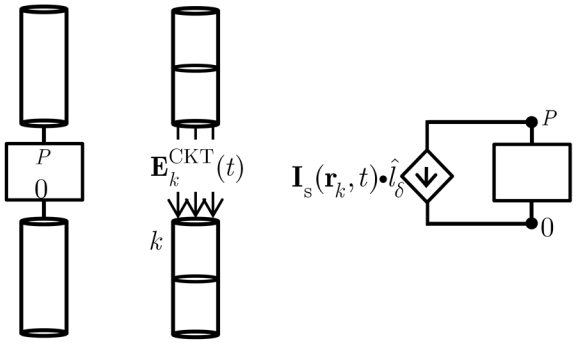

Fig. 3.2. EM-CKT coupling: (a) One-port circuit connected to the wires at node P and the reference node. (b) EM model. (c) CKT model.

The wires and the lumped circuits are coupled using the port model in [24], [25]. This model forces the voltage (line integral of electric field) and currents in the EM and CKT system of equations to be equal and makes the overall system of equations consistent. As an example, let the first circuit represent a two-terminal device occupying a small gap of length δ in the middle of the two segments corresponding to basis function k and be connected at nodes P and 0 as shown in Fig. 3.2. In this case, the coupling from the device to the wire is modeled by ignoring fringing fields, setting the electric field across the gap to be position independent, and equating its line integral to the port voltage, i.e., the envelopes of the time derivative of the electric field scattered by the wires are set as

$$\begin{aligned} &-\hat{l}_\delta\bullet(\partial_t + jh\omega_0)(\tilde{\mathbf{E}}^{\mathrm{sca},h}(\mathbf{r},t) + \tilde{\mathbf{E}}^{\mathrm{inc},h}(\mathbf{r},t)) \\ &= -\hat{l}_\delta\bullet(\partial_t + jh\omega_0)\tilde{\mathbf{E}}_k^{\mathrm{CKT},h}(t) = (\partial_t + jh\omega_0)\tilde{V}_P^{1,h}(t) \,/\, \delta \end{aligned} \tag{3.8}$$

for $\mathbf{r}$ in the gap and $h = 0,\ldots,N_{\mathrm{H}} - 1$. Here, $\hat{l}_\delta$ is the unit vector along the axis of the wire in the gap pointing from node 0 to node P. Here, the time derivative of the port voltage $\partial_t\tilde{V}_P^{1,h}$ is approximated by a third-order backward difference formula just as in [24], [25]. The coupling from the wires to the device is modeled by assuming that all the

axial component of the wire current at the port enters the circuit, i.e., by adding $\tilde{\mathbf{I}}_{\mathrm{s}}^{h}(\mathbf{r}_k,t)\cdot\hat{l}_\delta$ to the Kirchhoff's current law at node P for $\mathbf{r}_k$ in the middle of basis function $\mathbf{W}_k$ and $h=0,\ldots,N_{\mathrm{H}}-1$. If there are DC sources in the circuits, a two-step analysis is performed as in [25] and the coupling scheme is modified accordingly. In the first step, transient sources are turned off and DC analysis is performed (using the above coupling scheme) to find constant voltages and currents, which are used as initial conditions in the next step. In the second step, both DC and transient sources are turned on but the DC components of the currents and fields are removed from the EM system of equations. This is implemented by introducing independent DC voltage and current sources at the ports that remove the DC component of the port voltage when coupling from devices to wires and add the DC component of the port current when coupling from wires to devices [25].

The coupled system of equations can be expressed as

$$\tilde{\mathbf{F}}(\tilde{\mathbf{X}}_l)=\tilde{\mathbf{b}}_l \quad \text{for } l=1,\ldots,N_{\mathrm{T}} \tag{3.9}$$

where

$$\tilde{\mathbf{F}}(\tilde{\mathbf{X}}_l)=\begin{bmatrix}\tilde{\mathbf{Z}}_0^{\mathrm{EM}} & \tilde{\mathbf{C}}_0^{\mathrm{V}}\\ -\tilde{\mathbf{C}}^{\mathrm{I}} & \tilde{\mathbf{Y}}^{\mathrm{CKT}}\end{bmatrix}\underbrace{\begin{bmatrix}\tilde{\mathbf{I}}_l^{\mathrm{EM}}\\ \tilde{\mathbf{V}}_l^{\mathrm{CKT}}\end{bmatrix}}_{\tilde{\mathbf{x}}_l}+\begin{bmatrix}0\\ \tilde{\mathbf{I}}_l^{\mathrm{nl}}(\tilde{\mathbf{V}}_l^{\mathrm{CKT}})\end{bmatrix} \tag{3.10}$$

and

$$\tilde{\mathbf{b}}_l=\begin{bmatrix}\tilde{\mathbf{V}}_l^{\mathrm{EM}}-\sum_{l'=1}^{l-1}\tilde{\mathbf{Z}}_{l-l'}^{\mathrm{EM}}\tilde{\mathbf{I}}_{l'}^{\mathrm{EM}}-\sum_{l'=l-3}^{l-1}\tilde{\mathbf{C}}_{l-l'}^{\mathrm{V}}\tilde{\mathbf{V}}_{l'}^{\mathrm{CKT}}\\ \tilde{\mathbf{I}}_l^{\mathrm{CKT}}\end{bmatrix} \tag{3.11}$$

Here, $\tilde{\mathbf{V}}_l^{\mathrm{CKT}}$ is a vector formed by concatenating the vectors $\tilde{\mathbf{V}}_l^{\mathrm{CKT},1},\ldots,\tilde{\mathbf{V}}_l^{\mathrm{CKT},N_{\mathrm{D}}}$; i.e., it contains the samples at time $l\Delta t$ of the unknown voltage/current envelopes in all

circuits. Similarly, $\tilde{\mathbf{I}}_l^{\mathrm{CKT}}$ and $\tilde{\mathbf{I}}_l^{\mathrm{nl}}$ are formed by concatenating the vectors $\tilde{\mathbf{I}}_l^{\mathrm{CKT},1}\ldots,\tilde{\mathbf{I}}_l^{\mathrm{CKT},N_{\mathrm{D}}}$ and $\tilde{\mathbf{I}}_l^{\mathrm{nl},1},\ldots,\tilde{\mathbf{I}}_l^{\mathrm{nl},N_{\mathrm{D}}}$, respectively. All these vectors are of size $N_{\mathrm{H}}N_{\mathrm{CKT}}$, where $N_{\mathrm{CKT}}=N_{\mathrm{CKT}}^1+\ldots+N_{\mathrm{CKT}}^{N_{\mathrm{D}}}$ is the total number of CKT unknowns. The matrix $\tilde{\mathbf{Y}}^{\mathrm{CKT}}$ is a block-diagonal matrix; each of its blocks is one of the matrices $\tilde{\mathbf{Y}}^1,\ldots,\tilde{\mathbf{Y}}^{N_{\mathrm{D}}}$. The matrices $\tilde{\mathbf{C}}_{0,1,2,3}^{\mathrm{V}}$ represent coupling from devices to wires and $\tilde{\mathbf{C}}^{\mathrm{I}}$ represents the coupling from wires to the devices, respectively. Because the coupling at the ports is linear, these coupling matrices are block diagonal; their entries are given in Appendix III. Note that (3.9) contains $N_{\mathrm{H}}(N_{\mathrm{EM}}+N_{\mathrm{CKT}})$ equations.

3.1.4 Nonlinear Solution Algorithm

A multidimensional nonlinear solution algorithm is needed to solve (3.9) because of the $\tilde{\mathbf{I}}_l^{\mathrm{nl}}(\tilde{\mathbf{V}}_l^{\mathrm{CKT}})$ term that represents the equations governing the nonlinear CKT elements. At each time step, the Newton-Raphson algorithm is used to solve (3.9) for the vector $\tilde{\mathbf{X}}_l$. This procedure is similar to the one presented in Section 2.2 and is explained in detail here. Although the solution procedure for the proposed Fourier-envelope EM-CKT simulator is similar to that for the time-domain EM-CKT simulator in [25] , there are important modifications here because the unknown vector $\tilde{\mathbf{X}}_l$ and the equations $\tilde{\mathbf{F}}(\tilde{\mathbf{X}}_l)$ are complex valued and closed-form equations that relate the current and voltage envelopes are generally not available for nonlinear elements. The solution procedure can be $l\Delta t$ cast into five stages at each time step .

Stage 1: Compute the right hand side $\tilde{\mathbf{b}}_l$ of (3.9)

Stage 2: At each Newton iteration $p=1,2,\ldots$, compute the residual vector $\tilde{\mathbf{r}}_{l,p-1}=\tilde{\mathbf{F}}(\tilde{\mathbf{X}}_{l,p-1})-\tilde{\mathbf{b}}_l$ using $\tilde{\mathbf{X}}_{l,p-1}$, the solution vector guessed in the previous Newton iteration. The first guess is set to the solution at the previous time step: $\tilde{\mathbf{X}}_{l,0}=\tilde{\mathbf{X}}_{l-1}$. To compute the residual vector, the vectors

$\tilde{\mathbf{I}}_l^{\mathrm{nl},1}(\tilde{\mathbf{V}}_{l,p-1}^{\mathrm{CKT},1}),\ldots,\tilde{\mathbf{I}}_l^{\mathrm{nl},N_\mathrm{D}}(\tilde{\mathbf{V}}_{l,p-1}^{\mathrm{CKT},N_\mathrm{D}})$ must be evaluated, i.e., the N_H envelopes of the currents through nonlinear elements at time must be evaluated given the previous guess. When closed-form expressions are not available, these samples are approximated in three steps for each circuit $D = 1,\ldots,N_\mathrm{D}$; these are detailed for one circuit in Section 2.2. In effect, these approximations both sides of the envelope equation: for each circuit $D = 1,\ldots,N_\mathrm{D}$

$$\mathbf{I}^{\mathrm{nl},D}(\mathbf{V}^D,t) = \mathrm{Re}\left(\sum_{h=0}^{N_\mathrm{H}-1}\tilde{\mathbf{I}}^{\mathrm{nl},D,h}(\tilde{\mathbf{V}}^D,t)e^{jh\omega_0 t}\right) \tag{3.12}$$

and enforces the (incorrect) equations

$$\begin{aligned}\mathbf{I}^{\mathrm{nl},D}(\mathbf{V}_{l,0,p-1}^D,t_{l,0}) &\approx \mathrm{Re}\left(\sum_{h=0}^{N_H-1}\tilde{\mathbf{I}}_l^{\mathrm{nl},D,h}(\tilde{\mathbf{V}}_{l,p-1}^{\mathrm{CKT},D})e^{jh\omega_0 t_{l,0}}\right)\\ &\vdots\\ \mathbf{I}^{\mathrm{nl},D}(\mathbf{V}_{l,M,p-1}^D,t_{l,M}) &\approx \mathrm{Re}\left(\sum_{h=0}^{N_H-1}\tilde{\mathbf{I}}_l^{\mathrm{nl},D,h}(\tilde{\mathbf{V}}_{l,p-1}^{\mathrm{CKT},D})e^{jh\omega_0 t_{l,M}}\right)\end{aligned} \tag{3.13}$$

Stage 3: If $\left\|\tilde{\mathbf{r}}_{l,p-1}\right\| < tol \times \left\|\tilde{\mathbf{b}}_l\right\|$, where tol is a predefined tolerance, then set $\tilde{\mathbf{X}}_l = \tilde{\mathbf{X}}_{l,p-1}$ and stop the Newton iterations; else, calculate the next Newton step as follows.

Stage 4: Find the Jacobian. Because $\tilde{\mathbf{I}}^{\mathrm{nl}}$ depends on complex variables, the Jacobian must be computed with respect to the real and imaginary parts of these variables, i.e., for each circuit $D = 1,\ldots, N_\mathrm{D}$, $2N_\mathrm{H}^2$ matrices must be formed; the entries of these matrices are

$$\tilde{\mathbf{J}}_{l,p}^{\mathrm{Rnl},D,h,h'}[n,n'] = \left.\frac{\partial \tilde{\mathbf{I}}^{\mathrm{nl},D,h}[n]}{\partial \,\mathrm{Re}\{\tilde{\mathbf{V}}^{D,h'}[n']\}}\right|_{\tilde{\mathbf{V}}^{D,h'}[n']=\tilde{\mathbf{V}}_{l,p-1}^{\mathrm{CKT},D,h'}[n']}$$
$$\tilde{\mathbf{J}}_{l,p}^{\mathrm{Inl},D,h,h'}[n,n'] = \left.\frac{-\partial \tilde{\mathbf{I}}^{\mathrm{nl},D,h}[n]}{\partial \,\mathrm{Im}\{\tilde{\mathbf{V}}^{D,h'}[n']\}}\right|_{\tilde{\mathbf{V}}^{D,h'}[n']=\tilde{\mathbf{V}}_{l,p-1}^{\mathrm{CKT},D,h'}[n']} \tag{3.14}$$

for $n,n' = 1,\ldots,N_{\mathrm{CKT}}^{D}$. and $h,h' = 0,\ldots,N_{\mathrm{H}}-1$. Note that $\tilde{\mathbf{J}}_{l,p}^{\mathrm{Inl},D,h,0}$ is a null matrix because the envelope of the 0th harmonic is a real function. Similar to step 2, the entries of the Jacobian matrices are found approximately; i.e., the derivative of (3.13) rather than (3.12) is computed with respect to the real and imaginary parts of $\tilde{\mathbf{V}}_{l}^{\mathrm{CKT},D,h'}$:

$$\begin{aligned}
\mathbf{J}_{l,0,p}^{\mathrm{nl},D}[n,n']\cos(h'\omega_0 t_{l,0}) &\approx \mathrm{Re}\left(\sum_{h=0}^{N_{\mathrm{H}}-1}\tilde{\mathbf{J}}_{l,p}^{\mathrm{Rnl},D,h,h'}[n,n']e^{jh\omega_0 t_{l,0}}\right)\\
&\vdots\\
\mathbf{J}_{l,M,p}^{\mathrm{nl},D}[n,n']\cos(h'\omega_0 t_{l,M}) &\approx \mathrm{Re}\left(\sum_{h=0}^{N_{\mathrm{H}}-1}\tilde{\mathbf{J}}_{l,p}^{\mathrm{Rnl},D,h,h'}[n,n']e^{jh\omega_0 t_{l,M}}\right)\\
\mathbf{J}_{l,0,p}^{\mathrm{nl},D}[n,n']\sin(h'\omega_0 t_{l,0}) &\approx \mathrm{Re}\left(\sum_{h=0}^{N_{\mathrm{H}}-1}\tilde{\mathbf{J}}_{l,p}^{\mathrm{Inl},D,h,h'}[n,n']e^{jh\omega_0 t_{l,0}}\right)\\
&\vdots\\
\mathbf{J}_{l,M,p}^{\mathrm{nl},D}[n,n']\sin(h'\omega_0 t_{l,M}) &\approx \mathrm{Re}\left(\sum_{h=0}^{N_{\mathrm{H}}-1}\tilde{\mathbf{J}}_{l,p}^{\mathrm{Inl},D,h,h'}[n,n']e^{jh\omega_0 t_{l,M}}\right)
\end{aligned} \tag{3.15}$$

Here, $\mathbf{J}_{l,m,p}^{\mathrm{nl},D} = \partial\mathbf{I}^{\mathrm{nl},D} / \partial\mathbf{V}^{D}\big|_{\mathbf{V}^{D}=\mathbf{V}_{l,m,p-1}^{D}}$ denotes the Jacobian obtained from the nonlinear equations in time domain. These equations can also be solved efficiently by using FFTs if M and $t_{l,m}$ are chosen as mentioned in step 2.

Stage 5: Find the Newton step $\tilde{\mathbf{s}}_{l,p}$ and update the guess as $\tilde{\mathbf{X}}_{l,p} = \tilde{\mathbf{X}}_{l,p-1} - \tilde{\mathbf{s}}_{l,p}$. To find $\tilde{\mathbf{s}}_{l,p}$, which is a complex vector, its real and imaginary parts are stored in a real-valued vector denoted as $\tilde{\tilde{\mathbf{s}}}_{l,p}$ and a set of $(2N_{\mathrm{H}}-1)(N_{\mathrm{EM}}+N_{\mathrm{CKT}})$ real-valued equations are constructed and solved:

$$\begin{bmatrix} \tilde{\tilde{\mathbf{Z}}}_0^{\mathrm{EM}} & \tilde{\tilde{\mathbf{C}}}_0^{\mathrm{V}} \\ -\tilde{\tilde{\mathbf{C}}}^{\mathrm{I}} & \tilde{\tilde{\mathbf{Y}}}^{\mathrm{CKT}} + \tilde{\tilde{\mathbf{J}}}_{l,p}^{\mathrm{nl}} \end{bmatrix} \tilde{\tilde{\mathbf{s}}}_{l,p} = \tilde{\tilde{\mathbf{r}}}_{l,p-1} \tag{3.16}$$

The above vectors and matrices are formed by separating the real and imaginary parts of the corresponding vectors and matrices in (3.10) and (2.11); they are detailed in Appendix IV. This system of equation is solved iteratively.

The above Newton-Raphson solution scheme converges quadratically if the guessed vector $\tilde{\mathbf{X}}_{l,p}$ is close enough to the actual solution $\tilde{\mathbf{X}}_l$ and if the iterative solution of (3.16) converges [68]. The convergence of the iterative solver depends on many factors, including the discretization (Δt, N_{H}, space-time basis/testing functions used for the EM equations, integration rule used for the CKT equations), the antenna geometry, and the singularity of the Jacobian. The convergence rate can be improved by modifying these factors as well as by preconditioning (3.16) [55]–[57]. The preconditioning schemes are not used here and will be discussed in the next chapter.

3.1.5 Computational Complexity and Stability

Next, the computational costs of the Fourier envelope marching-on-in-time (FE-MOT) scheme are analyzed and compared to the time-domain MOT (TD-MOT) scheme described in [25]. In the following, the number of nonzero entries in the $\tilde{\mathbf{Z}}_0^{\mathrm{EM}}$ matrix, which can be sparse or dense depending on the bandwidth [35], is denoted by $N_{\mathrm{H}}N_0$. It is assumed that each circuit node is connected to only a few other nodes, i.e., the $\tilde{\mathbf{Y}}^{\mathrm{CKT}}$ matrix is assumed to be sparse with a total of $O(N_{\mathrm{H}}N_{\mathrm{CKT}})$ nonzero entries. It is also assumed that the nonlinear element equations depend on only a few of the MNA unknowns; i.e., if total number of nonlinear elements is denoted by $N_{\mathrm{CKT}}^{\mathrm{nl}}$, it is assumed that $\tilde{\mathbf{I}}_l^{\mathrm{nl}}$ depends on $O(N_{\mathrm{H}}N_{\mathrm{CKT}}^{\mathrm{nl}})$ unknowns; equivalently, $\tilde{\tilde{\mathbf{J}}}_{l,p}^{\mathrm{nl}}$ is assumed to have

$O(N_{\mathrm{H}}^2 N_{\mathrm{CKT}}^{\mathrm{nl}})$ nonzero entries. The average number of Newton iterations needed per time step is denoted by $\bar{N}_{\mathrm{N}}$.

In the first step of the FE-MOT scheme, the vector $\tilde{\mathbf{b}}_l$ is computed; this requires $O(N_{\mathrm{H}}(N_{\mathrm{EM}}^2 + N_{\mathrm{CKT}}))$ operations per time step. In the second step, the Newton iterations are started and the residual is computed. According to (3.10), finding the contribution from the linear and nonlinear parts of $\tilde{\mathbf{F}}$ to the residual requires $O(N_{\mathrm{H}}(N_0 + N_{\mathrm{CKT}}))$ and $O(N_{\mathrm{CKT}}^{\mathrm{nl}} N_{\mathrm{H}} \log N_{\mathrm{H}})$ operations, respectively; here it is assumed that FFTs are used to solve (3.13). Thus, a total of $O(\bar{N}_{\mathrm{N}} N_{\mathrm{H}}(N_0 + N_{\mathrm{CKT}} + N_{\mathrm{CKT}}^{\mathrm{nl}} \log N_{\mathrm{H}}))$ operations are required to compute the residual at each time step. In the fourth step, the Jacobian matrices are filled; this requires $O(\bar{N}_{\mathrm{N}} N_{\mathrm{CKT}}^{\mathrm{nl}} N_{\mathrm{H}} \log N_{\mathrm{H}})$ operations per time step if FFTs are used to solve (2.11). In the last step, the linear system of equations in (3.16) is solved iteratively; this requires $O(\bar{N}_{\mathrm{N}} \bar{N}_{\mathrm{I}} N_{\mathrm{H}}(N_0 + N_{\mathrm{CKT}} + N_{\mathrm{H}} N_{\mathrm{CKT}}^{\mathrm{nl}}))$ operations per time step; here, $\bar{N}_{\mathrm{I}}$ is the average number of iterations needed to solve (3.16) per Newton iteration per time step. Thus, the total cost of the five steps, which is referred henceforth as the "marching time", scales as $O(N_{\mathrm{T}}[N_{\mathrm{H}} N_{\mathrm{EM}}^2 + \bar{N}_{\mathrm{N}} \bar{N}_{\mathrm{I}} N_{\mathrm{H}} N_0 + \bar{N}_{\mathrm{N}} N_{\mathrm{H}}^2 N_{\mathrm{CKT}}^{\mathrm{nl}} + \bar{N}_{\mathrm{N}} \bar{N}_{\mathrm{I}} N_{\mathrm{H}} N_{\mathrm{CKT}}])$. For narrowband analysis, $N_0 \approx N_{\mathrm{EM}}^2$ [35] and typically $\bar{N}_{\mathrm{I}} \gg \log N_{\mathrm{H}}$; thus, the iterative solution in the fifth step dominates. Assuming $N_{\mathrm{CKT}}^{\mathrm{nl}} \approx N_{\mathrm{CKT}}$ (as is the case in all the examples in Section 3.2), the marching time scales as $O(N_{\mathrm{T}} \bar{N}_{\mathrm{N}} \bar{N}_{\mathrm{I}}[N_{\mathrm{H}} N_{\mathrm{EM}}^2 + N_{\mathrm{H}}^2 N_{\mathrm{CKT}}])$. The remaining major computational costs of the FE-MOT scheme are the time required to fill the matrices in (3.10)-(3.11) and the memory required to store them, both of which scale as $O(N_{\mathrm{H}}[N_{\mathrm{EM}}^2 + N_{\mathrm{CKT}}])$.

In the TD-MOT scheme, the marching time scales as $O(N_{\mathrm{T}}^{\mathrm{TD}}[N_{\mathrm{EM}}^2 + \bar{N}_{\mathrm{N}}^{\mathrm{TD}} \bar{N}_{\mathrm{I}}^{\mathrm{TD}}(N_0^{\mathrm{TD}} + N_{\mathrm{CKT}})])$ while the matrix fill time and memory

requirement scale as $O(N_{\mathrm{EM}}^2 + N_{\mathrm{CKT}})$ [25]; here, the variables with superscript TD are the counterparts in the time-domain scheme of the same variables without the superscript defined above for the Fourier envelope scheme. In general, the matrix setup time and memory requirement for FE-MOT is $\sim N_{\mathrm{H}}$ times larger. For moderate sized antennas, where the physical dimensions of the structure is comparable to or smaller than the wavelength at the maximum frequency of interest, $N_0^{\mathrm{TD}} \approx N_{\mathrm{EM}}^2$ and the FE-MOT marching time is $\sim N_{\mathrm{T}}^{\mathrm{TD}} \bar{N}_{\mathrm{N}}^{\mathrm{TD}} \bar{N}_{\mathrm{I}}^{\mathrm{TD}} \,/\, N_{\mathrm{T}} N_{\mathrm{H}} \bar{N}_{\mathrm{N}} \bar{N}_{\mathrm{I}}$ times smaller, where $N_{\mathrm{T}}^{\mathrm{TD}} \,/\, N_{\mathrm{T}} \sim \chi$ and $\chi = 1 + \omega_0 \,/\, \omega_{\mathrm{bw}}$. While it might appear that the narrower the bandwidth, the larger χ is and the relatively faster FE-MOT solution is; the comparison is complicated because the time step size and therefore $\bar{N}_{\mathrm{N}}$ and $\bar{N}_{\mathrm{I}}$ also depend on χ. For larger antennas, $N_0^{\mathrm{TD}} \sim N_{\mathrm{EM}}$, the right hand side vector computation dominates the TD-MOT cost, and the comparison becomes even less straightforward [25]. Also, it should be noted that the solutions from the methods might have different accuracy; in fact, envelope-tracking schemes are generally more accurate compared to their time-domain counterparts because of lower integration and interpolation errors [52], [67]**.** Thus, a more detailed analytical comparison of the FE-MOT and TD-MOT methods is not feasible; instead, the methods' computational costs and accuracy are compared empirically in Section 3.2.

As FE-MOT is an implicit time-marching method, it is generally slower but more stable than explicit time-marching methods. Nevertheless, errors due to approximate integration, interpolation, and iterative solution [67] during time marching can accumulate and lead to late-time instabilities, especially as N_{EM} increases. It is observed in that envelope-tracking integral-equation solution schemes are generally more stable than their time-domain counterparts for narrowband analysis and vice versa. No

instabilities were observed in the TD-MOT or FE-MOT solutions for the examples in Section 3.2.

3.2 NUMERICAL RESULTS

This section validates the proposed Fourier-envelope EM-CKT simulator and compares it to its time-domain counterpart by analyzing scattering from various nonlinearly loaded wire antennas and antenna arrays. Identical spatial basis functions are used when comparing FE-MOT and TD-MOT schemes. Unless noted otherwise, the temporal basis functions are third order causal piecewise polynomial functions (CPPIFs) for all envelope-tracking simulations and band-limited interpolatory functions (BLIFs) with half-width parameter 5 for time-domain simulations [59], [67]

3.2.1 Validation

Two examples are presented to validate the proposed method and to investigate its computational complexity. First, scattering from a dipole antenna center-loaded by a Gunn diode [26] is analyzed. The wire antenna is 1-m long with a length to diameter ratio of 74.2 (Fig. 3.3(a)). The Gunn diode is modeled as a $75\ \Omega$ resistor in parallel with a third order nonlinear resistor (Fig. 3.3(b)). The antenna is excited by a normally incident plane wave pulse that is a slowly ramping up sinusoid of unit amplitude [25], [69], , i.e.,

$$\mathbf{E}^{\mathrm{inc}}(\mathbf{r},t) = \hat{z} f((t-y/c)/\tau_0)\sin(\omega_0(t-y/c))$$
$$f(t) = \begin{cases} 0 & \text{for } t \le 0 \\ 10t^3 - 15t^4 + 6t^5 & \text{for } 0 \le t < 1 \\ 1 & \text{for } 1 \le t \end{cases} \tag{3.17}$$

where $\tau_0 = 1000\pi/\omega_0$. Less than 0.1% of the pulse power is outside the frequency band of $\omega_0 \pm \omega_0/75$ In the following simulations, the wire is discretized into 60 equal length segments and the circuit has only one non-reference node, i.e., $N_{\mathrm{EM}} = 59$ and

$N_{\mathrm{CKT}} = 1$. The current through the diode is found for $\omega_0 / 2\pi = 140\ \mathrm{MHz}$ using $N_{\mathrm{H}} = 4$ and $\Delta t = 15\pi / \omega_0 \approx 54\,\mathrm{ns}$; the result is compared to that found by the TD-MOT solver using BLIFs with a time step size $\pi / 20\omega_0 \approx 0.18\,\mathrm{ns}$ in Figs. 3.3(c)-3.3(d). The results agree well both during the ramp up and at steady state.

The performance of the FE-MOT and TD-MOT methods are compared by plotting the errors incurred by the methods as a function of their computational costs in Figs. 3.3(e)-3.3(f). In these plots, the error is defined as

$$error = \frac{\sqrt{\int_0^{N_{\mathrm{T}}\Delta t} \left(I(t) - I_{\mathrm{ref}}(t)\right)^2 dt}}{\sqrt{\int_0^{N_{\mathrm{T}}\Delta t} I_{\mathrm{ref}}^2(t) dt}} \tag{3.18}$$

Here, $N_{\mathrm{T}}\Delta t = 4.5\,\mu\mathrm{s}$, I is the current through the diode, and I_{ref} is computed from a more accurate FE-MOT simulation using $N_{\mathrm{H}} = 10$ and $\Delta t = 2\pi / \omega_0 \approx 6.6\ \mathrm{ns}$. The integrals in (3.18) are evaluated by using the trapezoidal rule with 30 samples per period of the fundamental carrier. The different data points in Fig. 3.3(e) are obtained by decreasing the time step size from $15\pi / \omega_0$ to $3\pi / \omega_0$ in the FE-MOT and from $\pi / 5\omega_0$ to $\pi / 25\omega_0$ in the TD-MOT schemes. The number of harmonics in the FE-MOT scheme is also varied. Fig. 3.3(e) clearly shows the trade-off between accuracy and computational cost. The following are observed in Fig. 3.3(e): (i) As the time step size decreases, both TD-MOT and FE-MOT, simulations become more accurate and costly. (ii) For TD-MOT, using BLIFs as temporal basis functions is the better choice because more accurate results are obtained with a marginal increase in cost compared to using CPPIFs. For FE-MOT, the error can be controlled also by changing the number of harmonics. (iii) Only reducing the time step size or increasing the number of harmonics is

not optimal, e.g., increasing the number of harmonics beyond 4 when Δt is too large (at 0.1% error level) or reducing the time step size beyond $8\pi / \omega_0$ when N_{H} is too small do not reduce the error further. Both parameters must be chosen carefully together for the best FE-MOT performance. (iv) The time step size and number of harmonics can be chosen such that FE-MOT method requires less simulation time compared to the TD-MOT method for errors in the $10^{-4}\% - 1\%$ range.

The error is plotted as a function of the memory requirement in Fig. 3.3(f). The different data points are obtained by varying the time step size; they correspond to the same simulations in Fig. 3.3(e). Fig. 3.3(f) shows that the FE-MOT memory requirement does not vary significantly with Δt but increases proportionally with N_{H}. The TD-MOT memory requirement is observed to be larger when BLIFs are used; this is due to increased span of the temporal basis functions [67]. Fig. 3.3(f) shows that TD-MOT scheme requires less memory than FE-MOT but is also less accurate.

The results are verified using an independent reference in Fig. 3.3(g). Here, $\omega_0 / 2\pi$ is varied from 50 to 450 MHz ($N_{\mathrm{H}} = 4$ and $\Delta t = 15\pi / \omega_0$ for all these results). After each simulation is completed, the steady-state portion of the current density is Fourier transformed to obtain the frequency-domain current density at the fundamental carrier frequency:

$$\mathbf{J}_{\mathrm{s}}(\mathbf{r}, \omega_0) = \int_{3.5\ \mu s}^{400\pi/\omega_0 + 3.5\ \mu s} \mathbf{J}_{\mathrm{s}}(\mathbf{r}, t) e^{-j\omega_0 t} dt \tag{3.19}$$

Then, this current density is used to find the backscattered radar cross section (RCS) of the antenna, which is plotted as ω_0 is varied in Fig. 3.3(g), where λ_0 denotes the free-space wavelength at ω_0. Fig. 3.3(g) shows that the Fourier-envelope EM-CKT

simulation results agree with the time-domain and reference harmonic-balance simulation results [26].

In the second example, scattering from a *p-n* junction diode loaded dipole antenna is analyzed (Fig. 3.4(a)). The dipole is the same as previous example, i.e., it is 1-m long with a length to diameter ratio of 74.2. The diode, which has a stronger nonlinearity compared to the previous example, is modeled as an exponential current source with $I_{\mathrm{S}} = 0.1\ \mathrm{pA}$ and $V_{\mathrm{TH}} = 0.02585215702\ \mathrm{V}$ connected in parallel to a capacitor with $C_{\mathrm{P}} = 1\ \mathrm{pF}$ and in series to a $R_{\mathrm{S}} = 16\ \Omega$ resistor (Fig. 3.4(b)). In this example, the antenna is excited by a normally incident Gaussian plane wave given by

$$\mathbf{E}^{\mathrm{inc}} = \hat{x} e^{-(t-t_{\mathrm{d}}-y/c)^2/2\sigma^2} \cos(\omega_0 (t - t_d - y/c)) \tag{3.20}$$

Here, $\omega_0/2\pi = 148.5\ \mathrm{MHz}$, $\sigma = 1/\pi\ \mu\mathrm{s}$, and $t_{\mathrm{d}} = 6\sigma$. Less than 0.01% of the incident pulse power is outside the frequency band of $\omega_0 \pm 3/\sigma$. In the following simulations, the dipole is divided into 60 equal segments, the circuit has two non-reference nodes, and five harmonics are used, i.e., $N_{\mathrm{EM}} = 59$, $N_{\mathrm{CKT}} = 2$, and $N_{\mathrm{H}} = 5$.

The voltage across the diode is found using $\Delta t = \pi\sigma/15 \approx 66\,\mathrm{ns}$ and is compared to that obtained from a TD-MOT simulation with time step size $\pi/20\omega_0$ $\approx 0.17\ \mathrm{ns}$ in Figs. 3.4(c)-3.4(d). Good agreement is observed between the TD-MOT and FE-MOT results both of which capture the negative DC voltage that remains across the diode after the excitation pulse extinguishes.

The methods' accuracy-cost trade-offs are compared in Figs. 3. 4(e)-3. 4(f); the different data points in the figures are obtained by decreasing the time step size from $15\pi/\omega_0$ to $3\pi/\omega_0$ in the FE-MOT and from $\pi/5\omega_0$ to $\pi/25\omega_0$ in the TD-MOT schemes.

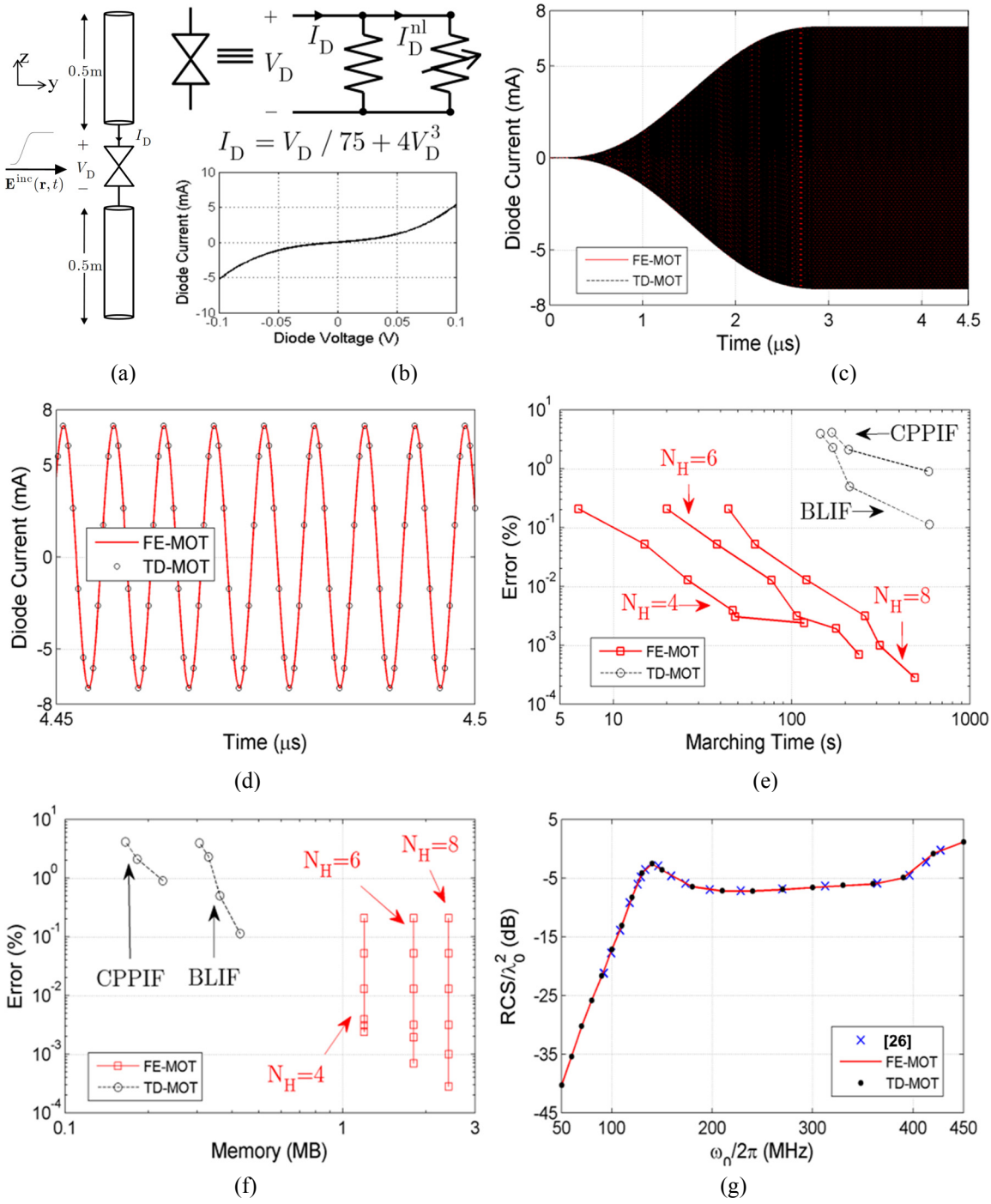

Fig. 3.3. Scattering from Gunn diode loaded dipole antenna (a) Dipole antenna loaded with a Gunn diode. (b) Gunn diode circuit model. (c) The current through the diode. (d) Steady state portion of the current through the diode. (e) Error versus marching time. (f) Error versus memory required. (g) Backscattered RCS.

In these plots, error is defined the same as (3.18), but $N_{\mathrm{T}}\Delta t = 4\,\mu\mathrm{s}$ and I_{ref} is computed from a more accurate FE-MOT simulation using $N_{\mathrm{H}} = 9$ and $\Delta t = \pi\sigma \,/\, 60$. To demonstrate the advantages of envelope tracking for narrow-band simulations, the above analysis is repeated as the bandwidth of the incident pulse is varied (σ is changed) and the results are shown in Fig. 3.4(e) for various values of $\chi = 1 + \omega_0 \,/\, \omega_{\mathrm{bw}} = 1 + \omega_0\sigma \,/\, 3$. As the excitations are made narrower band (increasing χ), the incident pulse width and the simulated time interval increase. In the TD-MOT case, this increase (without a considerable change in the time step size) requires the number of time steps to increase by a factor of $\sim \chi$, which increases the marching time as can be observed in Fig. 3.4(e). In the FE-MOT case, the increase in the simulated time interval is accompanied by an increase in the time step size; hence, as the bandwidth is reduced, the number of time steps and the marching time do not change significantly, which can also be observed in Fig. 3.4(e). The slight increase in the FE-MOT cost as the bandwidth becomes narrower is due to a small increase in $\bar{N}_{\mathrm{I}}$, the number of iterations in the iterative solution algorithm. Fig. 3.4(e) shows that, overall, the FE-MOT requires less marching time than TD-MOT for errors in the $10^{-3}\% - 1\%$ range and the FE-MOT method becomes more advantageous as the bandwidth becomes narrower. In Fig. 3.4(f), it is observed again that TD-MOT scheme requires less memory than FE-MOT scheme but is also less accurate. Fig. 3.4(f) shows that the memory requirement doesn't vary with bandwidth for either scheme.

To characterize the response of the antenna as a function of frequency, it is excited by a slowly ramping up sinusoidal pulse (3.17) and ω_0 is again varied from 50 to 450 MHz ($N_{\mathrm{H}} = 5$ and $\Delta t = 15\pi \,/\, \omega_0$ for all these results). The backscattered RCS is found from the steady state currents using (3.19) and plotted as a function of frequency in

Fig. 3.4(g). The RCS found by the FE-MOT and TD-MOT schemes agree well. Comparing Figs. 3.3(g) and 3.4(g), it is observed that the *p-n* junction diode causes the dipole antenna to resonate at a higher frequency compared to the Gunn diode, i.e., at $210\ \mathrm{MHz}$, where the antenna is $0.7\lambda_0$ long, and not at $140\ \mathrm{MHz}$, where it is $0.47\lambda_0$ long. This is due to the capacitive loading of the antenna by the *p-n* junction diode.

3.2.2 Complex Applications

Next, the FE-MOT method is used to solve two problems with more complicated loads and antennas. In the first problem, the DC voltage buildup in a rectenna is quantified. The rectenna comprises of a dipole antenna loaded by a voltage multiplier circuit, which converts the incident RF energy to DC voltage, e.g., for powering other circuit subsystems in RFID applications [62] (Fig. 3.5(a)). Here, the wire antenna is 16.4 cm long with a length to diameter ratio of 74.2, and a three-stage differential mode voltage multiplier is used as the rectifier [62] .The diode model parameters and the circuit component values for the voltage multiplier are the same as that presented in Section 2.3.2. The antenna is excited by the normally incident unit amplitude plane wave given by (3.17) with $\omega_0 / 2\pi = 915\ \mathrm{MHz}$. In the following simulations, the dipole is divided into 60 equal segments, the circuit has thirteen non-reference nodes, and four harmonics are used, i.e., $N_{\mathrm{EM}} = 59$, $N_{\mathrm{CKT}} = 16$, and $N_{\mathrm{H}} = 4$. The time step size for FE-MOT and TD-MOT are set to $15\pi / \omega_0 \approx 8\,\mathrm{ns}$ and $\pi / 20\omega_0 \approx 27\,\mathrm{ps}$, respectively. Fig. 3.5(c) shows that the output voltage found from the FE-MOT simulation agrees well with that found from the TD-MOT simulation both during the rise time and at steady state; the difference between them at steady state is less than 0.1%.

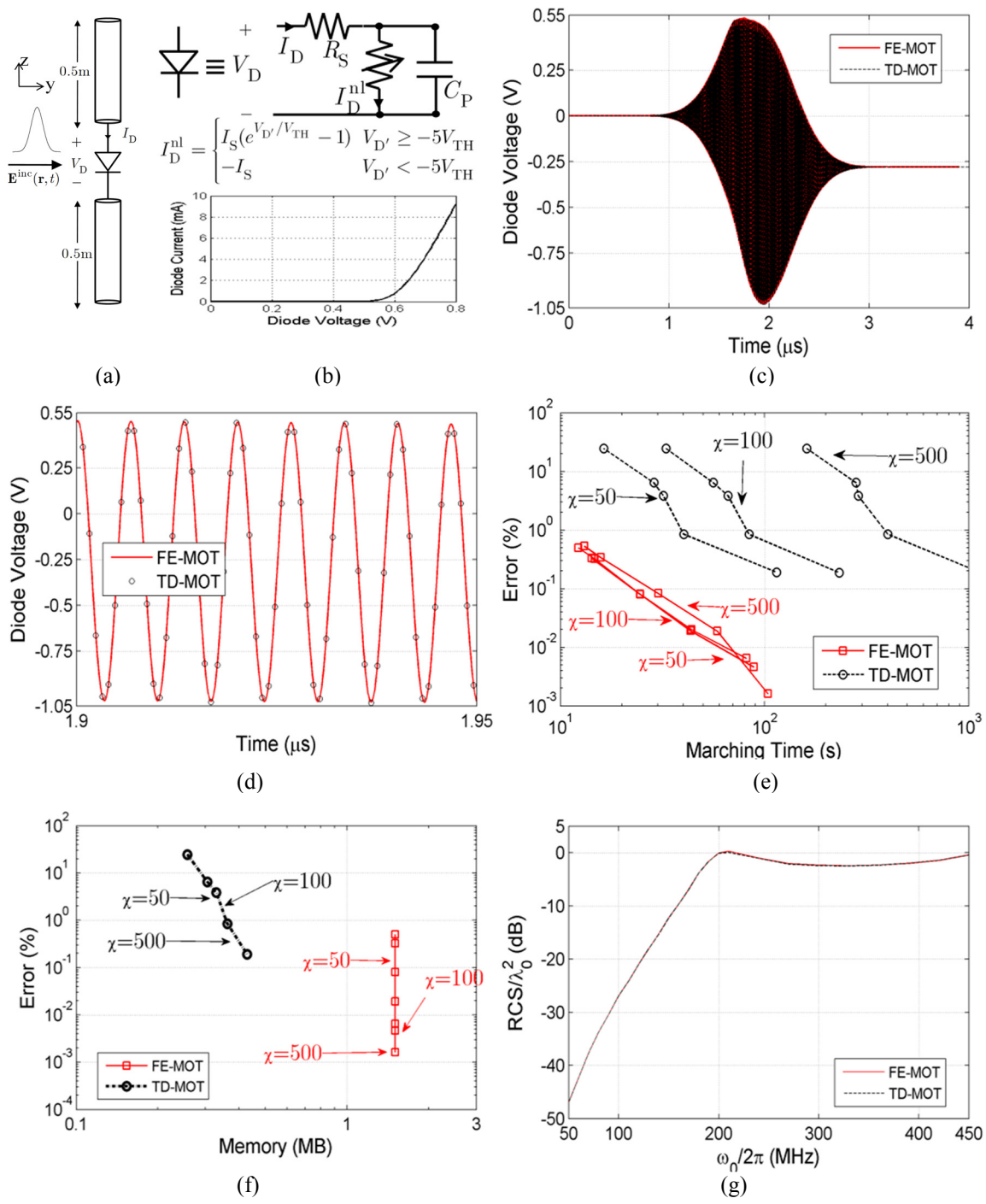

Fig. 3.4. Scattering from *p-n* junction diode loaded dipole antenna (a) Dipole antenna loaded with a *p-n* junction diode. (b) Diode circuit model. (c) The voltage across the diode. (d) Voltage near the peak value. (e) Error versus marching time as the excitation bandwidth changes. (f) Error versus memory required. (g) Backscattered RCS.

The errors and costs of the simulators are compared in Figs. 3.5(d)-3.5(e). In these plots, error is defined by (3.18) with $N_{\mathrm{T}}\Delta t = 5\,\mu\mathrm{s}$ and I_{ref} is computed from a more accurate FE-MOT simulation using $N_{\mathrm{H}} = 9$ and $\Delta t = 2\pi / \omega_0$. It is observed in Fig. 3.5(d) that FE-MOT parameters can be chosen such that it requires less simulation time than TD-MOT simulators for errors in the $10^{-3}\% - 1\%$ range. Similar to the examples in Section 3.2.1, it is observed in Fig. 3.5(e) that the FE-MOT memory requirement increases proportionally with N_{H} and is larger than the TD-MOT one.

The simulations are repeated for different excitation amplitudes (in the range 0.3 V/m to 2.1 V/m) and the output DC voltage (average value of the steady state output voltage) is plotted in Fig. 3.5(f) as a function of the time-average power available at the antenna ports, which is given as

$$\overline{P}_{\mathrm{in}} = \frac{\omega_0}{2\pi} \int_{t}^{t+2\pi/\omega_0} v_{\mathrm{in}}(t')\dot{i}_{\mathrm{in}}(t')dt' \tag{3.21}$$

The results from a Fourier-envelope CKT simulation that models the antenna as an independent voltage source connected to a 50 Ω series resistance [62] are also plotted in Fig. 3.5(f). In this pure CKT simulation, the voltage source is modeled as a slowly ramping up sinusoidal pulse just as in (3.17) with $\omega_0 / 2\pi$ equal to $915\ \mathrm{MHz}$ and its amplitude is varied from 0.35V to 1.1V. The results from the Fourier-envelope CKT simulation agree well with the results in [62]; the small discrepancies can be attributed to the differences in the diode model parameters. Fig. 3.5(f) shows that the output voltage found from the EM-CKT simulations is different than that from the pure CKT simulation; this is because of two reasons: (i) The input impedance of the dipole antenna is not 50 Ω. (ii) The CKT model neglects the higher frequency components of the currents on the wires and models the voltage at the ports as containing only the fundamental carrier and

not its harmonics. The higher frequency components of the wire current are also rectified in the EM-CKT simulation.

In the second problem, scattering from a phase conjugating frequency selective surface is analyzed [70]. The surface consists of an 10×10 array of dipole antennas each loaded by a Gunn diode (Fig. 3.6(a)). The problem is similar to the problem in Fig. 3.3; e.g., all the antennas are 1 m long with a length to diameter ratio of 74.2, the diodes are modeled as a linear resistor in parallel with a third order nonlinear resistor, and the antenna is excited by a normally incident plane wave pulse given by (3.17). There are two differences with the problem in Fig. 3.3: (i) There are more unknowns. Each dipole is divided into 60 segments, each circuit has one non-reference node, and three harmonics are used, i.e., $N_{\mathrm{EM}} = 5900$, $N_{\mathrm{CKT}} = 100$, and $N_{\mathrm{H}}=3$. (ii) Diodes are modeled as $I_{\mathrm{D}} = V_{\mathrm{D}} / 75 + a_3 V_{\mathrm{D}}^3$ [70].

The current through the first Gunn diode is plotted in Figs. 3.6(b)-3.6(c) when $a_3 = 0.5\ \mathrm{A/V}^3$ and $\omega_0 / 2\pi = 140\ \mathrm{MHz}$. Once again, good agreement is observed between the TD-MOT and FE-MOT results. To quantify the proposed method's performance with respect to the strength of the nonlinearity, the errors and costs of the methods are analyzed when a_3 is varied from 0 (the linear case) to 1 (strongly nonlinear case). Only the fundamental carrier is used for the linear case, just like for envelope-tracking pure EM simulators [52], and three harmonics ($N_{\mathrm{H}} = 3$) are used for the nonlinear cases. The time step size is varied from $15\pi / \omega_0$ to $3\pi / \omega_0$ and from $\pi / 10\omega_0$ to $\pi / 50\omega_0$ for the FE-MOT and TD-MOT schemes, respectively. The error in the current is computed using (3.18); here, $N_{\mathrm{T}}\Delta t = 4.5\ \mu\mathrm{s}$ and I_{ref} is the current found from a FE-MOT reference simulation where $\Delta t = 2\pi / \omega_0$ and either the fundamental harmonic is used (for the linear case) or $N_{\mathrm{H}}=6$.

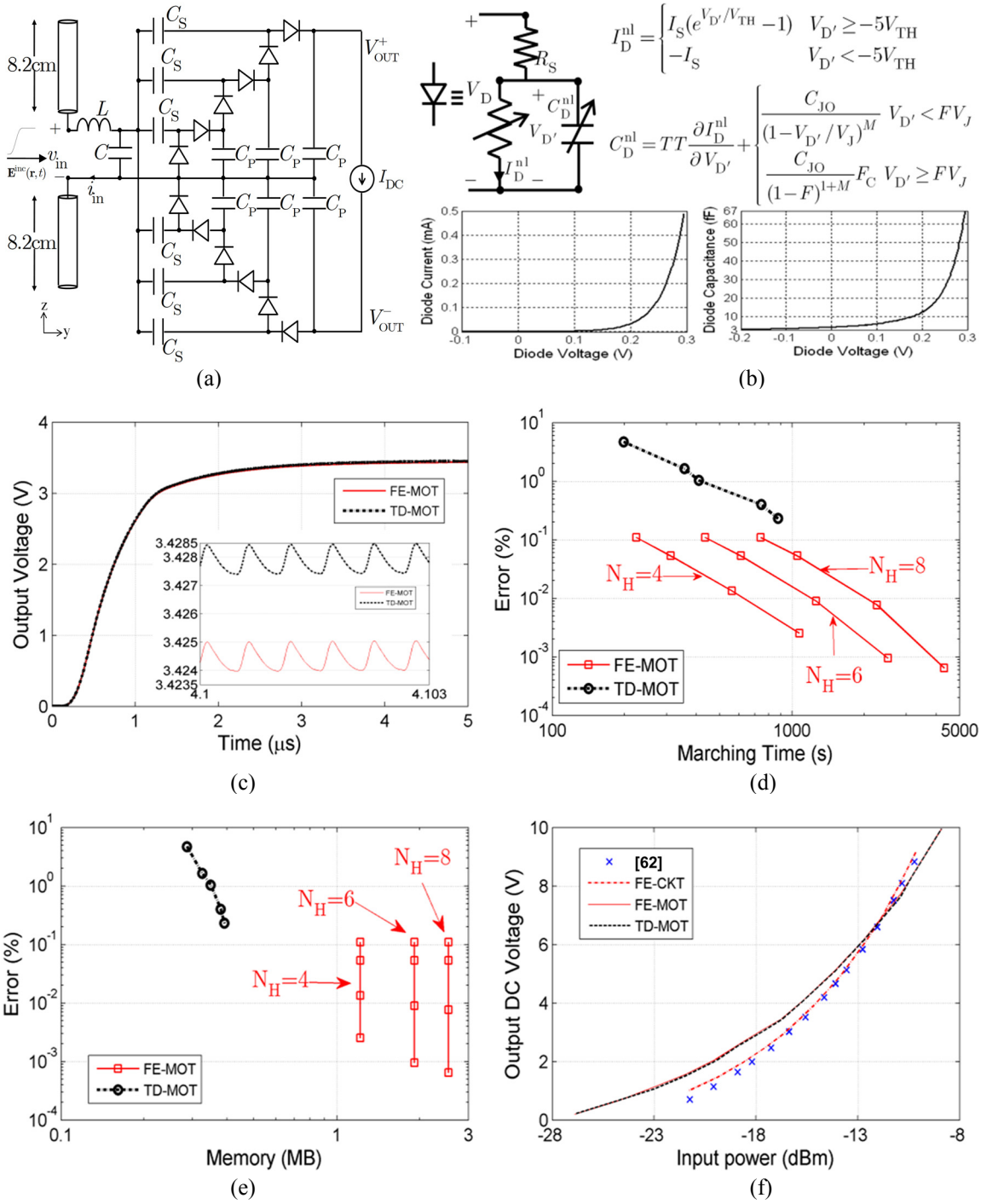

Fig. 3.5. Scattering from Rectenna. (a) Dipole antenna loaded with 3-stage voltage multiplier. (b) Diode circuit model (derived from [62]). (c) Time domain output voltage of rectenna (inset: steady state portion of voltage). (d) Error versus marching time. (e) Error versus memory required. (f) Output DC voltage versus the input power at antenna terminals.

Fig. 3.6(d) shows that overall FE-MOT requires less marching time than TD-MOT for error levels of $10^{-3}\% - 1\%$. Increasing the strength of the nonlinear resistor increases the marching costs only slightly for time-domain simulations but significantly for envelope-tracking ones: The stronger nonlinearities cause an increase in the number of Newton iterations ($\bar{N}_{\mathrm{N}}$ and $\bar{N}_{\mathrm{N}}^{\mathrm{TD}}$) in both envelope-tracking and time-domain simulations; additionally, it causes an increase in the number of iterations needed at each Newton iteration ($\bar{N}_{\mathrm{I}}$) in envelope-tracking simulations. For the TD-MOT scheme (especially with smaller time step sizes), the marching time is dominated by the right hand side computation and the increases in $\bar{N}_{\mathrm{N}}^{\mathrm{TD}}$ from $a_3 = 0.5$ to $a_3 = 1.0$ do not affect the costs significantly. For the FE-MOT scheme, however, the right hand side computation is negligible and the increases in $\bar{N}_{\mathrm{N}}$ and $\bar{N}_{\mathrm{I}}$ affect the cost significantly. Fig. 3.6(e) plots the error as a function of the memory required by the two schemes. It is observed that the FE-MOT scheme requires about the same memory as the TD-MOT scheme for the linear case and $\sim N_{\mathrm{H}}$ times more memory when loads are nonlinear; and the scheme's memory requirement is observed to not change significantly with the strength of the nonlinearity here (as N_{H} was not changed). The response of the array is quantified with respect to the strength of the nonlinearity by computing the backscattered RCS from the steady-state current density on the antenna array using (3.19); here, ω_0 is varied from $50\ \mathrm{MHz}$ to $250\ \mathrm{MHz}$. Fig. 3.6(f) shows that the RCS results found from envelope-tracking and time-domain simulations agree well. Here, the FE-MOT time step sizes are set to $15\pi\ /\ \omega_0$ and TD-MOT ones are set to $\pi\ /\ 20\omega_0$. The results show that the reflection from the array increases about 5dB from the linear case to the strongest nonlinear case near the resonant frequency, i.e., when $\omega_0 = 300\pi\,\mathrm{Mrad/s}$

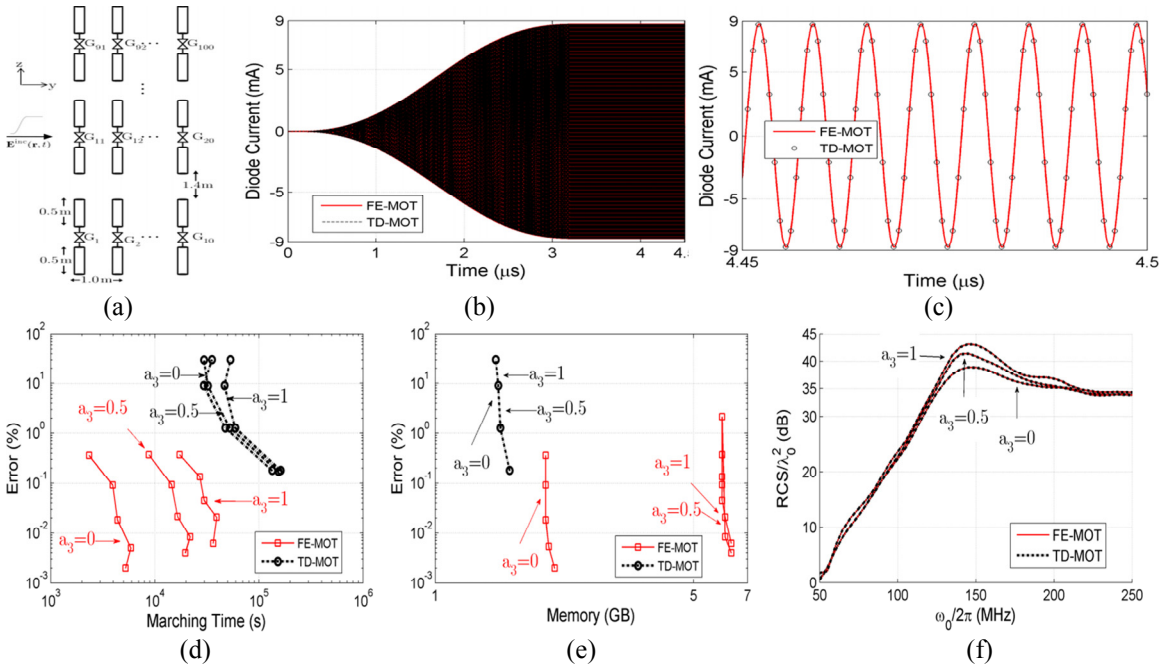

Fig. 3.6. Scattering from phase conjugating array. (a) Frequency selective surface. (b) Current through the Gunn diode G_1 at the bottom left. (c) Steady state portion of the current through G_1. (d) Error versus marching time as the strength of the nonlinearity increases from $a_3 = 0$ to $a_3 = 1$. (e) Error versus memory required. (f) Backscattered RCS.

CHAPTER 4

FOURIER ENVELOPE EM-CKT SIMULATORS UNDER BROAD(ER)-BAND EXCITATIONS[2]

The expressions to approximate the envelope of the current flowing through a nonlinear CKT element given the envelope voltage becomes invalid as the bandwidth of excitation broadens. Modifications are made in Stage 2 of the Newton Raphson algorithm (Section 2.2 and 3.1.4), which computes the residual vector $\tilde{\mathbf{r}}_{l,p-1} = \tilde{\mathbf{F}}(\tilde{\mathbf{X}}_{l,p-1}) - \tilde{\mathbf{b}}_l$ at each Newton iteration $p = 1,2,\ldots$ by using the solution $\tilde{\mathbf{X}}_{l,p-1}$ guessed at the end of the previous Newton iteration to facilitate broader band simulation with envelope tracking. The modifications are described in detail in Section 4.1. Numerical examples that demonstrate the advantages of these modifications in Section 4.2.

4.1 MODIFICATIONS TO THE NONLINEAR ALGORITHM

To compute $\tilde{\mathbf{r}}_{l,p-1}$ in stage 2 of the Newton Raphson algorithm described in Sections 2.2 and 3.1.4, the envelopes of the currents through nonlinear elements must be evaluated at time $l\Delta t$ given $\tilde{\mathbf{X}}_{l,p-1}$, i.e., $\tilde{\mathbf{I}}_l^{\mathrm{nl}}(\tilde{\mathbf{V}}_{l,p-1}^{\mathrm{CKT}})$ must be computed. When closed-form expressions are unavailable, these envelopes are estimated in three steps (Fig. 4.1):

First, the (unknown) voltages $\mathbf{V}^{\mathrm{CKT}}(t)$ are estimated at $M+1$ different time instants $t_{l,0},\ldots,t_{l,M}$ using the (known/ guessed) voltage envelope samples. This is achieved by interpolating the past voltage-envelope samples (previously computed) $\tilde{\mathbf{V}}_{l-N_{\mathrm{q}}}^{\mathrm{CKT}},\ldots,\tilde{\mathbf{V}}_{l-1}^{\mathrm{CKT}}$ and the present sample (guessed from the previous Newton iteration) $\tilde{\mathbf{V}}_{l,p-1}^{\mathrm{CKT}}$ to approximate the voltage envelopes at time instants $t_{l,0},\ldots,t_{l,M}$; i.e.,

[2] This chapter is written based on the work published in the journal paper V. Subramanian and A. E. Yılmaz, "An envelope tracking EM-CKT simulation of nonlinearly loaded wire antennas under broadband excitations," *Microw. Opt. Tech. Lett.*, vol. 57, no. 4, Feb 2015. All the research reported in the paper was performed by the author of this dissertation Vivek Subramanian. Prof. Ali Yılmaz's contribution to the paper was purely advisory.

$$\mathbf{v}^{\mathrm{CKT}}(t_{l,m}) = \mathrm{Re}\left\{\sum_{h=0}^{N_{\mathrm{H}}-1} \tilde{\mathbf{V}}^{\mathrm{CKT},h}(t_{l,m}) e^{j h \omega_0 t_{l,m}}\right\} \tag{4.1}$$

where $\tilde{\mathbf{V}}^{\mathrm{CKT},h}(t_{l,m})$ is approximated as

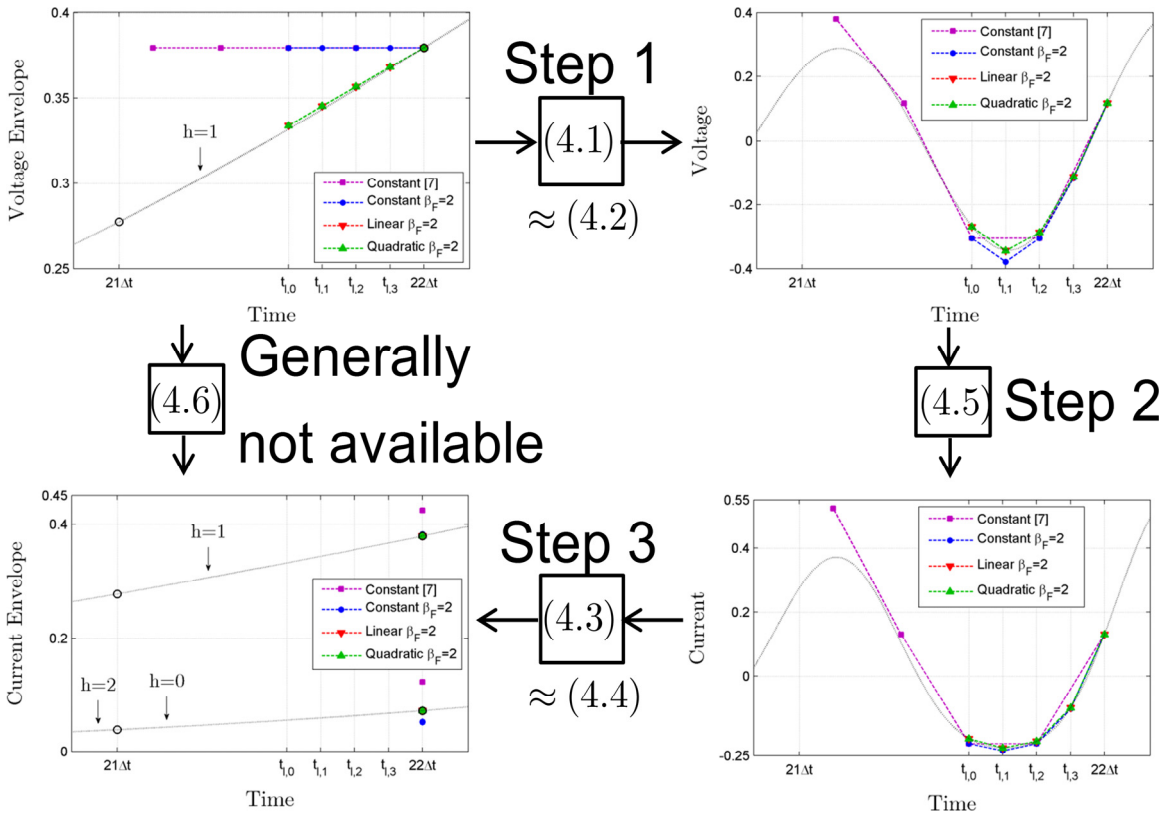

Fig. 4.1. Estimating current-envelope samples from voltage-envelope samples for a nonlinear element. A closed-form expression that relates current and voltage envelopes is used whenever possible (left); when such an expression is unknown/cannot be found, three steps are performed. Step 1: Approximate $M+1$ voltage samples from the voltage-envelope samples by using eq. (4.2) to approximate eq. (4.1). Step 2: Evaluate $M+1$ current samples using the time-domain relationship between the current and voltage in eq. (4.5). Step 3: Approximate current-envelope samples from the current samples by using eq. (4.4) to approximate eq. (4.3). Here, voltage envelope samples at time steps 21 and 22 are used to find the current envelope sample at time step 22, $N_{\mathrm{H}} = 3$, and $M = 4$.

$$\tilde{\mathbf{V}}^{\mathrm{CKT},h}(t_{l,m}) \approx \underbrace{\alpha_{0,m}\tilde{\mathbf{V}}^{\mathrm{CKT},h}_{l,p-1} + \sum_{l'=l-N_{\mathrm{q}}}^{l-1} \alpha_{l-l',m}\tilde{\mathbf{V}}^{\mathrm{CKT},h}_{l'}}_{\mathbf{V}^{\mathrm{CKT}}_{l,m,p-1}} \tag{4.2}$$

for $m = 0,\ldots,M$. Here, N_{q} is the interpolation order and $\alpha_{0,m},\ldots,\alpha_{N_{\mathrm{q}},m}$ are the interpolation coefficients. In the following, the voltage samples are estimated using (4.1) and (4.2) instead of (2.6) and are denoted as $\mathbf{V}^{\mathrm{CKT}}_{l,m,p-1}$.

Second, the time-domain currents through nonlinear elements, stored in the vector $\mathbf{I}^{\mathrm{nl}}(\mathbf{V}^{\mathrm{CKT}},t_{l,m})$, are estimated at the same time instants $t_{l,0},\ldots,t_{l,M}$ by using the (known) nonlinear circuit element models and the voltage samples found in the first step, i.e., the vector $\mathbf{I}^{\mathrm{nl}}(\mathbf{V}^{\mathrm{CKT}}_{l,m,p-1},t_{l,m})$, which approximates $\mathbf{I}^{\mathrm{nl}}(\mathbf{V}^{\mathrm{CKT}},t_{l,m})$, is computed.

Third, the current-envelope samples $\tilde{\mathbf{I}}^{\mathrm{nl}}_{l}(\tilde{\mathbf{V}}^{\mathrm{CKT}}_{l,p-1})$ are estimated using the current samples $\mathbf{I}^{\mathrm{nl}}(\mathbf{V}^{\mathrm{CKT}}_{l,m,p-1},t_{l,m})$ found in step 2. This is achieved by interpolating the past current envelope samples (computed at previous time steps) $\tilde{\mathbf{I}}^{\mathrm{nl}}(\tilde{\mathbf{V}}^{\mathrm{CKT}}_{1}),\ldots,\tilde{\mathbf{I}}^{\mathrm{nl}}(\tilde{\mathbf{V}}^{\mathrm{CKT}}_{l-1})$ and the present sample (unknown) $\tilde{\mathbf{I}}^{\mathrm{nl}}(\tilde{\mathbf{V}}^{\mathrm{CKT}}_{l,p-1})$ to approximate the current-envelope samples at time instants $t_{l,0},\ldots,t_{l,M}$ and solving the resulting system of equations to find $\tilde{\mathbf{I}}^{\mathrm{nl}}_{l}(\tilde{\mathbf{V}}^{\mathrm{CKT}}_{l,p-1})$, i.e., for $m = 0,\ldots,M$,

$$\mathbf{I}^{\mathrm{nl}}(\mathbf{V}^{\mathrm{CKT}},t_{l,m}) = \mathrm{Re}\left(\sum_{h=0}^{N_{\mathrm{H}}-1}\tilde{\mathbf{I}}^{\mathrm{nl},h}(\tilde{\mathbf{V}}^{\mathrm{CKT}},t_{l,m})e^{jh\omega_0 t_{l,m}}\right) \tag{4.3}$$

is enforced, the left-hand side is estimated as in the second step, and the $\tilde{\mathbf{I}}^{\mathrm{nl},h}(\tilde{\mathbf{V}}^{\mathrm{CKT}},t_{l,m})$ term on the right-hand side is expressed as

$$\tilde{\mathbf{I}}^{\mathrm{nl},h}(\tilde{\mathbf{V}}^{\mathrm{CKT}},t_{l,m}) \approx \alpha_0(t_{l,m})\tilde{\mathbf{I}}^{\mathrm{nl},h}_{l}(\tilde{\mathbf{V}}^{\mathrm{CKT}}_{l,p-1}) + \sum_{l'=l-N_{\mathrm{q}}}^{l-1}\alpha_{l-l'}(t_{l,m})\tilde{\mathbf{I}}^{\mathrm{nl},h}_{l'}(\tilde{\mathbf{V}}^{\mathrm{CKT}}_{l'}) \tag{4.4}$$

The current envelope samples are computed using (4.3) and (4.4) instead of (2.9). In (4.3), there are $M+1$ real-valued equations for the $N_{\mathrm{H}}-1$ complex-valued and one real-

valued (unknown) current-envelope samples $\tilde{\mathbf{I}}_l^{\mathrm{nl},0},\ldots,\tilde{\mathbf{I}}_l^{\mathrm{nl},\mathrm{N_H}-1}$. A square system of equations is obtained if M is chosen equal to $2N_{\mathrm{H}}-2$.

The validity and accuracy of this three-step estimation is dictated by the time instants $t_{l,0},\ldots,t_{l,M}$ as well as the interpolation scheme (N_{q} and α) used. Here, $M+1=2N_{\mathrm{H}}-1$ uniformly spaced time instants are chosen as $t_{l,m}=l\Delta t-2\pi(M-m)/s(M+1)\omega_0$ and piecewise constant, linear, or quadratic interpolation are used. Table I lists the interpolation coefficients for the time interval $[l\Delta t-\max(N_{\mathrm{q}},1)\Delta t, l\Delta t]$. The sampling parameter s controls how close the time instants used are to $l\Delta t$ ($s=1$ and piecewise constant interpolation results in (2.6) and (2.9)). The three-step procedure is illustrated in Fig. 4.1, where the envelope of the current through a typical second order nonlinear element

$$I(t)=-V(t)+V^2(t) \tag{4.5}$$

is computed for a known voltage envelope. In this special case, the envelopes of the current through this element can be related to the envelopes of the voltage across it in closed form:

$$\begin{aligned}
\tilde{I}^0(t)&=-\tilde{V}^0(t)+\tilde{V}^0(t)\tilde{V}^0(t)+\frac{1}{2}\sum_{h'=1}^{N_{\mathrm{H}}-1}\tilde{V}^{h'}(t)\tilde{V}^{h'*}(t)\\
\tilde{I}^h(t)&=-\tilde{V}^h(t)+2\tilde{V}^h(t)\tilde{V}^0(t)+\frac{1}{2}\sum_{h'=1}^{h-1}\tilde{V}^{h'}(t)\tilde{V}^{h-h'}(t)\\
&\quad+\sum_{h'=h+1}^{N_{\mathrm{H}}-1}\tilde{V}^{h'}(t)\tilde{V}^{h'-h^*}(t)\qquad \text{for } h=1,\ldots,N_{\mathrm{H}}-1
\end{aligned} \tag{4.6}$$

Here, the superscript $*$ represents the complex conjugate operator. In Fig. 4.1, the voltage is set to be a cosine modulated Gaussian pulse and $N_{\mathrm{H}}=3$, i.e., $\tilde{V}^1(t)=e^{-(t-6\sigma)^2/2\sigma^2}$ and $\tilde{V}^2(t)=\tilde{V}^0(t)=0$, where and $\omega_0/2\pi=150\,\mathrm{MHz}$; thus the corresponding current envelopes are $\tilde{I}^1(t)=-e^{-(t-6\sigma)^2/2\sigma^2}$ and

$\tilde{I}^0(t) = \tilde{I}^2(t) = 0.5e^{-(t-6\sigma)^2/\sigma^2}$. The time-step size for the three-step estimation is set to $\Delta t = \pi\sigma / 15$. In Fig. 4.1, the voltage envelope samples at time steps 20-22 and the current envelope samples at time steps 20 and 21 are used to estimate the current envelope samples at time step 22. The estimates are least accurate when piecewise constant interpolation with $s = 1$ (the scheme presented in Section 3.1.4) is used; the estimates are most accurate when piecewise linear or quadratic interpolation with $s = 2$ are used.

Table 4.1: Interpolation Schemes and Their Coefficients

Scheme	Interpolation Coefficients
Piecewise constant ($N_{\mathrm{q}} = 0$)	$\alpha_0(t) = 1$
Piecewise linear ($N_{\mathrm{q}} = 1$)	$\alpha_0(t) = \frac{t}{\Delta t} - (l-1) \quad \alpha_1(t) = l - \frac{t}{\Delta t}$
Piecewise quadratic ($N_{\mathrm{q}} = 2$)	$\alpha_0(t) = \frac{1}{2}(\frac{t}{\Delta t})^2 - (l - \frac{3}{2})\frac{t}{\Delta t} + \frac{(l-2)(l-1)}{2}$ $\alpha_1(t) = -(\frac{t}{\Delta t})^2 + 2(l-1)\frac{t}{\Delta t} - l(l-2)$ $\alpha_2(t) = \frac{1}{2}(\frac{t}{\Delta t})^2 - (l - \frac{1}{2})\frac{t}{\Delta t} + \frac{l(l-1)}{2}$

In the three-step estimation procedure, (4.3) and (4.4) are valid interpolation operations only if all of the $M+1$ time instants $t_{l,0},\ldots,t_{l,M}$ are in the interval $[(l - \max[N_{\mathrm{q}},1])\Delta t, l\Delta t]$. For $t_{l,0}$ to be in this interval, the time-step size must satisfy the condition $\Delta t \geq 2\pi(2N_{\mathrm{H}} - 2) / s\omega_0 \max(N_{\mathrm{q}},1)(2N_{\mathrm{H}} - 1)$; as the number of envelopes increases, $(2N_{\mathrm{H}} - 2) / (2N_{\mathrm{H}} - 1) \rightarrow 1$ and the condition becomes slightly more stringent. The time-step size is also limited from above by the Nyquist sampling criterion; combining these two conditions yields

$$\frac{\pi}{\omega_{\mathrm{bw}}} > \Delta t \geq \frac{2\pi}{s\omega_0 \max(N_{\mathrm{q}},1)} \tag{4.7}$$

The inequality implies that the three-step estimation procedure limits not only the smallest time-step size that can be used but also the maximum bandwidth that can be simulated by envelope tracking. It is clear from (4.7) that using a larger sampling parameter or a higher-order interpolation scheme relaxes the constraint on the bandwidth and enables broader band simulations. It should be emphasized that not all values in the range given in (4.7) are viable choices for the time-step size; indeed, Δt is also constrained by stability, accuracy, and efficiency requirements of the EM-CKT simulation [67] and the sampling rate can be neither much larger than the Nyquist rate nor too close to it (typically, $\pi / 2\omega_{\mathrm{bw}} \geq \Delta t \geq \pi / 10\omega_{\mathrm{bw}}$) [52]. The smaller is Δt relative to $\pi / \omega_{\mathrm{bw}}$, the smaller is the bandwidth that can be simulated (Fig. 4.2). Fig. 4.2 confirms that estimation schemes with large s or N_{q} are valid for broader band simulations. Fig. 4.2 also shows that for a fixed N_{q} and s, a larger time-step size would enable broader band envelope-tracking simulations. Of course, larger time step sizes generally yield less accurate results.

The computational cost of the proposed scheme differs from that in described in Section 3.1.4 primarily in the solution of (4.3). Solving (4.3) requires $O(N_{\mathrm{H}}^2 N_{\mathrm{CKT}})$ operations per Newton iteration as compared to $O(N_{\mathrm{H}} N_{\mathrm{CKT}} \log N_{\mathrm{H}})$ in section 3.1.2 and in [45]–[51] where FFTs are used to accelerate these operations. While this could cause a significant increase in computation time for envelope-tracking CKT analysis when there are strongly nonlinear elements (very large N_{H}), it is not expected to effect the computation time for most pure CKT simulations. In contrast, the increase in computation time is expected to be negligible for hybrid EM-CKT analysis because the computational costs are dominated by the EM system of equations in general.

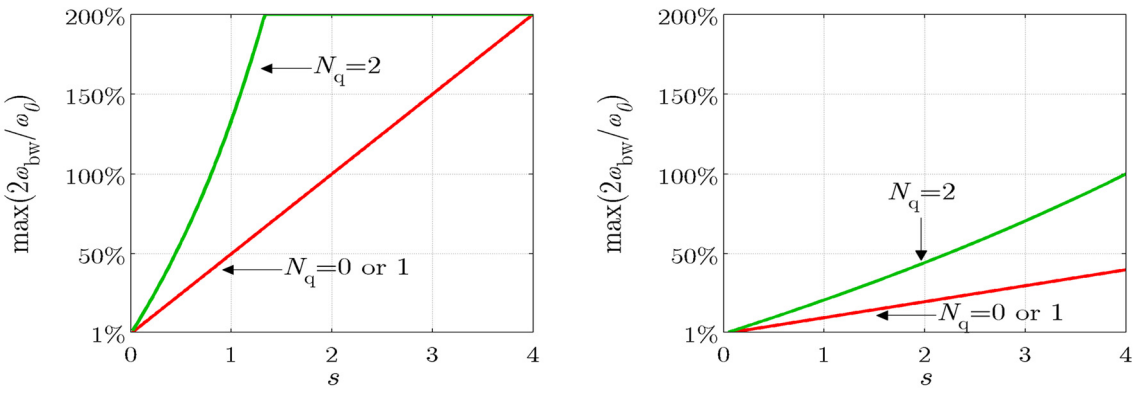

Fig. 4.2. Maximum bandwidth for which the three-step procedure in Fig. 4.1 is valid: (a) large time step ($\Delta t = \pi / 2\omega_{\mathrm{bw}}$). (b) Small time step ($\Delta t = \pi / 10\omega_{\mathrm{bw}}$).

Lastly, it should be noted that in stage 4 of the Newton-Raphson algorithm, Jacobian sub-matrices corresponding to nonlinear branches must be computed and the entries of these sub-matrices depend on the time instants used in the three-step procedure. These sub-matrices are independent of the interpolation scheme and can be found just as in stage 4 in Section 3.1.4 ((3.14) and (3.15)).

4.2 NUMERICAL RESULTS

The schemes proposed are validated and compared with the scheme in Section 3.1.4 by analyzing scattering from nonlinearly loaded antennas. In all the following simulations, band-limited interpolatory functions (with half-width parameter 5) [59], [67] were used as temporal basis functions. These temporal basis functions are non-causal and an extrapolation scheme is used to setup the EM part of the equations [59], [67].

First, scattering from a dipole antenna loaded with a p-n junction diode is analyzed. The dipole antenna is 1-m long with a length to diameter ratio of 74.2 and

center-loaded by the diode (Fig. 4.3(a)). The diode circuit parameters are same as in Section 3.2. The antenna is excited by a normally incident cosine-modulated Gaussian plane wave given by

$$\mathbf{E}^{\text{inc}} = \hat{z} e^{-(t-t_{\text{d}}-y/c)^2/2\sigma^2} \cos(\omega_0 (t - t_d - y/c)) \tag{4.8}$$

where $\omega_0/2\pi = 150$ MHz, $\sigma = 0.1/\pi$ μs, and $t_{\text{d}} = 6\sigma$. Less than 0.01% of the incident pulse power is outside the frequency band $[\omega_0 - \omega_{\text{bw}}, \omega_0 + \omega_{\text{bw}}]$, where $\omega_{\text{bw}} = 3/\sigma$. The dipole was divided into 60 equal segments, the circuit had two non-reference nodes, and five harmonics were used, i.e., $N_{\text{EM}} = 59$, $N_{\text{CKT}} = 2$, and $N_{\text{H}} = 5$; in these simulations, $\Delta t = \pi/10\omega_{\text{bw}}$ and $s = 2$. The voltage induced across the diode and the current through it are plotted in Figs. 4.3(b)-4.3(d); the results from envelope-tracking simulations agree well with those obtained from the time-domain method in [25].

To quantify the effectiveness of the proposed schemes, the simulations were repeated for three different excitation bandwidths ($\omega_{\text{bw}}/2\pi = 15\,\text{MHz}, 3\,\text{MHz}$, and 0.75MHz) and for $s = 1,2,4$ using various time-step sizes: $\Delta t = \pi/\beta\omega_{\text{bw}}$, where $\beta \in \{1, 2.5, 5, 7.5, 10, 12.5, 15, 17.5, 20\}$. Larger number of harmonics were used as the time-step size was decreased as recommended in Section 3.2; here, $N_{\text{H}} = 5$ when $\beta < 10$, $N_{\text{H}} = 6$ when $10 \le \beta \le 15$, and $N_{\text{H}} = 7$ when $15 < \beta \le 20$. The errors accrued in these simulations are shown as a function of the time-step size for piecewise constant, piecewise linear, and piecewise quadratic interpolation in Figs. 4.3(e)-4.3(g). In these plots, the error is defined as the root-mean-square error (L2-norm) of the diode current relative to a reference obtained from a more accurate envelope-tracking simulation with $N_{\text{H}} = 9$, $\Delta t = \pi/20\omega_{\text{bw}}$, and $s = 4$. Figs. 4.3(e)-4.3(g) show that simulations with larger s or N_{q} are indistinguishable from the scheme presented in

section 3.2 and [45]–[51] (piecewise constant interpolation with $s = 1$) for the narrowband excitation (4% or 1% bandwidth). The scheme in section 3.1 and [45]–[51] cannot be applied to the broader band case (20% bandwidth) however, (resulting in 100% errors). Figs. 4.3(e)-4.3(g) also show that using larger s allows the envelope-tracking simulation to use smaller time-step sizes, enables this simulation. Figs. 4.3(e)-4.3(g) also show that the errors accrued in the simulations are larger for broader band excitations. Comparing Figs. 4.3(f) and 4.3(g) to 4.3(e) shows that piecewise linear interpolation scheme has similar error trends with the piecewise constant scheme but with slightly lower error levels while piecewise quadratic interpolation (for same s) enables the simulation of a larger range of time-step sizes for the broadband case.

Next, the analysis is repeated for a phase conjugating frequency selective surface formed by an 10×10 array of dipole antennas loaded with Gunn diodes (Fig. 4.4(a)) . The diodes are identical and modeled as a third order nonlinearity $I_{\mathrm{D}} = V_{\mathrm{D}} / 75 + V_{\mathrm{D}}^3 / 2$. The antenna is excited by the same incident field as in the previous case. Each dipole was divided into 60 equal segments, each circuit had one non-reference node, and three harmonics were used, i.e., $N_{\mathrm{EM}} = 5900$, $N_{\mathrm{CKT}} = 100$, and $N_{\mathrm{H}} = 3$; in these simulations, $\Delta t = \pi / 10\omega_{\mathrm{bw}}$ and $s = 2$. The transient voltage induced across the diode G_1 and the current through it are plotted in Figs. 4.4(b)-4.4(d) which again show that the results from envelope-tracking simulations are in good agreement with their time-domain counterparts.

As in the previous example, the simulations were repeated for three different excitation bandwidths ($\omega_{\mathrm{bw}} / 2\pi = 15\,\mathrm{MHz}, 3\,\mathrm{MHz},$ and $0.75\mathrm{MHz}$) and for $s = 1,2,4$ using various time-step sizes : $\Delta t = \pi / \beta\omega_{\mathrm{bw}}$, where $\beta \in \{1, 2.5, 5, 7.5, 10, 12.5, 15, 17.5, 20\}$. Here, as the problem is mildly nonlinear, $N_{\mathrm{H}} = 3$ suffices for reasonable

accuracy and hence used in all the simulations. The errors accrued in these simulations are shown as a function of the time-step size in Figs. 4.4(e)-4.4(g).

In these plots, the error is defined as the root-mean-square error (L2-norm) of the current through the Gunn diode G1 (3.18) relative to a reference obtained from a more accurate envelope tracking simulation with $N_{\mathrm{H}} = 5$, $\Delta t = \pi / 20\omega_{\mathrm{bw}}$, and $s = 4$. Figs. 4.4(e)-4.4(g) show similar trends as Figs. 4.3(e)-4.3(g) that the proposed use of larger s enables the use of smaller time-step size and hence enables the simulation of broader band excitations and the higher order interpolation schemes allow for a larger range of time-step sizes for which the simulations are valid/accurate.

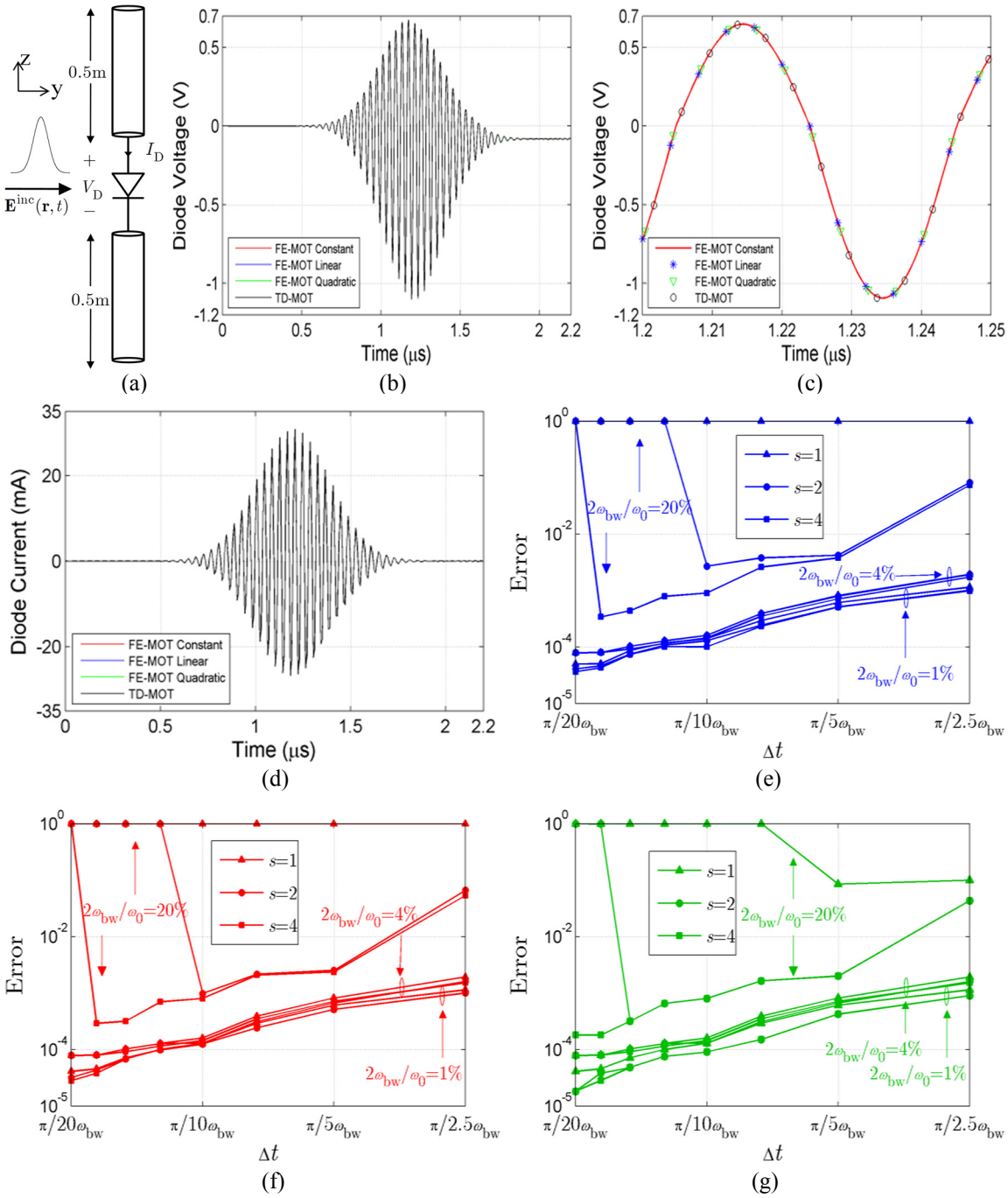

Fig. 4.3. Scattering from dipole antenna loaded with a p-n junction diode. (a) Dipole antenna loaded with a p-n junction diode excited by a normally incident cosine-modulated Gaussian plane wave. (b) Voltage induced across the diode. (c) Voltage near the peak value. (d) Current through the diode. Error versus time-step size using (e) piecewise constant, (f) piecewise linear, and (g) piecewise quadratic interpolation when different sampling instants (4.2) are used. The errors are shown for a narrow-and a broad-band excitation.

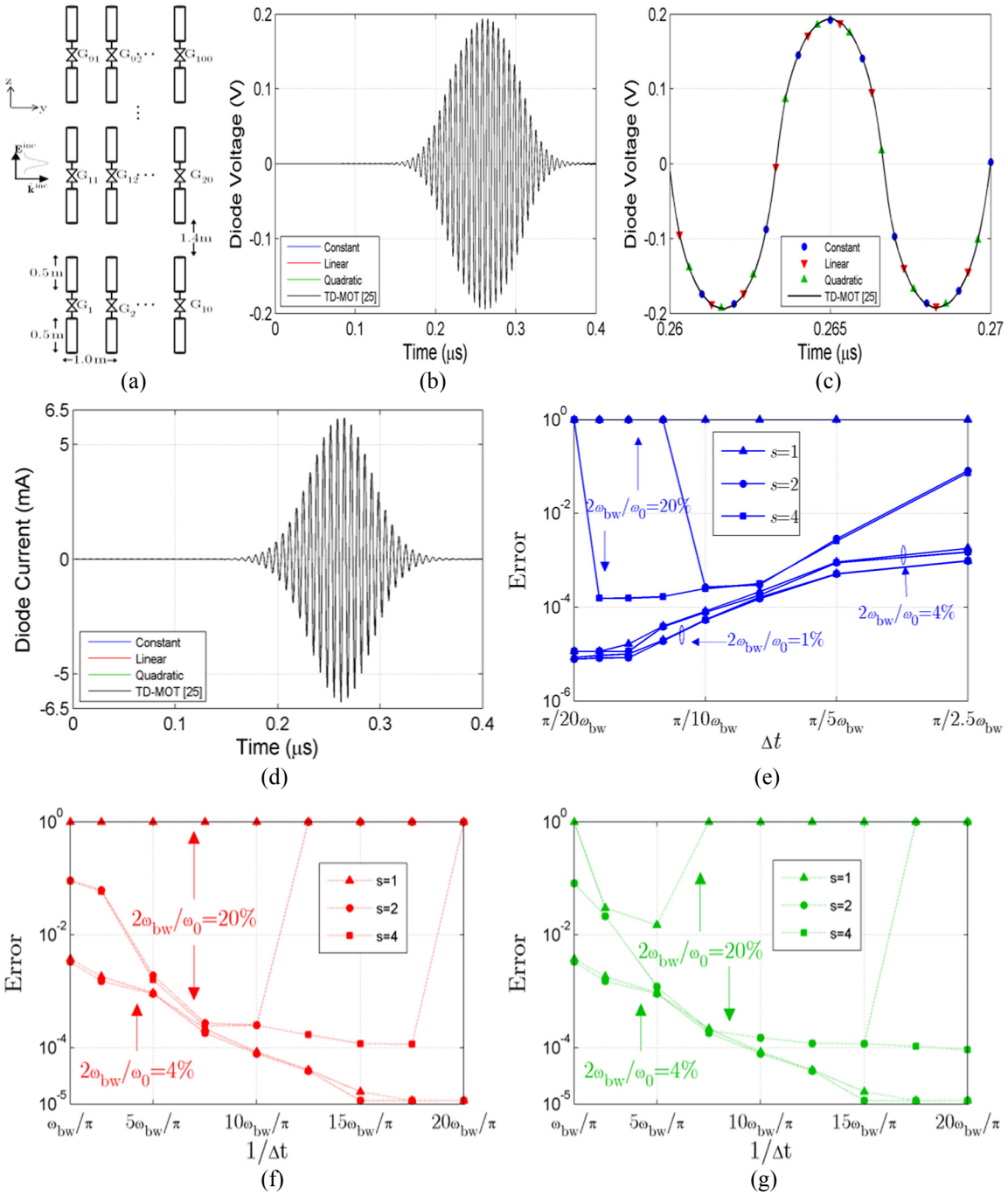

Fig. 4.4. Scattering from phase conjugating array. (a) 100-element array of Gunn-diode loaded dipoles excited by a normally incident cosine-modulated Gaussian plane wave. (b) The voltage across the Gunn diode G_1. (c) Voltage near the peak value. (d) Current through the diode G_1. Error versus time-step size using (e) piecewise constant, (f) piecewise linear, and (g) piecewise quadratic interpolation when different sampling instants (s) are used. The errors are shown for a narrow- and broad-band excitation.

CHAPTER 5

FOURIER ENVELOPE EM-CKT SIMULATOR FOR NONLINEARLY LOADED ANTENNAS AND ACTIVE MICROWAVE CIRCUITS

In this chapter, the envelope tracking hybrid EM-CKT simulator described in Chapter 3 is extended to include arbitrarily shaped dielectric and PEC bodies. The problem statement and the formulation are presented in Section 5.1. Section 5.2 presents a Fourier envelope-adaptive integral method (FE-AIM) to reduce the computational complexity of the simulator. Section 5.3 presents sparse near field preconditioning schemes used for improving the convergence of the nonlinear solution algorithm. Numerical results that highlight the various features of the algorithm are presented in Section 5.4.

5.1 FORMULATION

Consider arbitrarily shaped lossless dielectric with permittivity $\varepsilon(\mathbf{r})$ and PEC bodies that are loaded with nonlinear time-invariant devices at various locations. The structure is assumed to reside in an unbounded homogeneous medium with permittivity ε and permeability μ. Similar to the wire antennas, the structure is excited by a combination of an electric field $\mathbf{E}^{\text{inc}}(\mathbf{r},t)$ due to external impressed sources and voltage sources $VS_1(t), VS_2(t),\ldots$ and current sources $IS_1(t), IS_2(t),\ldots$ within the lumped circuits. The incident electric field on the wires is assumed to be zero for $t \le 0$ and essentially bandlimited to the angular frequency band $[\omega_0 - \omega_{\text{bw}}, \omega_0 + \omega_{\text{bw}}]$, where ω_0 is the fundamental carrier frequency and ω_{bw} is the single-sided bandwidth. All sources within the devices are assumed to be either DC sources or initially zero and essentially bandlimited just like the incident electric field.

5.1.1 EM Equations

To model the field interactions with the EM structure, the boundary conditions on the electric field are enforced. On the PEC surface S, the zero time derivative of the total electrical field tangential to S is enforced. On the dielectric volume V, the time derivative of the electric field is expressed as a sum of the time derivatives of incident and scattered field: [25]

$$\begin{aligned}
\hat{n}\times\hat{n}\times\partial_t\mathbf{E}^{\mathrm{inc}}(\mathbf{r},t) &= \hat{n}\times\hat{n}\times[\nabla\partial_t\phi_{\mathrm{S}}(\mathbf{r},t)+\partial_t^2\mathbf{A}_{\mathrm{S}}(\mathbf{r},t)] \qquad \mathbf{r}\in S\\
&\quad +\hat{n}\times\hat{n}\times[\nabla\partial_t\phi_{\mathrm{V}}(\mathbf{r},t)+\partial_t^2\mathbf{A}_{\mathrm{V}}(\mathbf{r},t)]\\
\partial_t\mathbf{E}^{\mathrm{inc}}(\mathbf{r},t) &= \partial_t\mathbf{E}(\mathbf{r},t)+[\nabla\partial_t\phi_{\mathrm{V}}(\mathbf{r},t)+\partial_t^2\mathbf{A}_{\mathrm{V}}(\mathbf{r},t)] \quad \mathbf{r}\in V\\
&\quad +[\nabla\partial_t\phi_{\mathrm{S}}(\mathbf{r},t)+\partial_t^2\mathbf{A}_{\mathrm{S}}(\mathbf{r},t)]
\end{aligned} \tag{5.1}$$

Here, $\mathbf{A}_{\mathrm{S}}(\phi_{\mathrm{S}})$ denotes the magnetic vector (electric scalar) potential due to the currents induced on the surface of the PEC, $\mathbf{A}_{\mathrm{V}}(\phi_{\mathrm{V}})$ denotes the magnetic vector (electric scalar) potential due to the polarization currents induced in the volume of the dielectric and $\hat{n}$ is the outward pointing unit vector normal to S, $\mathbf{E}$ represents the total electric field in the dielectric volume.

Next, the electric fields and induced current densities are expanded using a truncated series with N_{H} terms (harmonics):

$$\begin{aligned}
\mathbf{E}^{\mathrm{inc}}(\mathbf{r},t) &\cong \mathrm{Re}\left(\sum_{h=0}^{N_{\mathrm{H}}-1}\tilde{\mathbf{E}}^{\mathrm{inc},h}(\mathbf{r},t)e^{jh\omega_0 t}\right)\\
\mathbf{J}_{\mathrm{S}}(\mathbf{r},t) &\cong \mathrm{Re}\left(\sum_{h=0}^{N_{\mathrm{H}}-1}\tilde{\mathbf{J}}_{\mathrm{S}}^{h}(\mathbf{r},t)e^{jh\omega_0 t}\right) \qquad \mathbf{r}\in S\\
\mathbf{J}_{\mathrm{V}}(\mathbf{r},t) &\cong \mathrm{Re}\left(\sum_{h=0}^{N_{\mathrm{H}}-1}\tilde{\mathbf{J}}_{\mathrm{V}}^{h}(\mathbf{r},t)e^{jh\omega_0 t}\right) \qquad \mathbf{r}\in V\\
\mathbf{E}(\mathbf{r},t) &\cong \mathrm{Re}\left(\sum_{h=0}^{N_{\mathrm{H}}-1}\tilde{\mathbf{E}}^{h}(\mathbf{r},t)e^{jh\omega_0 t}\right) \qquad \mathbf{r}\in V
\end{aligned} \tag{5.2}$$

Henceforth, $\tilde{\mathbf{E}}^{\mathrm{inc},h}$, $\tilde{\mathbf{E}}^{h}$ $\tilde{\mathbf{J}}_{\mathrm{S}}^{h}$, and $\tilde{\mathbf{J}}_{\mathrm{V}}^{h}$ are referred as the h^{th} envelope of the incident electric field, total electric field, induced surface current density and induced polarization current density, respectively. By substituting (5.2) in (5.1), the EFIE is converted to N_{H} independent integral equations; each equation relates one of the envelopes of the current and the incident field. They are expressed as

$$\begin{aligned}
\hat{n}\times\hat{n}\times(\partial_t + jh\omega_0)\tilde{\mathbf{E}}^{\mathrm{inc},h} &= \hat{n}\times\hat{n}\times[\nabla(\partial_t + jh\omega_0)(\tilde{\phi}_{\mathrm{S}}^{h} + \tilde{\phi}_{\mathrm{V}}^{h}) + \\
&\qquad (\partial_t^2 + 2jh\omega_0\partial_t - h^2\omega_0^2)(\tilde{\mathbf{A}}_{\mathrm{S}}^{h} + \tilde{\mathbf{A}}_{\mathrm{V}}^{h}) \qquad \mathbf{r}\in S \\
(\partial_t + jh\omega_0)\tilde{\mathbf{E}}^{\mathrm{inc},h} &= (\partial_t + jh\omega_0)\tilde{\mathbf{E}}^{h} + [\nabla(\partial_t + jh\omega_0)(\tilde{\phi}_{\mathrm{S}}^{h} + \tilde{\phi}_{\mathrm{V}}^{h}) + \\
&\qquad (\partial_t^2 + 2jh\omega_0\partial_t - h^2\omega_0^2)(\tilde{\mathbf{A}}_{\mathrm{S}}^{h} + \tilde{\mathbf{A}}_{\mathrm{V}}^{h})] \qquad \mathbf{r}\in V
\end{aligned} \tag{5.3}$$

for $h = 0,\ldots,N_{\mathrm{H}}-1$. Here, the envelopes of the potentials are given by

$$\begin{aligned}
(\partial_t + jh\omega_0)\tilde{\phi}_{\mathrm{S}}^{h}(\mathbf{r},t) &= -\iint_S \nabla'\bullet\tilde{\mathbf{J}}_{\mathrm{S}}^{h}(\mathbf{r}',t-R/c)\frac{e^{-jhk_0R}}{4\pi\varepsilon R}ds' \\
\tilde{\mathbf{A}}_{\mathrm{S}}^{h}(\mathbf{r},t) &= \mu\iint_S \tilde{\mathbf{J}}_{\mathrm{S}}^{h}(\mathbf{r}',t-R/c)\frac{e^{-jhk_0R}}{4\pi R}ds' \\
(\partial_t + jh\omega_0)\tilde{\phi}_{\mathrm{V}}^{h}(\mathbf{r},t) &= -\iiint_V \nabla'\bullet\tilde{\mathbf{J}}_{\mathrm{V}}^{h}(\mathbf{r}',t-R/c)\frac{e^{-jhk_0R}}{4\pi\varepsilon R}dv' \\
\tilde{\mathbf{A}}_{\mathrm{V}}^{h}(\mathbf{r},t) &= \mu\iiint_V \tilde{\mathbf{J}}_{\mathrm{V}}^{h}(\mathbf{r}',t-R/c)\frac{e^{-jhk_0R}}{4\pi R}dv'
\end{aligned} \tag{5.4}$$

In (5.4), $R = |\,\mathbf{r}-\mathbf{r}'\,|$ is the distance between the source and the observer point, $c = (\mu\varepsilon)^{-1/2}$ is the speed of light in the background medium, and $k_0 = \omega_0 / c$ is the wave number at the fundamental carrier frequency.

In order to solve (5.3) numerically, (i) the surface S are discretized using triangular meshes with N_{S} internal edges, (ii) the edges at the N_{D} (finite-gap) CKT ports are labeled as $2N_{\mathrm{gap}}$ port edges and (iii) the volume V are meshed using

tetrahedral elements with N_{V} faces. Next, the envelopes of the induced currents are approximated using $N_{\mathrm{T}}N_{\mathrm{EM}}$ temporal-spatial basis functions as

$$\begin{aligned}\tilde{\mathbf{J}}_{\mathrm{S}}^{h}(\mathbf{r},t) &\cong \sum_{l'=1}^{N_{\mathrm{T}}}\sum_{k'=1}^{N_{\mathrm{S}}} \tilde{\mathbf{I}}_{l'}^{\mathrm{EM},h}[k']\mathbf{S}_{k'}(\mathbf{r})T_{l'}(t) + \sum_{l'=1}^{N_{\mathrm{T}}}\sum_{k'=1}^{N_{\mathrm{gap}}} \tilde{\mathbf{I}}_{l'}^{\mathrm{EM},h}[N_{\mathrm{S}}+k']\mathbf{P}_{k'}(\mathbf{r})T_{l'}(t) \\ \tilde{\mathbf{J}}_{\mathrm{V}}^{h}(\mathbf{r},t) &\cong \sum_{l'=1}^{N_{\mathrm{T}}}\sum_{k'=1}^{N_{\mathrm{V}}} \kappa(\mathbf{r})\tilde{\mathbf{I}}_{l'}^{\mathrm{EM},h}[N_{\mathrm{S}}+N_{\mathrm{gap}}+k']\mathbf{V}_{k'}(\mathbf{r})\partial_t T_{l'}(t)\end{aligned} \tag{5.5}$$

Here, $\tilde{\mathbf{I}}_{l'}^{\mathrm{EM},h}$ is an $N_{\mathrm{EM}}\times 1$ vector that stores unknown coefficients, $\mathbf{S}_{k'},\mathbf{P}_{k'},\mathbf{V}_{k'}$ are the spatial and $T_{l'}(t)=T(t-l'\Delta t)$ are the temporal basis functions, $N_{\mathrm{EM}}=N_{\mathrm{S}}+N_{\mathrm{gap}}+N_{\mathrm{V}}$ is the number of spatial and N_{T} is the number of temporal basis functions, $\kappa(\mathbf{r})=1-\varepsilon\,/\,\varepsilon(\mathbf{r})$ is the contrast ratio and Δt is the time step size. The spatial basis functions are (i) divergence conforming first order basis functions i.e., $\mathbf{S}_{1,\ldots N_{\mathrm{S}}}$ are RWG functions defined over edges of two adjoining triangles [71]; $\mathbf{V}_{1,\ldots,N_{\mathrm{V}}}$ are SWG functions defined over tetrahedrons [72] and (ii) $\mathbf{P}_{1,\ldots,N_{\mathrm{gap}}}$ are port basis functions defined on the $2N_{\mathrm{gap}}$ used to enforce current continuity in the finite-gap ports. The port basis functions will be explained in subsection 5.1.3. The temporal basis functions are chosen as causal piecewise polynomial interpolatory functions [67]. Substituting (5.5) in (5.4) and Galerkin-testing with $\mathbf{S}_{k'},\mathbf{P}_{k'},\mathbf{V}_{k'}$ testing the resulting equations at times $\Delta t,\ldots,N_{\mathrm{T}}\Delta t$ yields:

$$\tilde{\mathbf{Z}}_0\tilde{\mathbf{I}}_l^{\mathrm{EM}} = \tilde{\mathbf{V}}_l^{\mathrm{EM}} - \sum_{l'=\max(1,l-N_{\mathrm{g}})}^{l-1} \tilde{\mathbf{Z}}_{l-l'}\tilde{\mathbf{I}}_{l'}^{\mathrm{EM}} \text{ for } l=1,\ldots,N_{\mathrm{T}} \tag{5.6}$$

Here again as in the case of wires, $\tilde{\mathbf{I}}_{l'}^{\mathrm{EM}}$ is an $N_{\mathrm{H}}N_{\mathrm{EM}}\times 1$ vector that concatenates the unknown samples of the current envelopes at time $l'\Delta t$, i.e., $\tilde{\mathbf{I}}_{l'}^{\mathrm{EM}}[hN_{\mathrm{EM}}+1:(h+1)N_{\mathrm{EM}}]=\tilde{\mathbf{I}}_{l'}^{\mathrm{EM},h}[1:N_{\mathrm{EM}}]$ for $h=0,\ldots,N_{\mathrm{H}}-1$. Similarly, $\tilde{\mathbf{V}}_l^{\mathrm{EM}}$ is the vector that contains all the incident electric field envelopes tested at time $l\Delta t$. The matrices $\tilde{\mathbf{Z}}_{l-l'}$, which are of size $N_{\mathrm{H}}N_{\mathrm{EM}}\times N_{\mathrm{H}}N_{\mathrm{EM}}$, give the scattered field

envelopes tested at time $l\Delta t$ due to the current envelope samples at time $l'\Delta t.$. In (5.6), $N_{\mathrm{g}} = \left\lfloor R_{\max} / c\Delta t + l_{\max} \right\rfloor$ where $R_{\max}$ is the maximum distance between any two points on the EM module and $l_{\max}$ is the length of the temporal basis function in terms of Δt. Due to the linearity of EFIE, the equations corresponding to different harmonics in (5.6) are decoupled (each $\tilde{\mathbf{Z}}_{l-l'}$ matrix is block diagonal with N_{H} diagonal blocks of size $N_{\mathrm{EM}} \times N_{\mathrm{EM}}$); thus, the samples of each current envelope can be found independently, one envelope at a time. But when loaded by nonlinear devices, however, the equations for the different harmonics become coupled (through port currents and voltages); thus, the full system of equations (5.6) must be solved simultaneously at each time step; i.e., the samples of all current envelopes at each time step must be found together.

5.1.2 CKT Equations

The CKT equations is identical to that described in Chapter 2 and Section 3.1.2. The resulting equations are the same as (2.19) and repeated here for brevity.

$$\tilde{\mathbf{Y}}^{\mathrm{CKT}}\tilde{\mathbf{V}}_l^{\mathrm{CKT}} + \tilde{\mathbf{I}}_l^{\mathrm{nl}}(\tilde{\mathbf{V}}_l^{\mathrm{CKT}}) = \tilde{\mathbf{I}}_l^{\mathrm{CKT}} \tag{5.7}$$

5.1.3 Coupling EM-CKT Equations – Finite Gap Port Models

The EM structure and devices are coupled using the port model similar to the time domain ones described in [24], [25] and similar to that described in Sections 3.1.3. However, when there are gaps in the EM module, this port model (referred to as delta gap model) fills the gap with artificial PECs which are discretized using RWG functions. This model is simple as it uses the regular RWG functions, but it doesn't allow for fringing fields. The accuracy of this model is also sensitive to the refinement of the mesh and the mesh size [73], [74]. Here, a novel finite gap port model is used to model the port which

enforces continuity of the currents and enforces the line integral of the electric field in the gap is equal to the port voltage (in a weak sense).

As an example, let the first circuit representing a two terminal device is connected to the first finite gap port that occupies a rectangular gap $S_{\mathrm{gap},1}$ of length $l_{\mathrm{gap},1}$ and width $h_{\mathrm{gap},1}$ in the EM structure and be connected at nodes P and 0 as shown in Fig. 5.1(a). Hereafter, in this example, the top edge of the PEC is referred to as the positive edge and the bottom edge is referred to as the negative edge. To enforce (i) the equality of the current exiting the positive edge and that entering the negative edge and (ii) there is no scattering from the gap, all the port basis functions $\mathbf{P}_{1,\ldots,N_{\mathrm{gap}}}$ (Fig. 5.1(b)) are chosen to be defined as two *disconnected* half RWGs on triangles with the positive edge and negative edge of the port with the same coefficients. Next, the coupling from the device to the PEC surface is modeled by enforcing the average line integral of the electric field in the gap is equal to the port voltage (Fig. 5.2(c)), i.e. the envelopes of the time-derivative of the electric field in the port gap is set as

$$\frac{1}{l_{\mathrm{gap},1}} \iint_{S_{\mathrm{gap},1}} (\partial_t + jh\omega_0)(\tilde{\mathbf{E}}^{\mathrm{sca},h}(\mathbf{r},t) + \tilde{\mathbf{E}}^{\mathrm{inc},h}(\mathbf{r},t))\bullet\hat{h}_1 dhdl = (\partial_t + jh\omega_0)\tilde{V}_P^{1,h}(t) \tag{5.8}$$

Here, $\hat{h}_1$ is the unit vector along the positive edge to the negative edge of the first port-basis function. Here, again, the time derivative of the port voltage $\partial_t \tilde{V}_P^{1,h}$ is approximated by a third-order backward difference formula just as in [24], [25]. Using (5.5) in (5.8) and enforcing them at time $l\Delta t$ for all port basis, yields for $l = 1,\ldots,N_{\mathrm{T}}$

$$\tilde{\mathbf{Z}}_0^{\mathrm{port}}\tilde{\mathbf{I}}_l^{\mathrm{EM}} - \tilde{\mathbf{C}}_0^{\mathrm{V}}\tilde{\mathbf{V}}_l^{\mathrm{CKT}} = \tilde{\mathbf{V}}_l^{\mathrm{port}} - \sum_{l'=l-3}^{l-1} \tilde{\mathbf{C}}_{l-l'}^{\mathrm{V}}\tilde{\mathbf{V}}_{l'}^{\mathrm{CKT}} - \sum_{l'=\max(1,l-N_{\mathrm{g}})}^{l-1} \tilde{\mathbf{Z}}_{l-l'}^{\mathrm{port}}\tilde{\mathbf{I}}_{l'}^{\mathrm{EM}} \tag{5.9}$$

Here, $\tilde{\mathbf{Z}}_{l-l'}^{\mathrm{port}}$ are block diagonal matrix which stores the scattered field component of left hand side in (5.8) at time $l\Delta t$ due to the currents at time $l'\Delta t$ and $\tilde{\mathbf{V}}_l^{\mathrm{port}}$ stores the

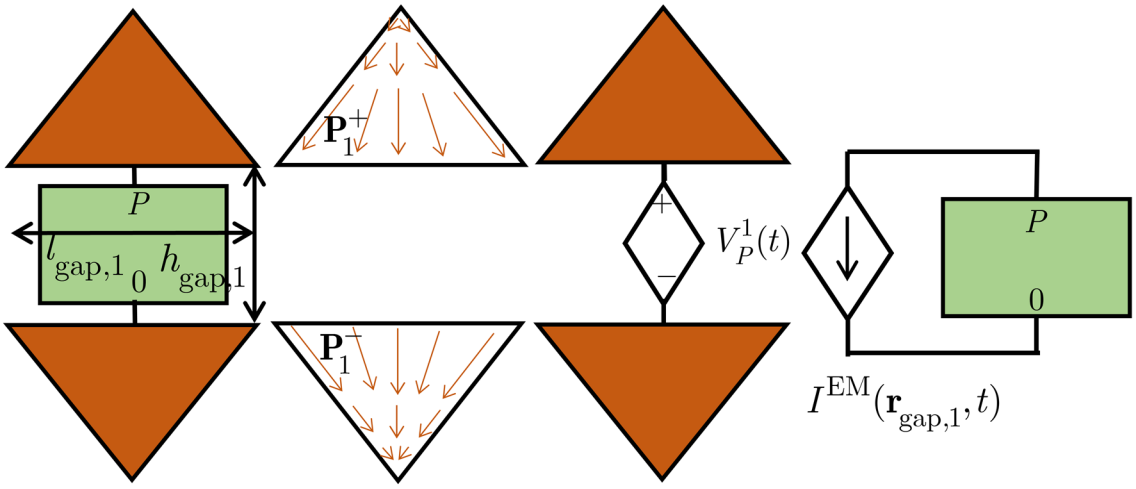

Fig. 5.1. EM-CKT coupling using non-radiative finite gap port model (a) One port circuit connected to the PEC surfaes at node P and the reference node. (b) Port basis function (c) EM model (d) CKT model.

contribution of incident fields in (5.8) at time $l\Delta t$. The port model equation (5.8) can be expressed as the tested envelope of the electric fields where the testing function is given by $\mathbf{P}_1^{\text{gap}}(\mathbf{r}) = \hat{h}$ for $\mathbf{r} \in S_{\text{gap}}$ and 0 elsewhere. Also, the Galerkin testing of the electric field equations on triangular patches of the port in (5.6) along with (5.9) can be expressed as a divergence conforming testing function of the electric field at the ports . Also, note that if $h_{\text{gap},1} \to 0$, the port equations yield the same equation as coupling described in [24], [25] and Section 3.1.3

The coupling from the PEC surfaces to the device is modeled similar to the case of wires (Fig. 5.2(d)) by assuming that all the current exiting the positive edge enters the negative edge through the circuit, i.e. by adding for $h = 0, \ldots, N_{\text{H}} - 1$ to the Kirchhoff's current law at node at node P in the middle of the basis function $\mathbf{P}_1(\mathbf{r}_{\text{gap},1})$. Here, $\tilde{I}^{\text{EM},h}(\mathbf{r}_{\text{gap},1}, t) = l_{\text{gap}} \tilde{\mathbf{J}}_{\text{S}}^{\text{EM},h}(\mathbf{r}_{\text{gap},1}, t) \bullet \hat{h}$. If there are DC sources in the circuits, a two-step DC analysis is performed and the coupling scheme is modified accordingly. This is identical to the procedure described in Section 3.1.3.Also, there can be more than one gap

edge associated with one device port. The extension is straightforward using the scheme described in [24]. The coupled system of equations can be expressed as

$$\tilde{\mathbf{F}}(\tilde{\mathbf{X}}_l) = \tilde{\mathbf{b}}_l \quad \text{for } l = 1,\ldots,N_{\mathrm{T}} \tag{5.10}$$

where

$$\tilde{\mathbf{F}}(\tilde{\mathbf{X}}_l) = \begin{bmatrix} \tilde{\mathbf{Z}}_0^{\mathrm{EM}} + \tilde{\mathbf{Z}}_0^{\mathrm{port}} & \tilde{\mathbf{C}}_0^{\mathrm{V}} \\ -\tilde{\mathbf{C}}^{\mathrm{I}} & \tilde{\mathbf{Y}}^{\mathrm{CKT}} \end{bmatrix} \underbrace{\begin{bmatrix} \tilde{\mathbf{I}}_l^{\mathrm{EM}} \\ \tilde{\mathbf{V}}_l^{\mathrm{CKT}} \end{bmatrix}}_{\tilde{\mathbf{X}}_l} + \begin{bmatrix} 0 \\ \tilde{\mathbf{I}}_l^{\mathrm{nl}}(\tilde{\mathbf{V}}_l^{\mathrm{CKT}}) \end{bmatrix} \tag{5.11}$$

and

$$\tilde{\mathbf{b}}_l = \begin{bmatrix} \tilde{\mathbf{V}}_l^{\mathrm{EM}} + \tilde{\mathbf{V}}_l^{\mathrm{port}} - \sum_{l'=\max(1,l-N_{\mathrm{g}})}^{l-1} (\tilde{\mathbf{Z}}_{l-l'}^{\mathrm{EM}} + \tilde{\mathbf{Z}}_{l-l'}^{\mathrm{port}})\tilde{\mathbf{I}}_{l'}^{\mathrm{EM}} - \sum_{l'=l-3}^{l-1} \tilde{\mathbf{C}}_{l-l'}^{\mathrm{V}} \tilde{\mathbf{V}}_{l'}^{\mathrm{CKT}} \\ \tilde{\mathbf{I}}_l^{\mathrm{CKT}} \end{bmatrix} \tag{5.12}$$

The entries of the matrices and vectors in (5.11) and (5.12) are listed in Appendix V.

5.1.4 Solution Algorithm

A multidimensional nonlinear solution algorithm is used to solve (5.10) because of the $\tilde{\mathbf{I}}_l^{\mathrm{nl}}(\tilde{\mathbf{V}}_l^{\mathrm{CKT}})$ term that represents the equations governing the nonlinear CKT elements. The algorithm is same as the one presented in the Section 3.1.4 along with the improvements presented in Chapter 4.

5.1.5 Computational Costs

As in the case of wires, the number of non-zero entries in $\tilde{\mathbf{Z}}_0^{\mathrm{EM}}$ matrix is denoted by $N_{\mathrm{H}}N_0$. $\tilde{\mathbf{Y}}^{\mathrm{CKT}}$ is assumed to have a total of $O(N_{\mathrm{H}}N_{\mathrm{CKT}})$ nonzero entries and the total number of nonlinear elements is denoted by $N_{\mathrm{CKT}}^{\mathrm{nl}}$ and the Jacobian matrix $\tilde{\tilde{\mathbf{J}}}_{l,p}^{\mathrm{nl}}$ is assumed to have $O(N_{\mathrm{H}}^2 N_{\mathrm{CKT}}^{\mathrm{nl}})$ nonzero entries. The average number of Newton iterations needed per time step is denoted by $\bar{N}_{\mathrm{N}}$.

In the first step of the FE-MOT scheme, the vector $\tilde{\mathbf{b}}_l$ is computed; this requires $O(N_{\mathrm{H}}(N_{\mathrm{EM}}^2 + N_{\mathrm{CKT}}))$ operations per time step In the second step, the Newton iterations are started and the residual is computed. Finding the contribution from the linear and nonlinear parts of $\tilde{\mathbf{F}}$ to the residual requires $O(N_{\mathrm{H}}(N_0 + N_{\mathrm{CKT}}))$ and $O(N_{\mathrm{CKT}}^{\mathrm{nl}} N_{\mathrm{H}}^2)$ operations, respectively. A total of $O(\bar{N}_{\mathrm{N}} N_{\mathrm{H}}(N_0 + N_{\mathrm{CKT}} + N_{\mathrm{H}} N_{\mathrm{CKT}}^{\mathrm{nl}}))$ operations per time step are required to compute the residual at each time step. In the fourth step, the Jacobian matrices are filled; this requires $O(\bar{N}_{\mathrm{N}} N_{\mathrm{H}}^2 N_{\mathrm{CKT}}^{\mathrm{nl}})$ operations per time step. In the last step, the linear solve requires $O(\bar{N}_{\mathrm{N}} \bar{N}_{\mathrm{I}} N_{\mathrm{H}}$ $(N_0 + N_{\mathrm{CKT}} + N_{\mathrm{H}} N_{\mathrm{CKT}}^{\mathrm{nl}}))$ operations per time step; here, $\bar{N}_{\mathrm{I}}$ is the average number of iterations needed to solve the linear equation per Newton iteration per time step. Thus, the marching time, scales as $O(N_{\mathrm{T}}[N_{\mathrm{H}} N_{\mathrm{EM}}^2 + \bar{N}_{\mathrm{N}} \bar{N}_{\mathrm{I}} N_{\mathrm{H}} N_0 +$ $\bar{N}_{\mathrm{N}} N_{\mathrm{H}}^2 N_{\mathrm{CKT}}^{\mathrm{nl}} + \bar{N}_{\mathrm{N}} \bar{N}_{\mathrm{I}} N_{\mathrm{H}} N_{\mathrm{CKT}}])$. For narrowband analysis, $N_0 \approx N_{\mathrm{EM}}^2$ [35] and typically $\bar{N}_{\mathrm{I}} \gg N_{\mathrm{H}}$; thus, the iterative solution in the fifth step dominates. Assuming $N_{\mathrm{CKT}}^{\mathrm{nl}} \approx N_{\mathrm{CKT}}$ (as is the case in all the examples in Section 5.4), the marching time scales as $O(N_{\mathrm{T}} \bar{N}_{\mathrm{N}} \bar{N}_{\mathrm{I}}[N_{\mathrm{H}} N_{\mathrm{EM}}^2 + N_{\mathrm{H}}^2 N_{\mathrm{CKT}}])$. The remaining major computational costs of the FE-MOT scheme are the time required to fill the matrices in (5.11) and (5.12) the memory required to store them which scale as $O(N_{\mathrm{H}}[N_{\mathrm{EM}}^2 + N_{\mathrm{CKT}}])$ and $O(N_{\mathrm{H}}[N_{\mathrm{EM}}^2 + N_{\mathrm{g}} N_{\mathrm{EM}} + N_{\mathrm{CKT}}])$.

There are two issues which make these computational cost prohibitive: (i) typically, as with time-domain counterparts, N_{EM} is very large compared to the wire problems and the computational costs make FE-MOT prohibitive for moderate and large problems. (ii) the convergence of the iterative solver solving the coupled system of equations is poor when $\tilde{\mathbf{Z}}_0^{\mathrm{EM}}$ is nearly full (for narrowband problems as here) and $\bar{N}_{\mathrm{I}}$ is

large. Adaptive integral method and sparse near-field preconditioners are used to alleviate these two issues as explained next.

5.2 FOURIER ENVELOPE ADAPTIVE INTEGRAL METHOD (FE-AIM)

To accelerate the simulations, as in pure envelope tracking EM simulators [52] and hybrid time-domain EM-CKT simulators [24], [25], a fast algorithm has to be applied. Here, envelope tracking AIM [52] is used which approximates the interaction between source and observers (separated by a distance larger than a threshold) with point sources on a regular grid with N_{C} points. FE-AIM algorithm is an extension of the envelope tracking AIM [52] and similar to the time-domain AIM algorithms [25], [53]. FE-AIM is formulated by introducing a 3-D regular grid of N_{C} auxiliary nodes that encloses the microwave antenna or circuit. Note that, in general, there can be N_{H} different auxiliary grids as each of the N_{H} harmonics can have a different 3-D grid. However, here only one auxiliary grid is used for all harmonics for simplicity.

Using the auxiliary grid, for each harmonic $h = 0,\ldots,N_{\mathrm{H}}-1$, the FE-AIM procedure approximates the N_{H} ($N_{\mathrm{EM}} \times N_{\mathrm{EM}}$ sized) block diagonal entries of impedance matrices $\tilde{\mathbf{Z}}_{l-l'}^{\mathrm{imp}} = \tilde{\mathbf{Z}}_{l-l'}^{\mathrm{EM}} + \tilde{\mathbf{Z}}_{l-l'}^{\mathrm{port}}$ i.e. $\tilde{\mathbf{Z}}_{l-l'}^{\mathrm{imp},h,h} \approx \tilde{\mathbf{Z}}_{l-l'}^{\mathrm{FFT},h,h} + \tilde{\mathbf{Z}}_{l-l'}^{\mathrm{near},h,h}$ where

$$\tilde{\mathbf{Z}}_{l-l'}^{\mathrm{FFT},h,h} = \sum_{i\in\{x,y,z\}} [\Lambda_i^{\mathrm{int}} \tilde{\mathbf{G}}_{l-l'}^{\mathrm{A},h} \Lambda_i^{\mathrm{ant}} + \Lambda_\nabla^{\mathrm{ant}\dagger} \tilde{\mathbf{G}}_{l-l'}^{\phi,h} \Lambda_\nabla^{\mathrm{ant}}] \tag{5.13}$$

Here, the reduction in the computational cost is obtained by storing and multiplying the sparse anterpolation [54], [75] ($\Lambda_{x,y,z,\nabla}^{\mathrm{ant}}$), propagation matrices ($\tilde{\mathbf{G}}_{l-l'}^{A,h}, \tilde{\mathbf{G}}_{l-l'}^{\phi,h}$) and interpolation matrices ($\Lambda_{x,y,z,\nabla}^{\mathrm{int}}$) instead of explicitly computing $\tilde{\mathbf{Z}}_{l-l'}^{\mathrm{FFT},h,h}$. In (5.13), the anterpolation matrices $\Lambda_{x,y,z,\nabla}^{\mathrm{ant}}$ represent the fields radiated by basis functions in terms of those radiated by point sources on the auxiliary grid; they are obtained using the method followed in [52], [53] by matching the multipole moments of the Cartesian co-ordinate

components of $\{\mathbf{S}_{k'}, \mathbf{P}_{k'}, \mathbf{V}_{k'}\}$ and those of $\{\nabla\bullet\mathbf{S}_{k'}, \nabla\bullet\mathbf{P}_{k'}, \nabla\bullet\mathbf{V}_{k'}\}$, typically to an order of 1 to 5 [52]–[54], [76]. The interpolation matrices $\Lambda^{\mathrm{int}}_{x,y,z,}$ and $\Lambda^{\mathrm{int}}_{\nabla}$ represent the fields interpolated from point observers on the auxiliary grid to the testing functions; they are also obtained by matching the multipole moments of the Cartesian coordinate components of $\{\mathbf{S}_k, \mathbf{P}_k + \mathbf{P}^{\mathrm{gap}}_k, \mathbf{V}_k\}$ and $\{\nabla\bullet\mathbf{S}_{k'}, \nabla\bullet\mathbf{P}_{k'}, \nabla\bullet\mathbf{V}_{k'}\}$ to the same order as the anterpolation matrices. The entries of the propagation matrices are

$$\begin{aligned}
\tilde{\mathbf{G}}^{\mathrm{A},h}_{l-l'}[u,u'] &= \left\{(\partial_t^2 + 2jh\omega_0\partial_t - h^2\omega_0^2)\mu\right\}\frac{T(t-\left|\mathbf{r}-\mathbf{r}_{u'}\right|/c)}{4\pi\left|\mathbf{r}-\mathbf{r}_{u'}\right|}e^{-jhk_0\left|\mathbf{r}-\mathbf{r}_{u'}\right|}\Big|_{\substack{\mathbf{r}=\mathbf{r}_u \\ t=(l-l')\Delta t}} \\
\tilde{\mathbf{G}}^{\phi,h}_{l-l'}[u,u'] &= \frac{1}{\varepsilon}\frac{T(t-\left|\mathbf{r}-\mathbf{r}_{u'}\right|/c)}{4\pi\left|\mathbf{r}-\mathbf{r}_{u'}\right|}e^{-jhk_0\left|\mathbf{r}-\mathbf{r}_{u'}\right|}\Big|_{\substack{\mathbf{r}=\mathbf{r}_u \\ t=(l-l')\Delta t}}
\end{aligned} \tag{5.14}$$

for $h = 0,\ldots,N_{\mathrm{H}}-1$. Here, $\{u,u'\} \in 1,\ldots,N_{\mathrm{C}}$,$\{\mathbf{r}_u, \mathbf{r}_{u'}\}$ represent the observer and source positions on the auxiliary grid. Because of the space-time shift invariance of the free-space Green function [52], [53], the propagation matrices are in block-Toeplitz form and can be multiplied with vectors using FFTs. Blocked 4-D space-time FFTs with varying temporal FFT sizes [52], [53] are used to multiply the propagation matrices for which $l-l' \neq 0$ during marching in time. 3-D space FFTs are used to multiply $\tilde{\mathbf{G}}^{A,h}_0$ and $\tilde{\mathbf{G}}^{\phi,h}_0$ during the iterative solution similar to [52], [77].

The near-zone correction matrices $\tilde{\mathbf{Z}}^{\mathrm{near},h,h}_{l-l'}$ for $h = 0,\ldots,N_{\mathrm{H}}-1$ are needed to be stored and multiplied at each time-step. The entries of these "pre-corrected" matrices [54], [78] are: for $h = 0,\ldots,N_{\mathrm{H}}-1$

$$\tilde{\mathbf{Z}}^{\mathrm{near},h,h}_{l-l'}[k,k'] = \begin{cases} \tilde{\mathbf{Z}}^{\mathrm{EM},h,h}_{l-l'}[k,k'] - \tilde{\mathbf{Z}}^{\mathrm{FFT},h,h}_{l-l'}[k,k'] & R[k,k'] < \gamma\Delta \\ 0 & \mathrm{otherwise} \end{cases} \tag{5.15}$$

Here, Δ is the grid spacing, and γ is an integer that sets the near-zone size; typically $1 \leq \gamma \leq 6$ [52], $R[k,k']$is the minimum distance between the spatial basis functions k and k'. For narrowband analysis, the distance traveled in one time step ($c\Delta t$) is much larger than the maximum spatial discretization or the near zone size ($\gamma\Delta$). This results in a large number of immediate interactions (matrix entries of $\tilde{\mathbf{Z}}_0^{\mathrm{EM},h,h}$) for source-observer pairs outside the near zone. So $\tilde{\mathbf{Z}}_0^{\mathrm{EM},h,h}$ is also pre-corrected and stored in this scheme similar to [52], [77].

Next, the computational cost of the FE-AIM method is analyzed. In the first step of the FE-AIM scheme, the vector $\tilde{\mathbf{b}}_l$ is computed using 4D FFTs; this requires $O(N_{\mathrm{H}}(N_{\mathrm{C}}\log N_{\mathrm{C}} + N_{\mathrm{C}}\log^2 N_{\mathrm{g}} + N_{\mathrm{CKT}}))$ operations per time step In the second step, the Newton iterations are started and the residual is computed. The computation of linear and nonlinear contributions to requires $\tilde{\mathbf{F}}$ uses 3D FFTs and require $O(N_{\mathrm{H}}(N_{\mathrm{C}}\log N_{\mathrm{C}} + N_{\mathrm{CKT}}))$ and $O(N_{\mathrm{CKT}}^{\mathrm{nl}}N_{\mathrm{H}}^2)$ operations, respectively. Thus, a total of $O(\bar{N}_{\mathrm{N}}N_{\mathrm{H}}(N_{\mathrm{C}}\log N_{\mathrm{C}} + N_{\mathrm{CKT}} + N_{\mathrm{H}}N_{\mathrm{CKT}}^{\mathrm{nl}}))$ operations per time step are required to compute the residual at each time step. In the fourth step, the Jacobian matrices are filled; this requires $O(\bar{N}_{\mathrm{N}}N_{\mathrm{H}}^2N_{\mathrm{CKT}}^{\mathrm{nl}})$ operations per time step In the last step, the linear solve again uses 3D FFTs and hence requires $O(\bar{N}_{\mathrm{N}}\bar{N}_{\mathrm{I}}N_{\mathrm{H}}(N_{\mathrm{C}}\log N_{\mathrm{C}} + N_{\mathrm{CKT}} + N_{\mathrm{H}}N_{\mathrm{CKT}}^{\mathrm{nl}}))$ operations per time step; here, $\bar{N}_{\mathrm{I}}$ is the average number of iterations needed to solve the linear equation per Newton iteration per time step. Thus, the marching time scales as $O(N_{\mathrm{T}}[N_{\mathrm{H}}N_{\mathrm{C}}\log N_{\mathrm{C}} + N_{\mathrm{H}}N_{\mathrm{C}}\log^2 N_{\mathrm{g}} + \bar{N}_{\mathrm{N}}\bar{N}_{\mathrm{I}}N_{\mathrm{H}}N_{\mathrm{C}}\log N_{\mathrm{C}} + \bar{N}_{\mathrm{N}}N_{\mathrm{H}}^2N_{\mathrm{CKT}}^{\mathrm{nl}} + \bar{N}_{\mathrm{N}}\bar{N}_{\mathrm{I}}N_{\mathrm{H}}N_{\mathrm{CKT}}])$. For narrowband problems, the marching cost is dominated by the solve step and the marching time scales as $O(\bar{N}_{\mathrm{N}}\bar{N}_{\mathrm{I}}N_{\mathrm{H}}N_{\mathrm{C}}\log N_{\mathrm{C}} + \bar{N}_{\mathrm{N}}\bar{N}_{\mathrm{I}}N_{\mathrm{H}}N_{\mathrm{CKT}}])$. The antennas and microwave circuits are typically planar structures. For quasi planar structures, $N_{\mathrm{C}} \approx N_{\mathrm{EM}}$ and therefore the marching time scales as

$O(\bar{N}_{\mathrm{N}}\bar{N}_{\mathrm{I}}N_{\mathrm{H}}N_{\mathrm{EM}}\log N_{\mathrm{EM}} + \bar{N}_{\mathrm{N}}\bar{N}_{\mathrm{I}}N_{\mathrm{H}}N_{\mathrm{CKT}}])$ instead of $O(\bar{N}_{\mathrm{N}}\bar{N}_{\mathrm{I}}N_{\mathrm{H}}N_{\mathrm{EM}}^2 + \bar{N}_{\mathrm{N}}\bar{N}_{\mathrm{I}}N_{\mathrm{H}}N_{\mathrm{CKT}}])$ for the FE-MOT method described in the previous section. Comparison of the marching cost to TD-AIM is not straightforward as is the case of wires. It is done empirically for the problem in Section 5.4. The algorithm require $O(N_{\mathrm{H}}N_{\mathrm{g}}(N_{\mathrm{C}} + N_{\mathrm{EM}}) + N_{\mathrm{H}}^2 N_{\mathrm{CKT}})$ bytes to store and matrices and vectors used in the algorithm and $O(N_{\mathrm{H}}(N_{\mathrm{C}} + N_{\mathrm{EM}}) + N_{\mathrm{H}}N_{\mathrm{CKT}})$ operations to fill them. Compared to FE-MOT, the memory and matrix fill cost is significantly reduced. TD-AIM simulators [25] requires $O(N_{\mathrm{g}}^{\mathrm{TD}}(N_{\mathrm{C}} + N_{\mathrm{EM}}) + N_{\mathrm{H}}^2 N_{\mathrm{CKT}})$ bytes to store the matrices and vectors and $O(N_{\mathrm{C}} + N_{\mathrm{EM}}) + N_{\mathrm{CKT}})$ operations to compute them. The memory requirement for FE-AIM is smaller by $\sim N_{\mathrm{g}}^{\mathrm{TD}} / l_{\max}N_{\mathrm{H}}$ where $l_{\max}$ is the length of the temporal basis function and requires $\sim N_{\mathrm{H}}$ more computations to fill them.

5.3 SPARSE NEAR-FIELD PRECONDITIONERS

In order to accelerate the convergence of the linearized equation at each Newton iteration, the performance of two preconditioners viz. iterative near-field [57] and sparse approximate inverse [56] are compared here. Here, for notational simplicity, (3.16) is denoted as

$$\tilde{\tilde{\mathbf{J}}}_{l,p}^{\mathrm{R}}\tilde{\tilde{s}}_p = \tilde{\tilde{\mathbf{r}}}_{l,p-1} \tag{5.16}$$

5.3.1 Iterative Near-Field Preconditioner

The iterative near field (INF) preconditioner is an implicit right-preconditioner, i.e. inverse of preconditioner is not pre-computed and an inner iterative solve (not very accurate) is used instead in the iterative solution procedure. Here, at each Newton iteration $p = 1,2,\ldots$, a matrix $\mathbf{M}_p$ is formed by using the three components: (i) Choosing

EM entries using proximity filtering and algebraic filtering [55]. Proximity filtering chooses those EM entries for which the source and observer basis functions are separated by less than a predefined distance and algebraic filtering removes the entries with less than a predefined value. (ii) Neglecting the non-block-diagonal entries of the Jacobian sub-matrices arising in the CKT system. Note that the preconditioner matrix changes at every Newton iteration as the "linear" (block-diagonal) components of the Jacobian are included. (iii) Including all EM-CKT coupling terms. The preconditioning matrix is an operator which approximates $\mathbf{M}_p^{-1}$ using an iterative solver. In order to solve (3.16), this preconditioner solves $\tilde{\tilde{\mathbf{J}}}_{l,p}^{\mathrm{R}}\mathbf{M}_p^{-1}s_p' = \tilde{\tilde{\mathbf{r}}}_{l,p-1}$ for s_p' iteratively and then computes $\tilde{\tilde{s}}_p$ by solving $\tilde{\tilde{s}}_p = \mathbf{M}_p s_p'$. The iteration solution procedure to find $\tilde{\tilde{s}}_p$ can be cast in three phases as follows (Fig. 5.2) :

Phase I – Inner solve: At each solver iteration $i = 1,2,\ldots$, Solve (inaccurately) $\mathbf{M}_p\mathbf{s}_i'' \approx \mathbf{s}_i'$ starting from $\mathbf{s}_1' = \mathbf{0}$. The matrix $\mathbf{M}_p$ is block-diagonal and hence each of the N_{H} blocks can be solved independently.

Phase II – Outer solve: Next, compute $\mathbf{r}_i'' = \tilde{\tilde{\mathbf{r}}}_{l,p-1} - \tilde{\tilde{\mathbf{J}}}_{l,p}^{\mathrm{R}}s_i''$. If $\left\|\mathbf{r}_i''\right\| \le tol_{\mathrm{iter}}.\left\|\tilde{\tilde{\mathbf{r}}}_{l,p-1}\right\|$, then, proceed to Phase III for post-computing step. Here, tol_{iter} is a pre-defined tolerance for determining convergence of the linear iterative solver. Else, update $\mathbf{s}_{i+1}'$ using $\mathbf{r}_i''$ and $\mathbf{s}_i'$ according to a Krylov sub-space iterative solver algorithm. Here, generalized minimal residual method (GMRES) is used to update the guess $\mathbf{s}_i'$. Proceed to phase I again with $i = i + 1$.

Phase III –Post Computing: Find $\tilde{\tilde{\mathbf{s}}}_p$ by solving $\mathbf{M}_p\tilde{\tilde{\mathbf{s}}}_p = \mathbf{s}_i'$.

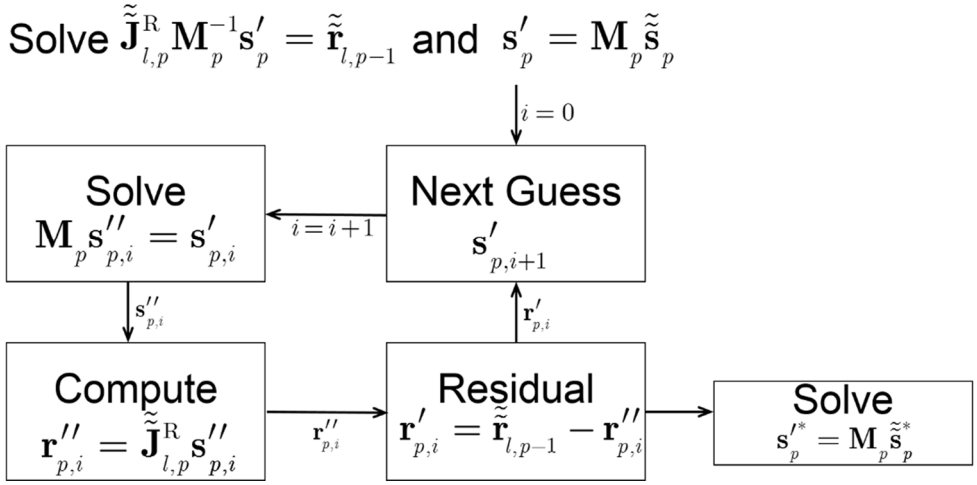

Fig. 5.2. Iterative near field preconditioner [57], [55].

5.3.2 Sparse Approximate Inverse Preconditioner (SAI)

Sparse approximate inverse (SAI) is an explicit preconditioner i.e., the inverse of preconditioner is precomputed [56]. A matrix is formed by using the three components: (i) Choosing EM entries, as in INF, using proximity filtering and algebraic filtering. (ii) Neglecting the nonlinear elements contribution in the arising in the CKT system. (iii) Including all EM-CKT coupling terms. The preconditioning matrix (denoted by $\mathbf{M}$) is an approximate inverse of the above defined matrix and is precomputed. The matrix $\mathbf{M}$ is found and made sparse by algebraic and proximity filtering of the inverted matrix. Again as in INF, the solution procedure can be cast in three phases : (Fig. 5.3)

Phase I – Inner solve: At each solver iteration $i = 1, 2, \ldots$, Compute $\mathbf{s}''_i \approx \mathbf{M}\mathbf{s}'_i$ starting from $\mathbf{s}'_1 = \mathbf{0}$. The matrix $\mathbf{M}$ is block-diagonal and hence each of the N_{H} blocks can be multiplied independently.

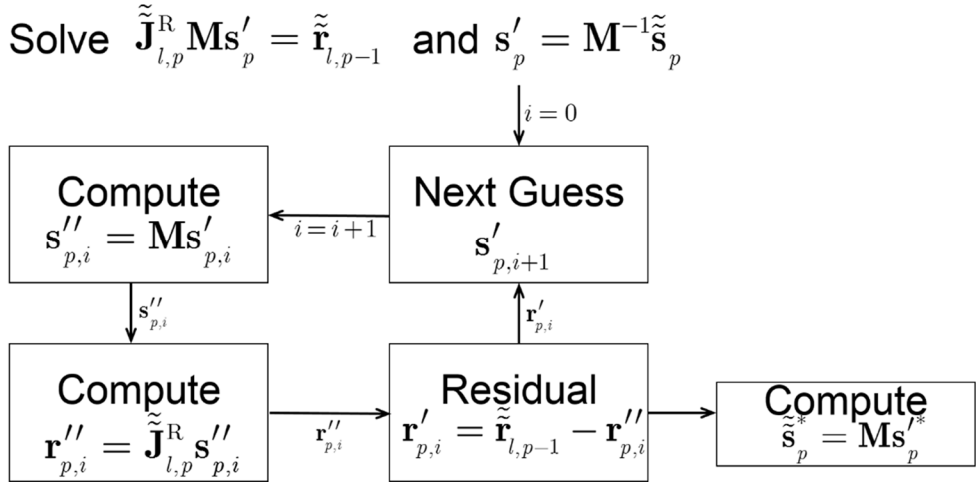

Fig. 5.3. Sparse approximate inverse preconditioner [56], [55].

Phase II – Outer solve: Next, compute $\mathbf{r}''_i = \tilde{\tilde{\mathbf{r}}}_{l,p-1} - \tilde{\tilde{\mathbf{J}}}^{\mathrm{R}}_{l,p} s''_i$. If $\left\|\mathbf{r}''_i\right\| \le tol_{\mathrm{iter}} . \left\|\tilde{\tilde{\mathbf{r}}}_{l,p-1}\right\|$, then, proceed to Phase III for post-computing step. Here, tol_{iter} is a pre-defined tolerance for determining convergence of the linear iterative solver. Else, update $\mathbf{s}'_{i+1}$ using $\mathbf{r}''_i$ and $\mathbf{s}'_i$ according to a Krylov sub-space iterative solver algorithm. Here, generalized minimal residual method (GMRES) is used to update the guess $\mathbf{s}'_i$. Proceed to phase I again with $i = i + 1$.

Phase III –Post Computing: Find $\tilde{\tilde{\mathbf{s}}}_p$ by computing $\tilde{\tilde{\mathbf{s}}}_p = \mathbf{M}\mathbf{s}'_i$

Although, both the preconditioners has more computations per iterations than applying an iterative solver to (3.16), the number of iterations ($\bar{N}_{\mathrm{I}}$) is greatly reduced and the overall solve time is reduced. There is also an increase in filling the matrices and the memory used. This improvement is demonstrated in an example in Section 5.4

5.4 NUMERICAL EXAMPLES

First, an unbalanced microstrip mixer [79] is analyzed to validate the FE-AIM method Here, a Schottky barrier diode connected with an open stub filter is used an unbalanced microstrip mixer (Fig.5.4(a) and Fig. 5.4(b)). The Schottky barrier diode

model is shown in Fig. 5.4(c). The mixer is excited by a voltage source with a series resistance $R = 50\ \Omega$. The output port is also loaded with a $50\ \Omega$ resistance. The excitation voltage is a modulated sinusoidal wave given by

$$V_{\text{in}}(t) = 0.3 f(t) \sin(\omega_{\text{mod}} t) \sin((\omega_0 + \omega_{\text{mod}})t) \tag{5.17}$$

Here, $f(t)$ is the slowly ramping up pulse function as in (3.17), $\omega_0 / 2\pi = 2$ GHz and $\omega_{\text{mod}} / 2\pi = 25$ MHz .The mixer combines the two frequencies and the difference of the two frequencies is output. In the following, the ground plane, mixer circuit and dielectric substrate were meshed such that there are $N_{\text{S}} = 376$ surface unknowns, $N_{\text{gap}} = 9$ port unknowns and $N_{\text{V}} = 3384$ volume unknowns, there are 3 circuits with $N_{\text{CKT}} = 8$. The resulting diode voltage and output voltage are found using $N_{\text{H}} = 4$ and $\Delta t = 20\pi / \omega_0 = 5$ ns ; the result is compared to a TD-AIM solver with a step size of $\pi / 20\omega_0 = 0.125$ ns in Figs. 5.4(d)-5.4(g). The results agree well both during ramp up and steady state. The simulator also captures the demodulating scheme where the output voltage is dominated by the ω_{mod} frequency component.

Next, the performance of the FE-AIM method is compared by plotting the errors incurred by the methods as a function of their computational costs. In these plots, the error is defined as L-2 norm error in the current in the diode (3.18) with $N_{\text{T}} \Delta t = 0.25\ \mu$s . The reference is computed from a more-accurate FE-AIM simulation with $N_{\text{H}} = 6$ and $\Delta t = \pi / \omega_0 = 0.5$ ns. The error is plotted versus the marching time, matrix fill time and the memory respectively in Figs. 5.5(a)-5.5(c) for both time-domain and Fourier envelope methods.. Again, the results show that the Fourier envelope method has more accurate solution with a much smaller marching time and comparable memory.

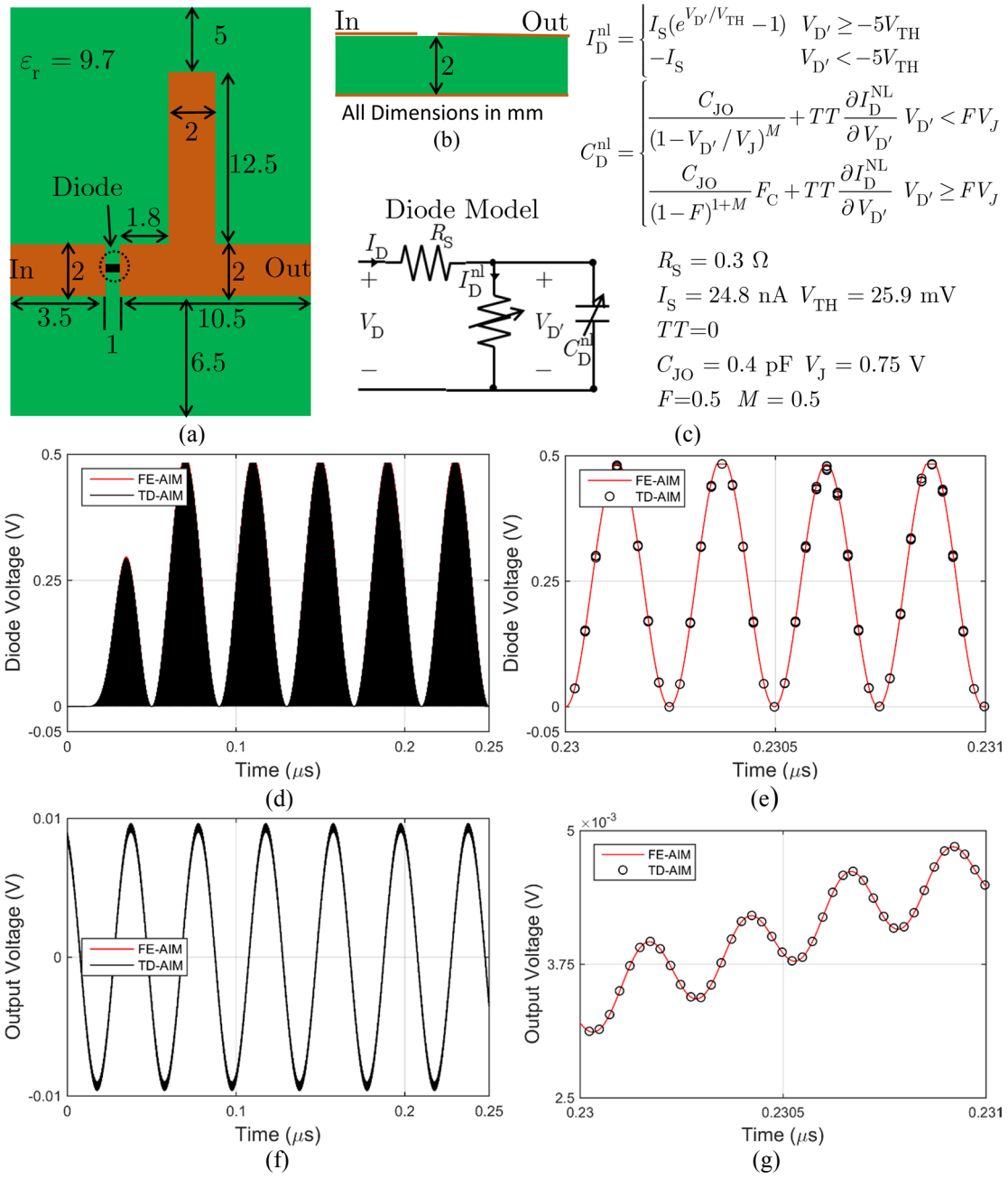

Fig. 5.4. Unbalanced Microstrip Mixer. (a) Top view. (b) Cross Section view. (c) Diode Model. (d) Diode voltage. (e) Steady state diode voltage. (f) Output Voltage. (g) Steady state output voltage.

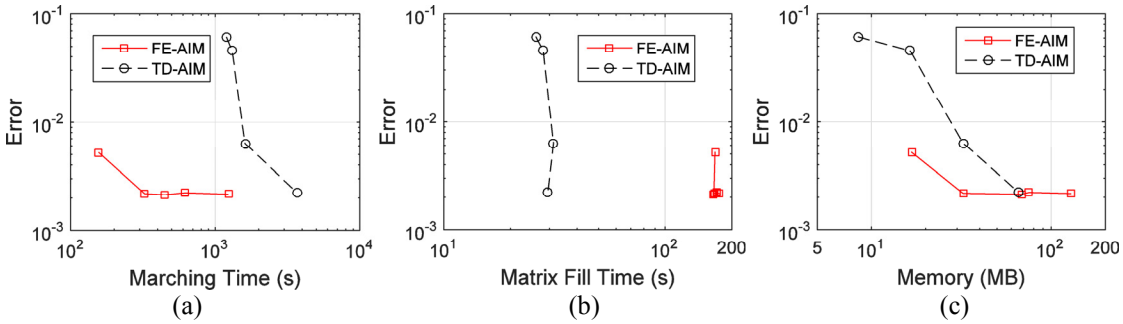

Fig. 5.5. Cost Analysis of mixer simulation. (a) Error versus marching time. (b) Error versus matrix fill time. (c) Error vs memory.

However, the matrix fill time (which is small comparable to the marching time is greater than the time-domain one.

In the second example, a rectenna array is analyzed to show the applicability of the preconditioners and validate the cost. The feed structure, the rectenna array and one element of the rectenna array consisting of printed dipoles center loaded with p-n junction diodes are shown. The models of the diode are same as those described in Section 3.2. The dipole is assumed to be made of PEC and residing in air. The structure is excited by a slowly rising sinusoidal pulse plane wave (3.17) with $\omega_0 / 2\pi = 5.8\,\mathrm{GHz}$ and $\tau_0 = 500\pi / \omega_0$. The array consisted of 3×2 elements. In these analysis, for all preconditioners, the structure was discretized using 770 elements ($N_{\mathrm{EM}} = 770$), the envelope tracking parameters were $\Delta t = 1\,\mathrm{ns}$ and $N_{\mathrm{H}} = 3$. The AIM near zone parameters were $\Delta = 2.586\,\mathrm{mm}$ and $\gamma = 3$. The output induced voltage and the currents are plotted in Figs. 5.6(c) and 5.6(d) using a diagonal preconditioner, INF preconditioner and SAI preconditioner. It shows the three results agree with each other very well.

Next, in order to quantify the improvements using the sparse near-field preconditioners, the number of array elements is varied. The number of elements used are $1 \times 1, 3 \times 2, 3 \times 7, 3 \times 20, 3 \times 60, 3 \times 80$. Figs. 5.6(e) and 5.6(f) plot the time needed to fill

the matrices and the marching time respectively as the number of surface unknowns. Results from diagonal precondition, direct inversion (full inverse) , INF and SAI preconditioners are compared here. From Fig. 5.6(e), the precomputing of the direct solve adds significant cost which becomes prohibitive after 2700 unknowns. SAI preconditioner which precomputes some components of the inverse has an increased fill cost (~1.5-2 times) compared to diagonal and INF preconditioners. It can be seen from Fig. 5.6. (f) that INF (SAI) preconditioning roughly 3.5 (5) times faster than diagonal preconditioning for rectenna arrays. It can be inferred that INF should be used for applications requiring early time effects and SAI preconditioners for applications requiring steady state and late time effects.

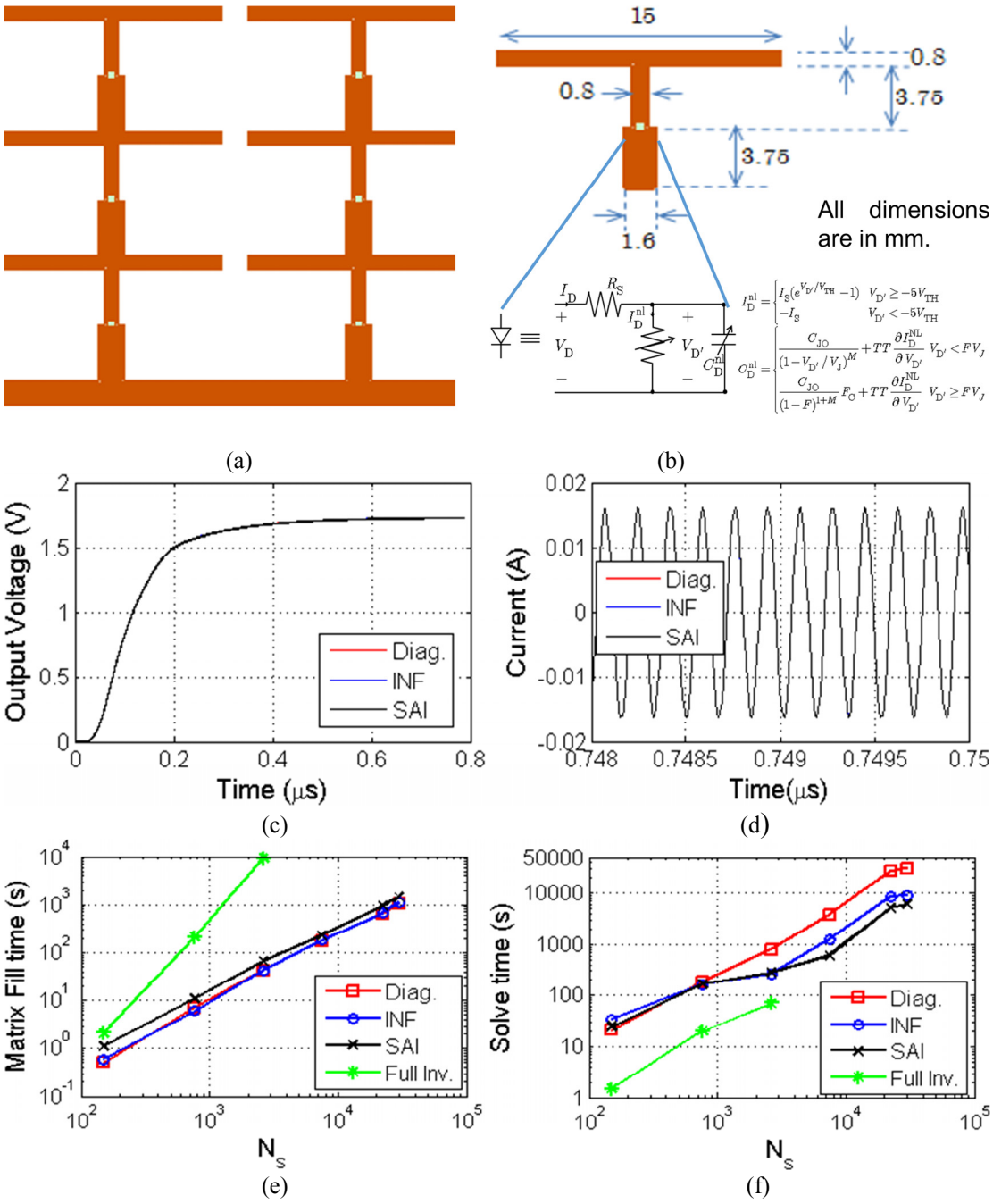

Fig. 5.6. Rectenna Array (a) & (b) A 6-element rectenna array. (c) Output voltage. (c) Output current. (e) & (f) Matrix and Solve time as the number of elements are increased

CHAPTER 6

HYBRID EM-CKT SIMULATORS FOR TRANSIENT ANALYSIS OF NONLINEARLY LOADED PERIODIC STRUCTURES

Large nonlinearly loaded arrays are encountered in applications like frequency selective surfaces, phased array antennas [6], [7], [70] for either achieving frequency tunability or increasing the bandwidth of the structure. An efficient method for analyzing these arrays is to model them as infinitely periodic arrays of a (significantly smaller) reference structure. The signals (fields, voltages, currents etc.) are assumed to be such that these quantities at all locations are expressed as time-shifted of the corresponding signals in the reference structure The governing equations are enforced in terms of the signals in the reference structures. In this chapter, both TD and FE hybrid EM-CKT simulators are presented for analyzing transient scattering from such nonlinearly loaded periodic structures

The problem statement is presented in Section 6.1. The TD-MOT formulation.is described in Section 6.2. The FE-MOT formulation is presented in Section 6.3. The numerical results for solving frequency selected surfaces loaded with varactor diodes is presented in Section 6.4.

6.1 PROBLEM STATEMENT

Consider a two-dimensional periodic (in the x-y directions) arrangement of arbitrarily shaped dielectric and PEC bodies that are loaded with nonlinear time-invariant devices at various locations (unit cells) (Fig. 6.1(a)). Let the size of the unit cell along x and y directions be denoted as d_{x} and d_{y} respectively. The structure is assumed to reside in an unbounded homogeneous medium with permittivity ε and permeability μ. The structure is excited by a plane wave with the direction of propagation $\hat{k}_{\mathrm{inc}}$ and electric

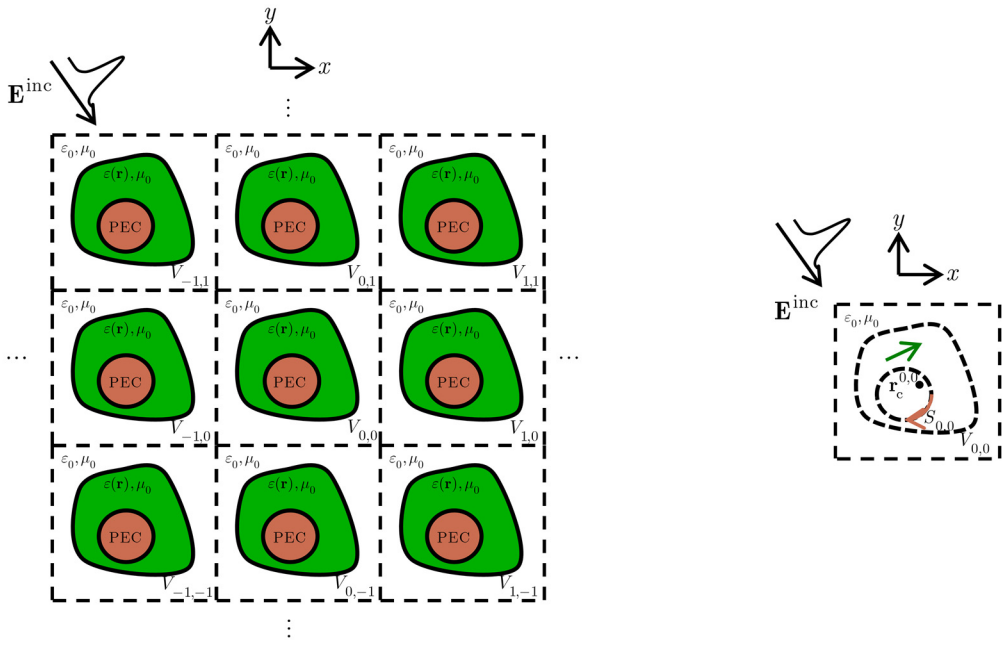

Fig. 6.1. Periodic structure problem description. (a) Two dimensional periodic structure composed of dielectric and PEC bodies. (b) the equivalent problem with periodic Green function.

field $\mathbf{E}^{\text{inc}}(\mathbf{r},t)$ produced due to an external impressed source. The impressed sources are assumed to be essentially bandlimited to the angular frequency band $[\omega_0-\omega_{\text{bw}},\omega_0+\omega_{\text{bw}}]$, where ω_0 is the fundamental carrier frequency and ω_{bw} is the single-sided bandwidth. One of the unit cells is identified as the "reference cell" such that the incident electric field and the induced currents in this cell are zero for $t\le 0$.

6.2 TIME DOMAIN HYBRID EM-CKT FORMULATION

An EM time-domain simulator for transient analysis of the scattering from periodic array of PEC structures was developed and presented in [58]. Here, a similar formulation is used for periodic arrays of PEC and dielectric structures loaded with lumped circuits.

6.2.1 EM System of Equations

The signals (fields, currents) in any cell can be shown to be a time-shifted copy of those in the reference cell, i.e., for $m,n \in (-\infty,\ldots,-1,0,1,\ldots,\infty)$ [58]

$$\begin{aligned}
\mathbf{E}^{m,n}(\mathbf{r},t) &= \mathbf{E}^{0,0}(\mathbf{r}-\mathbf{r}_{\mathrm{c}}^{m,n}, t-\hat{\mathbf{k}}^{\mathrm{inc}}\bullet\mathbf{r}_{\mathrm{c}}^{m,n}\ /\ c)\\
\mathbf{E}^{\mathrm{inc},m,n}(\mathbf{r},t) &= \mathbf{E}^{\mathrm{inc},0,0}(\mathbf{r}-\mathbf{r}_{\mathrm{c}}^{m,n}, t-\hat{\mathbf{k}}^{\mathrm{inc}}\bullet\mathbf{r}_{\mathrm{c}}^{m,n}\ /\ c)\\
\mathbf{J}_{\mathrm{S}}^{m,n}(\mathbf{r},t) &= \mathbf{J}_{\mathrm{S}}^{0,0}(\mathbf{r}-\mathbf{r}_{\mathrm{c}}^{m,n}, t-\hat{\mathbf{k}}^{\mathrm{inc}}\bullet\mathbf{r}_{\mathrm{c}}^{m,n}\ /\ c)\\
\mathbf{J}_{\mathrm{V}}^{m,n}(\mathbf{r},t) &= \mathbf{J}_{\mathrm{V}}^{0,0}(\mathbf{r}-\mathbf{r}_{\mathrm{c}}^{m,n}, t-\hat{\mathbf{k}}^{\mathrm{inc}}\bullet\mathbf{r}_{\mathrm{c}}^{m,n}\ /\ c)
\end{aligned} \tag{6.1}$$

Here, m,n are indices of the cells along the *x* and *y* directions respectively and each unit cell is indicated by (m,n). The reference cell is assumed to be the unit cell (0,0), $c=(\mu\varepsilon)^{-1/2}$ is the speed of light in the background medium, $\hat{\mathbf{k}}^{\mathrm{inc}}$ is the unit vector along the propagation direction of the incident plane wave, $\mathbf{r}_{\mathrm{c}}^{m,n}$ is the center of the unit cell, $\mathbf{E}^{m,n}, \mathbf{E}^{\mathrm{inc},m,n}, \mathbf{J}_{\mathrm{S}}^{m,n}$ and $\mathbf{J}_{\mathrm{V}}^{m,n}(\mathbf{r},t)$ represent the total electric-field, incident electric field, induced surface current on PEC and the polarization current in the dielectrics in the unit cell (m,n) respectively. Note that $\hat{\mathbf{k}}^{\mathrm{inc}}\bullet\mathbf{r}_{\mathrm{c}}^{m,n}=0$ for normal incidence and the excitations for all unit cells are identical. Thus, (6.1) can be used to express the scattering problem can be modified to that of relating the fields in the reference cell to the surface/volume currents in the reference cell radiating through a periodic Green function (Fig. 6.1(b)) [58].

To model the field interactions with the EM structure, boundary and consistency conditions are enforced on the reference cell: On the PEC surface $S_{0,0}$, the time derivative of the electrical field tangential to is forced to be zero; on the dielectric volume $V_{0,0}$, the time derivative of the total electric field is enforced to be equal to the time derivatives of sum of incident and scattered fields [25], [58]

$$
\begin{aligned}
\hat{n}\times\hat{n}\times\partial_t\mathbf{E}^{\mathrm{inc},0,0}(\mathbf{r},t) &= \hat{n}\times\hat{n}\times[\nabla\partial_t\phi_{\mathrm{S}}^{0,0}(\mathbf{r},t)+\partial_t^2\mathbf{A}_{\mathrm{S}}^{0,0}(\mathbf{r},t)]+ \\
&\qquad \hat{n}\times\hat{n}\times[\nabla\partial_t\phi_{\mathrm{V}}^{0,0}(\mathbf{r},t)+\partial_t^2\mathbf{A}_{\mathrm{V}}^{0,0}(\mathbf{r},t)] \qquad \mathbf{r}\in S_{0,0} \\
\partial_t\mathbf{E}^{\mathrm{inc},0,0}(\mathbf{r},t) &= \partial_t\mathbf{E}(\mathbf{r},t)+[\nabla\partial_t\phi_{\mathrm{V}}^{0,0}(\mathbf{r},t)+\partial_t^2\mathbf{A}_{\mathrm{V}}^{0,0}(\mathbf{r},t)] \\
&\qquad +[\nabla\partial_t\phi_{\mathrm{S}}^{0,0}(\mathbf{r},t)+\partial_t^2\mathbf{A}_{\mathrm{S}}^{0,0}(\mathbf{r},t)] \qquad \mathbf{r}\in V_{0,0}
\end{aligned}
\tag{6.2}
$$

Here, ∂_t denotes the partial time derivative, $\{\phi_{\mathrm{S}}^{0,0},\mathbf{A}_{\mathrm{S}}^{0,0}\}$ ($\{\phi_{\mathrm{V}}^{0,0},\mathbf{A}_{\mathrm{V}}^{0,0}\}$) denotes the {electric scalar, magnetic vector} potential due to the currents on the PEC surface (in the dielectric volume) *in all unit cells*, and $\hat{n}$ is the outward pointing unit vector normal to $S_{0,0}$. In (6.2), the vector and scalar potentials due to the currents in all unit cells can be expressed as the potentials scattered by the currents in the reference cells convolved with a periodic Green function i.e.

$$
\begin{aligned}
\partial_t\phi_{\mathrm{S}}^{0,0}(\mathbf{r},t) &= -\frac{1}{\varepsilon}\iint_{S_{0,0}}[\nabla'\bullet\mathbf{J}_{\mathrm{S}}^{0,0}(\mathbf{r}',t)*G^{\mathrm{per}}(\mathbf{r},\mathbf{r}',t)]ds' \\
\mathbf{A}_{\mathrm{S}}^{0,0}(\mathbf{r},t) &= \mu\iint_{S_{0,0}}[\mathbf{J}_{\mathrm{S}}^{0,0}(\mathbf{r}',t)*G^{\mathrm{per}}(\mathbf{r},\mathbf{r}',t)]ds' \\
\partial_t\phi_{\mathrm{V}}^{0,0}(\mathbf{r},t) &= -\frac{1}{\varepsilon}\iiint_{V_{0,0}}[\nabla'\bullet\mathbf{J}_{\mathrm{V}}^{0,0}(\mathbf{r}',t)*G^{\mathrm{per}}(\mathbf{r},\mathbf{r}',t)]dv' \\
\mathbf{A}_{\mathrm{V}}^{0,0}(\mathbf{r},t) &= \mu\iiint_{V_{0,0}}[\mathbf{J}_{\mathrm{V}}^{0,0}(\mathbf{r}',t)*G^{\mathrm{per}}(\mathbf{r},\mathbf{r}',t)]dv'
\end{aligned}
\tag{6.3}
$$

The periodic Green function is given as

$$
G^{\mathrm{per}}(\mathbf{r},\mathbf{r}',t)=\sum_m\sum_n\frac{\delta(t-(\hat{\mathbf{k}}^{\mathrm{inc}}\bullet\mathbf{r}_{\mathrm{c}}^{m,n}+R^{m,n})/c)}{4\pi R^{m,n}} \tag{6.4}
$$

Here, $R^{m,n}=\mid\mathbf{r}-\mathbf{r}'-\mathbf{r}_{\mathrm{c}}^{m,n}\mid$ is the distance between a source point in the (m,n) unit cell and the observer point in the reference cell. The periodic Green function can be interpreted as the magnetic vector potential produced at an observer point in the reference cell at time t due to corresponding point current sources in all unit cells. For obliquely incident plane wave, there will be unit cells such that $\hat{\mathbf{k}}^{\mathrm{inc}}\bullet\mathbf{r}_{\mathrm{c}}^{m,n}+R^{m,n}<0$. This results

in a non-causal Green function i.e. the potentials and the fields in the reference cell at time $t = t_0$ depends on the currents in the reference cell at times $t > t_0$ [58], [80], [81]. Indeed, special temporal basis and testing function [58], [82] have to be used along with extrapolation schemes [58], [59] to develop a time-marching solution scheme.as explained next.

To solve (6.2) numerically, the surface and volume in the reference cell are discretized using triangular and tetrahedral elements in the same manner as described in Section 5.1.1. Next, the current densities are approximated using $N_{\mathrm{T}}^{\mathrm{TD}} N_{\mathrm{EM}}$ ($N_{\mathrm{EM}} = N_{\mathrm{S}} + N_{\mathrm{gap}} + N_{\mathrm{V}}$) temporal-spatial functions, i.e.

$$\begin{aligned}
\mathbf{J}_{\mathrm{S}}^{0,0}(\mathbf{r},t) &\cong \sum_{l'=1}^{N_{\mathrm{T}}^{\mathrm{TD}}} \sum_{k'=1}^{N_{\mathrm{S}}} \mathbf{I}_{l'}^{\mathrm{EM}}[k']\mathbf{S}_{k'}(\mathbf{r}) T_{l'}(t - \hat{\mathbf{k}}^{\mathrm{inc}} \bullet \mathbf{r}_{k'} \,/\, c) \\
&\quad + \sum_{l'=1}^{N_{\mathrm{T}}^{\mathrm{TD}}} \sum_{k'=1}^{N_{\mathrm{gap}}} \mathbf{I}_{l'}^{\mathrm{EM}}[N_{\mathrm{S}} + k']\mathbf{P}_{k'}(\mathbf{r}) T_{l'}(t - \hat{\mathbf{k}}^{\mathrm{inc}} \bullet \mathbf{r}_{N_{\mathrm{S}}+k'} \,/\, c) \qquad (6.5) \\
\mathbf{J}_{\mathrm{V}}^{0.0}(\mathbf{r},t) &\cong \sum_{l'=1}^{N_{\mathrm{T}}^{\mathrm{TD}}} \sum_{k'=1}^{N_{\mathrm{V}}} \kappa(\mathbf{r}) \mathbf{I}_{l'}^{\mathrm{EM}}[N_{\mathrm{S}} + N_{\mathrm{gap}} + k']\mathbf{V}_{k'}(\mathbf{r}) \partial_t T_{l'}(t - \hat{\mathbf{k}}^{\mathrm{inc}} \bullet \mathbf{r}_{N_{\mathrm{S}}+N_{\mathrm{gap}}+k'} \,/\, c)
\end{aligned}$$

Here, $\mathbf{I}_{l'}^{\mathrm{EM}}$ is an $N_{\mathrm{EM}} \times 1$ vector that stores unknown coefficients, $\mathbf{S}_{k'}, \mathbf{P}_{k'}, \mathbf{V}_{k'}$ are the spatial basis functions which are RWG [71], port basis functions (Section 5.1.3) and SWG [72] basis functions, respectively, $\mathbf{r}_{k'}$ is the center of the basis function $\mathbf{S}_{k'}$, $\mathbf{P}_{k'}$ or $\mathbf{V}_{k'}$. In (6.5), $T_{l'}(t) = T(t - l'\Delta t^{\mathrm{TD}})$ are the temporal basis functions and Δt^{TD} is the time step size for the time domain simulator. In order to facilitate the extrapolation required, the temporal basis functions are chosen as bandlimited interpolatory functions [59], [67]. Substituting (6.5) in (6.4) and testing the resulting equations with $\mathbf{S}_k(\mathbf{r})\delta(t - \hat{\mathbf{k}}^{\mathrm{inc}} \bullet \mathbf{r}_k \,/\, c)$, $\mathbf{P}_k(\mathbf{r})\delta(t - \hat{\mathbf{k}}^{\mathrm{inc}} \bullet \mathbf{r}_{N_{\mathrm{S}}+k} \,/\, c)$ for the surface EFIE and $\mathbf{V}_k(\mathbf{r})\delta(t - \hat{\mathbf{k}}^{\mathrm{inc}} \bullet \mathbf{r}_{N_{\mathrm{S}}+N_{\mathrm{gap}}+k} \,/\, c)$ for the volume EFIE results in the equation

$$\sum_{l'=-N_{\text{adv}}}^{0} \mathbf{Z}_{l-l'}^{0,0}\mathbf{I}_{l'}^{\text{EM}} = \mathbf{V}_{l}^{\text{EM}} - \sum_{l'=1}^{l-1} \mathbf{Z}_{l-l'}^{0,0}\mathbf{I}_{l'}^{\text{EM}} \quad \text{for } l = 1,\ldots,N_{\text{T}}^{\text{TD}} \tag{6.6}$$

Unlike the free-space time-domain simulators [24], [25], the temporal basis functions are delayed based on their location in the unit cell. So $\tilde{\mathbf{I}}_{l'}^{\text{EM},h}$ does not hold the current samples at $l'\Delta t$ but different times for different basis functions. It contains the sample of each basis function k' is sampled at time $l'\Delta t^{\text{TD}} + \hat{\mathbf{k}}^{\text{inc}} \bullet \mathbf{r}_{k'} / c$ Also, the testing procedure enforces the EFIE at different times at different positions in the reference cell. In general, this is a causality trick used to reduce the number of current samples that need to be extrapolated [58], [82] from $\max(0, \left\lfloor \left|\mathbf{r} - \mathbf{r}'\right| / c\Delta t^{\text{TD}} \right\rfloor)$ $\forall \mathbf{r}', \mathbf{r} \in \{S_{0,0} \cup V_{0,0}\}$ (if free space temporal basis-testing functions in Section 5.1.1 were used) to

$$N_{\text{adv}} = \max \left\{ \begin{array}{l} 0 \\ \max\limits_{\mathbf{r}\in \text{span}(\mathbf{S}_{k'})} \left\lfloor \left|\mathbf{r} - \mathbf{r}_{k'}\right| / c\Delta t^{\text{TD}} \right\rfloor \\ \max\limits_{\mathbf{r}\in \text{span}(\mathbf{P}_{k'})} \left\lfloor \left|\mathbf{r} - \mathbf{r}_{N_{\text{S}}+k'}\right| / c\Delta t^{\text{TD}} \right\rfloor \\ \max\limits_{\mathbf{r}\in \text{span}(\mathbf{V}_{k'})} \left\lfloor \left|\mathbf{r} - \mathbf{r}_{N_{\text{S}}+N_{\text{gap}}+k'}\right| / c\Delta t^{\text{TD}} \right\rfloor \end{array} \right\} \tag{6.7}$$

For typical problems, the size of the unit cells are comparable to the wavelength of interest and the meshes are approximately tenth or twentieth of the minimum wavelength of interest. The above procedure results in $N_{\text{adv}} \sim 2-3$ while $N_{\text{adv}} \sim 15-20$ if the temporal basis-testing functions in Section 5.1.1 were used. For the sake of simplicity in coupling EM and CKT equations, all the port basis functions defined at one device are sampled using the same temporal basis function and tested at the same time. For e.g., if the port basis functions $\mathbf{P}_1, \mathbf{P}_2, \mathbf{P}_3$ are connected to the device *D*, then $\mathbf{r}_{N_{\text{S}}+1} = \mathbf{r}_{N_{\text{S}}+2} = \mathbf{r}_{N_{\text{S}}+3} \doteq \mathbf{r}_D$. The advanced samples are found using extrapolation similar to the methods described in [59], [67].

6.2.2 CKT System of Equations

The circuit quantities are also time-shifted copies of the those in the reference cell, i.e., for $m,n \in (-\infty,\ldots,-1,0,1,\ldots,\infty)$ [58]

$$\begin{aligned}\mathbf{V}^{m,n}(t) &= \mathbf{V}^{0,0}(t-\hat{\mathbf{k}}^{\mathrm{inc}}\bullet\mathbf{r}_{\mathrm{c}}^{m,n}\ /\ c)\\ \mathbf{I}^{\mathrm{nl},m,n}(t) &= \mathbf{I}^{\mathrm{nl},0,0}(t-\hat{\mathbf{k}}^{\mathrm{inc}}\bullet\mathbf{r}_{\mathrm{c}}^{m,n}\ /\ c)\\ \mathbf{I}^{m,n}(t) &= \mathbf{I}^{0,0}(t-\hat{\mathbf{k}}^{\mathrm{inc}}\bullet\mathbf{r}_{\mathrm{c}}^{m,n}\ /\ c)\end{aligned} \tag{6.8}$$

The CKT equations in different reference cells are coupled only through the EM equations and the CKT relationship for the circuit in the reference cell (and also other unit cells) can be expressed similar to those presented in [24], [25]: for $l = 1,\ldots.N_{\mathrm{T}}^{\mathrm{TD}}$

$$\mathbf{Y}^{\mathrm{CKT}}\mathbf{V}_l^{\mathrm{CKT}} + \mathbf{I}_l^{\mathrm{nl}}(\mathbf{V}_l^{\mathrm{CKT}}) = \mathbf{I}_l^{\mathrm{CKT}} \tag{6.9}$$

There is, however, one difference in these equations: Each of the N_{D} system of equations are enforced at times $l\Delta t - \hat{\mathbf{k}}^{\mathrm{inc}}\bullet\mathbf{r}_{1,\ldots,N_{\mathrm{D}}}$ because the EM and CKT equations at the ports must be enforced at the same time.

6.2.3 Coupling of EM-CKT equations and Nonlinear Solution Algorithm

The EM structure and devices in the reference cell are coupled using the port model presented in Section 5.1.3. For each device, the coupling from the device to the PEC surface is modeled by (i) enforcing the average line integral of the electric field in the gap to the port voltage, (ii) approximating the time-derivative of the port voltage with a third order backward difference formula and (iii) expanding the currents in terms of space-time basis functions (6.5). This results in the following system of equations

$$\mathbf{Z}_0^{\mathrm{port}}\mathbf{I}_l^{\mathrm{EM}} - \mathbf{C}_0^{\mathrm{V}}\mathbf{V}_l^{\mathrm{CKT}} = \mathbf{V}_l^{\mathrm{port}} - \sum_{l'=l-3}^{l-1}\mathbf{C}_{l-l'}^{\mathrm{V}}\mathbf{V}_{l'}^{\mathrm{CKT}} - \sum_{l'=1}^{l-1}\mathbf{Z}_{l-l'}^{\mathrm{port}}\mathbf{I}_{l'}^{\mathrm{EM}} \tag{6.10}$$

The coupling from the EM structure to the circuit port is identical to that described in [24], [25]. The final system of equations can be expressed as

$$\mathbf{F}(\mathbf{X}_l) = \mathbf{b}_l \quad \text{for } l = 1,\ldots,N_{\mathrm{T}}^{\mathrm{TD}} \tag{6.11}$$

where

$$\mathbf{F}(\mathbf{X}_l) = \begin{bmatrix} \mathbf{Z}_0^{\mathrm{EM}} + \mathbf{Z}_0^{\mathrm{port}} & \zeta_0\mathbf{C} \\ -\mathbf{C}^T & \mathbf{Y}^{\mathrm{CKT}} \end{bmatrix} \underbrace{\begin{bmatrix} \mathbf{I}_l^{\mathrm{EM}} \\ \mathbf{V}_l^{\mathrm{CKT}} \end{bmatrix}}_{\mathbf{x}_l} + \begin{bmatrix} 0 \\ \mathbf{I}_l^{\mathrm{nl}}(\mathbf{V}_l^{\mathrm{CKT}}) \end{bmatrix} \tag{6.12}$$

and

$$\mathbf{b}_l = \begin{bmatrix} \mathbf{V}_l^{\mathrm{EM}} + \mathbf{V}_l^{\mathrm{port}} - \sum_{l'=1}^{l-1} (\mathbf{Z}_{l-l'}^{\mathrm{EM}} + \mathbf{Z}_{l-l'}^{\mathrm{port}})\mathbf{I}_{l'}^{\mathrm{EM}} - \sum_{l'=l-3}^{l-1} \zeta_{l-l'}\mathbf{C}\tilde{\mathbf{V}}_{l'}^{\mathrm{CKT}} \\ \mathbf{I}_l^{\mathrm{CKT}} \end{bmatrix} \tag{6.13}$$

A multidimensional nonlinear solution algorithm identical to that described in [25] is used to solve (6.11). However, in the first step, when finding the right hand side a blocked Toeplitz FFT is used to accelerate the evaluation of $\sum_{l'=1}^{l-1} (\mathbf{Z}_{l-l'}^{\mathrm{EM}} + \mathbf{Z}_{l-l'}^{\mathrm{port}})\mathbf{I}_{l'}^{\mathrm{EM}}$ which reduces the cost from $O(N_{\mathrm{T}}^{\mathrm{TD}^2} N_{\mathrm{EM}}^2)$ to $O(N_{\mathrm{T}}^{\mathrm{TD}} N_{\mathrm{EM}}^2 \log^2 N_{\mathrm{T}}^{\mathrm{TD}})$ operations [83].

6.2.4 Computational Complexity

Next, the computational complexity of the above method is evaluated. Let the average number of the Green functions terms from the summation (6.4) per basis-testing pair in the matrices $\mathbf{Z}_0^{\mathrm{EM}}$ and the other $\mathbf{Z}_{l-l'}^{\mathrm{EM}}$ matrices be denoted as $\bar{N}_{\mathrm{U}}$. In the multidimensional Newton algorithm for solving (6.11), the first step to find the right hand side, requires $O(N_{\mathrm{EM}}^2 \log^2 N_{\mathrm{T}}^{\mathrm{TD}} + N_{\mathrm{CKT}})$ operations. In the second step, the Newton iterations are started. Let $\bar{N}_{\mathrm{N}}^{\mathrm{TD}}$ be the average number of Newton iterations at each time step. For finding the residue, the linear and nonlinear contributions to $\mathbf{F}(\mathbf{X}_l)$ needs to be evaluated which requires $O(\bar{N}_{\mathrm{N}}^{\mathrm{TD}}(N_0^{\mathrm{TD}} + N_{\mathrm{CKT}}))$ where N_0^{TD} is the number of non-

zero entries in the $\mathbf{Z}_0^{\mathrm{EM}}$. Finding the Jacobian and solving the linearized equation requires $O(\bar{N}_{\mathrm{N}}^{\mathrm{TD}}\bar{N}_{\mathrm{I}}^{\mathrm{TD}}(N_0^{\mathrm{TD}}+N_{\mathrm{CKT}}))$ where $\bar{N}_{\mathrm{I}}^{\mathrm{TD}}$ is the average number of solve iterations per Newton iteration per time step. The marching time scales as $O(N_{\mathrm{EM}}^2\log^2 N_{\mathrm{T}}^{\mathrm{TD}}+\bar{N}_{\mathrm{N}}^{\mathrm{TD}}\bar{N}_{\mathrm{I}}^{\mathrm{TD}}N_0^{\mathrm{TD}}+\bar{N}_{\mathrm{N}}^{\mathrm{TD}}\bar{N}_{\mathrm{I}}^{\mathrm{TD}}N_{\mathrm{CKT}})$ per time step.

The filling of matrices in (6.11) requires $O(\bar{N}_{\mathrm{U}}N_{\mathrm{EM}}^2+N_{\mathrm{CKT}})$ operations. For normally incident plane wave, the number of source observer pairs that interact during the whole duration is proportional to $O(N_{\mathrm{T}}^{\mathrm{TD}^2}N_{\mathrm{EM}}^2)$ i.e. $\bar{N}_{\mathrm{U}} \sim N_{\mathrm{T}}^{\mathrm{TD}^2}$. However, for obliquely incident plane wave, all the source observer pairs such that $\hat{\mathbf{k}}^{\mathrm{inc}}\bullet(\mathbf{r}-\mathbf{r}'-\mathbf{r}_{\mathrm{c}}^{m,n})<0$ interact to produce entries in $\mathbf{Z}_0^{\mathrm{EM}}$ and the truncation of the summation in (6.4) is done based on the decay of $1/R^{m,n}$ such that it is to a certain threshold. This leads to very large value of $\bar{N}_{\mathrm{U}}$ and therefore very high matrix fill times. Indeed, the Green function should be represented appropriately using schemes like Ewald's method [81], [84] and other techniques need to alleviate this high matrix fill cost. This will be a future area of research and not addressed here.

Finally, the $O(N_{\mathrm{T}}^{\mathrm{TD}}N_{\mathrm{EM}}^2+N_{\mathrm{CKT}})$ bytes of memory is required to store the matrices, and vectors in the solution of (6.11)

6.3 Fourier Envelope Formulation

The Fourier envelope MOT formulation of the hybrid EM-CKT equations equivalent to the TD-MOT in Section 6.2 is presented here..

6.3.1 EM System of Equations

The fields and induced currents using a truncated series with N_{H} envelopes: as

$$\begin{Bmatrix} \mathbf{E}^{\mathrm{inc},m,n}(\mathbf{r},t) \\ \mathbf{E}^{m,n}(\mathbf{r},t) \\ \mathbf{J}_{\mathrm{S}}^{m,n}(\mathbf{r},t) \\ \mathbf{J}_{\mathrm{V}}^{m,n}(\mathbf{r},t) \end{Bmatrix} \cong \mathrm{Re}\left(\sum_{h=0}^{N_{\mathrm{H}}-1} \begin{Bmatrix} \tilde{\mathbf{E}}^{\mathrm{inc},h,m,n}(\mathbf{r},t) \\ \tilde{\mathbf{E}}^{h,m,n}(\mathbf{r},t) \\ \tilde{\mathbf{J}}_{\mathrm{S}}^{h,m,n}(\mathbf{r},t) \\ \tilde{\mathbf{J}}_{\mathrm{V}}^{h,m,n}(\mathbf{r},t) \end{Bmatrix} e^{jh\omega_0 t} \right) \tag{6.14}$$

Next, the envelopes of the signals in any cell can be expresses as the scaled time-shifted copies of the envelopes of those in the reference cell, i.e. for $h = 0,\ldots,N_{\mathrm{H}}-1$

$$\begin{aligned} \tilde{\mathbf{E}}^{h,m,n}(\mathbf{r},t) &= \tilde{\mathbf{E}}^{h,0,0}(\mathbf{r}-\mathbf{r}_{\mathrm{c}}^{m,n}, t-\hat{\mathbf{k}}^{\mathrm{inc}}\bullet\mathbf{r}_{\mathrm{c}}^{m,n}\ /\ c)e^{-jk_0h(\hat{\mathbf{k}}^{\mathrm{inc}}\bullet\mathbf{r}_{\mathrm{c}}^{m,n})} \\ \tilde{\mathbf{E}}^{\mathrm{inc},h,m,n}(\mathbf{r},t) &= \tilde{\mathbf{E}}^{\mathrm{inc},h,0,0}(\mathbf{r}-\mathbf{r}_{\mathrm{c}}^{m,n}, t-\hat{\mathbf{k}}^{\mathrm{inc}}\bullet\mathbf{r}_{\mathrm{c}}^{m,n}\ /\ c)e^{-jk_0h(\hat{\mathbf{k}}^{\mathrm{inc}}\bullet\mathbf{r}_{\mathrm{c}}^{m,n})} \\ \tilde{\mathbf{J}}_{\mathrm{S}}^{h,m,n}(\mathbf{r},t) &= \tilde{\mathbf{J}}_{\mathrm{S}}^{h,0,0}(\mathbf{r}-\mathbf{r}_{\mathrm{c}}^{m,n}, t-\hat{\mathbf{k}}^{\mathrm{inc}}\bullet\mathbf{r}_{\mathrm{c}}^{m,n}\ /\ c)e^{-jk_0h(\hat{\mathbf{k}}^{\mathrm{inc}}\bullet\mathbf{r}_{\mathrm{c}}^{m,n})} \\ \tilde{\mathbf{J}}_{\mathrm{V}}^{h,m,n}(\mathbf{r},t) &= \tilde{\mathbf{J}}_{\mathrm{V}}^{h,0,0}(\mathbf{r}-\mathbf{r}_{\mathrm{c}}^{m,n}, t-\hat{\mathbf{k}}^{\mathrm{inc}}\bullet\mathbf{r}_{\mathrm{c}}^{m,n}\ /\ c)e^{-jk_0h(\hat{\mathbf{k}}^{\mathrm{inc}}\bullet\mathbf{r}_{\mathrm{c}}^{m,n})} \end{aligned} \tag{6.15}$$

Similar to the time-domain case, the surface and EFIE relating the envelopes of the currents to the fields in the reference cell: for $h = 0,\ldots,N_{\mathrm{H}}-1$

$$\begin{aligned} \hat{n}\times\hat{n}\times(\partial_t + jh\omega_0)\tilde{\mathbf{E}}^{\mathrm{inc},h,0,0} &= \hat{n}\times\hat{n}\times[\nabla(\partial_t + jh\omega_0)(\tilde{\phi}_{\mathrm{S}}^{h,0,0} + \tilde{\phi}_{\mathrm{V}}^{h,0,0}) + \\ &\qquad (\partial_t^2 + 2jh\omega_0\partial_t - h^2\omega_0^2)(\tilde{\mathbf{A}}_{\mathrm{S}}^{h,0,0} + \tilde{\mathbf{A}}_{\mathrm{V}}^{h,0,0}) \qquad \mathbf{r}\in S_{0,0} \\ (\partial_t + jh\omega_0)\tilde{\mathbf{E}}^{\mathrm{inc},h,0,0} &= (\partial_t + jh\omega_0)\tilde{\mathbf{E}}^{\mathrm{tot},h,0,0} + [\nabla(\partial_t + jh\omega_0)(\tilde{\phi}_{\mathrm{S}}^{h,0,0} + \tilde{\phi}_{\mathrm{V}}^{h,0,0}) + \\ &\qquad (\partial_t^2 + 2jh\omega_0\partial_t - h^2\omega_0^2)(\tilde{\mathbf{A}}_{\mathrm{S}}^{h,0,0} + \tilde{\mathbf{A}}_{\mathrm{V}}^{h,0,0})] \qquad \mathbf{r}\in V_{0,0} \end{aligned} \tag{6.16}$$

Here, ∂_t denotes the partial time derivative, $\{\tilde{\phi}_{\mathrm{S}}^{h,0,0}, \tilde{\mathbf{A}}_{\mathrm{S}}^{h,0,0}\}$ ($\{\tilde{\phi}_{\mathrm{V}}^{h,0,0}, \tilde{\mathbf{A}}_{\mathrm{V}}^{h,0,0}\}$) denotes the {electric scalar, magnetic vector} potential due to the currents on the PEC surface (in the dielectric volume) *in all unit cells*, and $\hat{n}$ is the outward pointing unit vector normal to $S_{0,0}$. In (6.16), the envelopes of vector and scalar potentials due to the currents in all unit cells can be expressed as the envelopes potentials scattered by the currents in the reference cells convolved with a periodic Green function i.e. for $h = 0,\ldots,N_{\mathrm{H}}-1$

$$
\begin{aligned}
(\partial_t + jh\omega_0)\tilde{\phi}_{\mathrm{S}}^{h,0,0}(\mathbf{r},t) &= -\frac{1}{\varepsilon}\sum_m\sum_n\iint_{S_{0,0}} \nabla'\bullet\tilde{\mathbf{J}}_{\mathrm{S}}^{h,0,0}(\mathbf{r}',t-t_d^{m,n})\tilde{G}^{h,m,n}(\mathbf{r},\mathbf{r}')ds' \\
\tilde{\mathbf{A}}_{\mathrm{S}}^{h,0,0}(\mathbf{r},t) &= \mu\sum_m\sum_n\iint_{S_{0,0}} [\tilde{\mathbf{J}}_{\mathrm{S}}^{h,0,0}(\mathbf{r}',t-t_d^{m,n})\tilde{G}^{h,m,n}(\mathbf{r},\mathbf{r}')]ds' \\
(\partial_t + jh\omega_0)\tilde{\phi}_{\mathrm{V}}^{h,0,0}(\mathbf{r},t) &= -\frac{1}{\varepsilon}\sum_m\sum_n\iiint_{V_{0,0}} [\nabla'\bullet\tilde{\mathbf{J}}_{\mathrm{V}}^{h,0,0}(\mathbf{r}',t-t_d^{m,n})\tilde{G}^{h,m,n}(\mathbf{r},\mathbf{r}')]dv' \\
\tilde{\mathbf{A}}_{\mathrm{V}}^{h,0,0}(\mathbf{r},t) &= \mu\sum_m\sum_n\iiint_{V_{0,0}} [\tilde{\mathbf{J}}_{\mathrm{V}}^{0,0}(\mathbf{r}',t-t_d^{m,n})G^{h,m,n}(\mathbf{r},\mathbf{r}')]dv'
\end{aligned}
\tag{6.17}
$$

where

$$
\begin{aligned}
t_d^{m,n} &= (\hat{\mathbf{k}}^{\mathrm{inc}}\bullet\mathbf{r}_{\mathrm{c}}^{m,n} + R^{m,n})/c \\
\tilde{G}^{h,m,n}(\mathbf{r},\mathbf{r}') &= \frac{e^{-jhk_0(\hat{\mathbf{k}}^{\mathrm{inc}}\bullet\mathbf{r}_{\mathrm{c}}^{m,n}+R^{m,n})}}{4\pi R^{m,n}}
\end{aligned}
\tag{6.18}
$$

Here, $k_0 = \omega_0 / c$, $R^{m,n} = \mid \mathbf{r} - \mathbf{r}' - \mathbf{r}_{\mathrm{c}}^{m,n} \mid$ is the distance between a source point in the (m,n) unit cell and the observer point in the reference cell. Again as in the time-domain special temporal basis and testing function [58], [82] have to be used along with extrapolation schemes [58], [59] to develop a time-marching solution scheme.as explained next.

To solve (6.16) numerically, the surface and volume in the reference cell are discretized using triangular and tetrahedral elements in the same manner as in the time domain case. Next, the envelope of the current densities are approximated using $N_{\mathrm{T}}N_{\mathrm{EM}}$ ($N_{\mathrm{EM}} = N_{\mathrm{S}} + N_{\mathrm{gap}} + N_{\mathrm{V}}$) temporal-spatial functions, i.e.

$$
\begin{aligned}
\tilde{\mathbf{J}}_{\mathrm{S}}^{h,0,0}(\mathbf{r},t) &\cong \sum_{l'=1}^{N_{\mathrm{T}}}\sum_{k'=1}^{N_{\mathrm{S}}} \tilde{\mathbf{I}}_{l'}^{\mathrm{EM},h}[k']\mathbf{S}_{k'}(\mathbf{r})T_{l'}(t-\hat{\mathbf{k}}^{\mathrm{inc}}\bullet\mathbf{r}_{k'}/c) \\
&\quad + \sum_{l'=1}^{N_{\mathrm{T}}}\sum_{k'=1}^{N_{\mathrm{gap}}} \tilde{\mathbf{I}}_{l'}^{\mathrm{EM},h}[N_{\mathrm{S}}+k']\mathbf{P}_{k'}(\mathbf{r})T_{l'}(t-\hat{\mathbf{k}}^{\mathrm{inc}}\bullet\mathbf{r}_{N_{\mathrm{S}}+k'}/c) \\
\tilde{\mathbf{J}}_{\mathrm{V}}^{0.0}(\mathbf{r},t) &\cong \sum_{l'=1}^{N_{\mathrm{T}}}\sum_{k'=1}^{N_{\mathrm{V}}} \kappa(\mathbf{r})\tilde{\mathbf{I}}_{l'}^{\mathrm{EM},h}[N_{\mathrm{S}}+N_{\mathrm{gap}}+k']\mathbf{V}_{k'}(\mathbf{r})\partial_t T_{l'}(t-\hat{\mathbf{k}}^{\mathrm{inc}}\bullet\mathbf{r}_{N_{\mathrm{S}}+N_{\mathrm{gap}}+k'}/c)
\end{aligned}
\tag{6.19}
$$

Here, $\tilde{\mathbf{I}}_{l'}^{\mathrm{EM},h}$ is an $N_{\mathrm{EM}} \times 1$ vector that stores unknown coefficients, $\mathbf{S}_{k'}, \mathbf{P}_{k'}, \mathbf{V}_{k'}$ are the spatial basis functions which are RWG [71], port basis functions (Section 5.1.3) and SWG [72] basis functions, respectively, $\mathbf{r}_{k'}$ is the center of the basis function $\mathbf{S}_{k'}$, $\mathbf{P}_{k'}$ or $\mathbf{V}_{k'}$. In (6.5), $T_{l'}(t) = T(t - l'\Delta t)$ are the temporal basis functions and Δt is the time step size. As in the time domain formulation $T_{l'}(t)$ are chosen as bandlimited interpolatory functions [59], [67]. Substituting (6.5) in (6.4) and testing the resulting equations with $\mathbf{S}_k(\mathbf{r})\delta(t - \hat{\mathbf{k}}^{\mathrm{inc}} \bullet \mathbf{r}_k \,/\, c)$, $\mathbf{P}_k(\mathbf{r})\delta(t - \hat{\mathbf{k}}^{\mathrm{inc}} \bullet \mathbf{r}_{N_{\mathrm{S}}+k} \,/\, c)$ for the surface EFIE and $\mathbf{V}_k(\mathbf{r})\delta(t - \hat{\mathbf{k}}^{\mathrm{inc}} \bullet \mathbf{r}_{N_{\mathrm{S}}+N_{\mathrm{gap}}+k} \,/\, c)$ for the volume EFIE results in the equation

$$\sum_{l'=-N_{\mathrm{adv}}}^{0} \tilde{\mathbf{Z}}_{l-l'}^{0,0} \tilde{\mathbf{I}}_{l'}^{\mathrm{EM}} = \tilde{\mathbf{V}}_{l}^{\mathrm{EM}} - \sum_{l'=1}^{l-1} \tilde{\mathbf{Z}}_{l-l'}^{0,0} \tilde{\mathbf{I}}_{l'}^{\mathrm{EM}} \quad \text{for } l = 1, \ldots, N_{\mathrm{T}}^{\mathrm{TD}} \tag{6.20}$$

Here

$$N_{\mathrm{adv}} = \max \left\{ \begin{array}{l} 0 \\ \max\limits_{\mathbf{r} \in \mathrm{span}(\mathbf{S}_{k'})} \left\lfloor \left| \mathbf{r} - \mathbf{r}_{k'} \right| / c\Delta t \right\rfloor \\ \max\limits_{\mathbf{r} \in \mathrm{span}(\mathbf{P}_{k'})} \left\lfloor \left| \mathbf{r} - \mathbf{r}_{N_{\mathrm{S}}+k'} \right| / c\Delta t \right\rfloor \\ \max\limits_{\mathbf{r} \in \mathrm{span}(\mathbf{V}_{k'})} \left\lfloor \left| \mathbf{r} - \mathbf{r}_{N_{\mathrm{S}}+N_{\mathrm{gap}}+k'} \right| / c\Delta t \right\rfloor \end{array} \right\} \tag{6.21}$$

For typical problems, the size of the unit cells are comparable to the wavelength of interest and the meshes are approximately tenth or twentieth of the minimum wavelength of interest. The above procedure results in $N_{\mathrm{adv}} \sim 1$ Again, all the port basis functions defined at one device are sampled using the same temporal basis function and tested at the same time. The advanced samples are found using extrapolation similar to the methods described in [59], [67].

6.3.2 CKT System of Equations

The circuit signals using a truncated series with N_{H} envelopes

$$\begin{Bmatrix} \mathbf{V}^{m,n}(t) \\ \mathbf{I}^{\mathrm{nl}m,n}(t) \\ \mathbf{I}^{m,n}(t) \end{Bmatrix} \cong \mathrm{Re}\left(\sum_{h=0}^{N_{\mathrm{H}}-1} \begin{Bmatrix} \tilde{\mathbf{V}}^{h,m,n}(t) \\ \tilde{\mathbf{I}}^{\mathrm{nl}h,m,n}(t) \\ \tilde{\mathbf{I}}^{h,m,n}(t) \end{Bmatrix} e^{jh\omega_0 t} \right) \tag{6.22}$$

The envelopes of the circuit quantities are also time-shifted copies of the those in the reference cell, i.e., for $m,n \in (-\infty,\ldots,-1,0,1,\ldots,\infty)$, $h = 0,\ldots,N_{\mathrm{H}}-1$ [58]

$$\begin{aligned} \tilde{\mathbf{V}}^{h,m,n}(t) &= \tilde{\mathbf{V}}^{h,0,0}(t - \hat{\mathbf{k}}^{\mathrm{inc}} \bullet \mathbf{r}_{\mathrm{c}}^{m,n} \;/\; c) e^{-jk_0 h(\hat{\mathbf{k}}^{\mathrm{inc}} \bullet \mathbf{r}_{\mathrm{c}}^{m,n})} \\ \tilde{\mathbf{I}}^{\mathrm{nl}h,m,n}(t) &= \tilde{\mathbf{I}}^{\mathrm{nl}h,0,0}(t - \hat{\mathbf{k}}^{\mathrm{inc}} \bullet \mathbf{r}_{\mathrm{c}}^{m,n} \;/\; c) e^{-jk_0 h(\hat{\mathbf{k}}^{\mathrm{inc}} \bullet \mathbf{r}_{\mathrm{c}}^{m,n})} \\ \tilde{\mathbf{I}}^{h,m,n}(t) &= \tilde{\mathbf{I}}^{h,0,0}(t - \hat{\mathbf{k}}^{\mathrm{inc}} \bullet \mathbf{r}_{\mathrm{c}}^{m,n} \;/\; c) e^{-jk_0 h(\hat{\mathbf{k}}^{\mathrm{inc}} \bullet \mathbf{r}_{\mathrm{c}}^{m,n})} \end{aligned} \tag{6.23}$$

Again as in the time-domain case, the circuit equation in each unit cell is independent of other unit cells and by enforcing the N_{D} system of equations at times $l\Delta t - \hat{\mathbf{k}}^{\mathrm{inc}} \bullet \mathbf{r}_{1,\ldots,N_{\mathrm{D}}}$ and following the procedure described in Chapter 2, the circuit system of equations is obtained.

$$\tilde{\mathbf{Y}}^{\mathrm{CKT}} \tilde{\mathbf{V}}_l^{\mathrm{CKT}} + \tilde{\mathbf{I}}_l^{\mathrm{nl}}(\tilde{\mathbf{V}}_l^{\mathrm{CKT}}) = \tilde{\mathbf{I}}_l^{\mathrm{CKT}} \tag{6.24}$$

6.3.3 Coupling of EM-CKT equations and Nonlinear Solution Algorithm

The EM structure and devices in the reference cell are coupled using the port model presented in Section 5.1.3 with each of the N_{D} port equations enforced at times $l\Delta t - \hat{\mathbf{k}}^{\mathrm{inc}} \bullet \mathbf{r}_{1,\ldots,N_{\mathrm{D}}}$., the coupling system of equations are obtained. The final system of equations can be expressed as

$$\tilde{\mathbf{F}}(\tilde{\mathbf{X}}_l) = \tilde{\mathbf{b}}_l \quad \text{for } l = 1,\ldots,N_{\mathrm{T}} \tag{6.25}$$

where

$$\tilde{\mathbf{F}}(\tilde{\mathbf{X}}_l) = \begin{bmatrix} \tilde{\mathbf{Z}}_0^{\mathrm{EM}} + \tilde{\mathbf{Z}}_0^{\mathrm{port}} & \tilde{\mathbf{C}}_0^{\mathrm{V}} \\ -\tilde{\mathbf{C}}^{\mathrm{I}} & \tilde{\mathbf{Y}}^{\mathrm{CKT}} \end{bmatrix} \underbrace{\begin{bmatrix} \tilde{\mathbf{I}}_l^{\mathrm{EM}} \\ \tilde{\mathbf{V}}_l^{\mathrm{CKT}} \end{bmatrix}}_{\tilde{\mathbf{x}}_l} + \begin{bmatrix} 0 \\ \tilde{\mathbf{I}}_l^{\mathrm{nl}}(\tilde{\mathbf{V}}_l^{\mathrm{CKT}}) \end{bmatrix} \tag{6.26}$$

and

$$\tilde{\mathbf{b}}_l = \begin{bmatrix} \tilde{\mathbf{V}}_l^{\mathrm{EM}} + \tilde{\mathbf{V}}_l^{\mathrm{port}} - \sum_{l'=\max(1,l-N_{\mathrm{g}})}^{l-1} (\tilde{\mathbf{Z}}_{l-l'}^{\mathrm{EM}} + \tilde{\mathbf{Z}}_{l-l'}^{\mathrm{port}}) \tilde{\mathbf{I}}_{l'}^{\mathrm{EM}} - \sum_{l'=l-3}^{l-1} \tilde{\mathbf{C}}_{l-l'}^{\mathrm{V}} \tilde{\mathbf{V}}_{l'}^{\mathrm{CKT}} \\ \tilde{\mathbf{I}}_l^{\mathrm{CKT}} \end{bmatrix} \tag{6.27}$$

A multidimensional nonlinear solution algorithm identical to that described in Section 3.1.4 is used to solve (6.25). However, as in the time-domain simulator above, in the first step, when finding the right hand side a blocked Toeplitz FFT is used to accelerate the evaluation of $\sum_{l'=1}^{l-1} \tilde{\mathbf{Z}}_{l-l'}^{\mathrm{EM}} \mathbf{I}_{l'}^{\mathrm{EM}}$ which reduces the cost from $O(N_{\mathrm{H}} N_{\mathrm{T}}^2 N_{\mathrm{EM}}^2)$ to $O(N_{\mathrm{H}} N_{\mathrm{T}} N_{\mathrm{EM}}^2 \log^2 N_{\mathrm{T}})$ operations [83].

6.3.4 Computational Complexity

Next, the computational complexity of the Fourier envelope method is evaluated. Let the average number of the Green functions terms from the summation (6.17) per basis-testing pair in the matrices $\tilde{\mathbf{Z}}_0^{\mathrm{EM}}$ and the other $\tilde{\mathbf{Z}}_{l-l'}^{\mathrm{EM}}$ matrices be denoted as $\bar{N}_{\mathrm{U}}$.It should be noted that this number is approximately same for both time domain and Fourier envelope methods. In the nonlinear solution algorithm for solving (6.25), the first step to find the right hand side, requires $O(N_{\mathrm{H}} N_{\mathrm{EM}}^2 \log^2 N_{\mathrm{T}} + N_{\mathrm{H}} N_{\mathrm{CKT}})$ operations. In the second step, the Newton iterations are started. Let $\bar{N}_{\mathrm{N}}$ be the average number of Newton iterations at each time step. For finding the residue, the linear and nonlinear contributions to $\mathbf{F}(\mathbf{X}_l)$ needs to be evaluated which requires $O(\bar{N}_{\mathrm{N}}(N_{\mathrm{H}} N_0 + N_{\mathrm{H}}^2 N_{\mathrm{CKT}}))$ where N_0 is the number of non-zero entries in the $\mathbf{Z}_0^{\mathrm{EM}}$. Finding the Jacobian and solving the linearized equation requires $O(\bar{N}_{\mathrm{N}} \bar{N}_{\mathrm{I}} (N_{\mathrm{H}} N_0 + N_{\mathrm{H}}^2 N_{\mathrm{CKT}}))$ where $\bar{N}_{\mathrm{I}}^{\mathrm{TD}}$ is the average number of solve iterations per Newton iteration per time step. For narrowband problems, $N_0 \approx N_{\mathrm{EM}}^2$ [35] and the marching time scales as $O([\log^2 N_{\mathrm{T}} + \bar{N}_{\mathrm{N}} \bar{N}_{\mathrm{I}}] N_{\mathrm{H}} N_{\mathrm{EM}}^2 + N_{\mathrm{H}}^2 N_{\mathrm{CKT}})$ per time step.

The filling of matrices in (6.26) and (6.27) requires $O(\bar{N}_{\mathrm{U}} N_{\mathrm{H}} N_{\mathrm{EM}}^2 + N_{\mathrm{H}} N_{\mathrm{CKT}})$ operations. Similar to the time-domain case, there exist a problem for obliquely incident plane wave that $\bar{N}_{\mathrm{U}}$ becomes very large and the matrix fill time is very high. Special techniques need to be developed to alleviate this issue

Finally, $O(N_{\mathrm{T}} N_{\mathrm{H}} N_{\mathrm{EM}}^2 + N_{\mathrm{H}}^2 N_{\mathrm{CKT}})$ bytes of memory is required to store the matrices, and vectors in (6.26) and (6.27). The cost comparison between FE scheme and TD schemes is tedious and not straightforward as explained in Section 3.1.5.

6.4 NUMERICAL EXAMPLE

In this section, scattering from varactor diode (SVM1232) loaded artificial magnetic conductor metasurface is analyzed [85]. The varactor diode provides a tuning functionality for the metasurface. The capacitance loading the surface changes depending on the bias voltage which in turn changes the resonant frequency of the metasurface thereby enabling frequency tuning. The metasurface and the reference cell are shown in Fig. 6.2(a) and the diode model is presented in Fig. 6.2(b). The structure is excited by a slowly rising sinusoidal plane wave:

$$\begin{aligned} \mathbf{E}^{\mathrm{inc}}(\mathbf{r},t) &= \hat{x} f((t-\hat{\mathbf{k}}^{\mathrm{inc}}\bullet\mathbf{r}\,/\,c)\,/\,\tau_0)\sin(\omega_0(t-\hat{\mathbf{k}}^{\mathrm{inc}}\bullet\mathbf{r}\,/\,c)) \\ f(t) &= \begin{cases} 0 & \text{for } t \le 0 \\ 10t^3 - 15t^4 + 6t^5 & \text{for } 0 \le t < 1 \\ 1 & \text{for } 1 \le t \end{cases} \end{aligned} \tag{6.28}$$

Here, $\tau_0 = 20\pi\,/\,\omega_0$. First, the analysis is one for synchronous excitation (normal incidence with $\hat{\mathbf{k}}^{\mathrm{inc}} = \hat{z}$), the bias voltage is set to 4V and multiple simulations are done by varying the excitation frequency $\omega_0\,/\,2\pi$ between 1GHz and 4GHz. The steady state portion of the current densities are Fourier transformed to obtain the frequency domain currents, and the frequency domain reflected field $\mathbf{E}^{\mathrm{ref}}$ is computed:

$$\mathbf{E}^{\mathrm{ref}}(\omega_0) \approx -\hat{\mathbf{E}}^{\mathrm{inc}} \frac{c\mu_0}{2d_x d_y} e^{j\mathbf{k}\bullet\mathbf{r}} \left(\iint\limits_{S_{0,0}} \hat{\mathbf{E}}^{\mathrm{inc}} \bullet \mathbf{J}_{\mathrm{S}}^{0,0}(\mathbf{r}', \omega_0) e^{j\mathbf{k}\bullet\mathbf{r}'} ds' + \iiint\limits_{V_{0,0}} \hat{\mathbf{E}}^{\mathrm{inc}} \bullet \mathbf{J}_{\mathrm{V}}^{0,0}(\mathbf{r}', \omega_0) e^{j\mathbf{k}\bullet\mathbf{r}'} dv' \right) \quad (6.29)$$

Here, $\mathbf{k} = \hat{\mathbf{k}}^{\mathrm{inc}}\, \omega_0 / c$. The phase of the reflection coefficient $\Gamma = \hat{\mathbf{E}}^{\mathrm{inc}} \bullet \mathbf{E}^{\mathrm{ref}}(\omega_0) / \left| \mathbf{E}^{\mathrm{inc}}(\omega_0) \right|$ is plotted in Fig. 6.2(c). Apart from this result where the varactor diode is modeled, the results are obtained from an hybrid FDTD-SPICE simulator [85]. It can be observed from Fig. 6.2(c) that the results from all the simulations are close, but the parasitic model of the varactor (not modeled in the other reference simulators) leads to deviated results from the rest. Next, the analysis is repeated for a larger capacitance by setting the diode bias to 0V. Again, there is reasonable agreement with the reference results from [85]. The parasitic effect of the varactor diode shifts the resonant frequency higher as in the previous case.

Lastly, the analysis is repeated for progressively delayed excitation (oblique incidence with $\hat{\mathbf{k}}^{\mathrm{inc}} = \frac{\hat{y}}{\sqrt{2}} + \frac{\hat{z}}{\sqrt{2}}$). Figs. 6.2(d) plots the results obtained for the bias voltage of 4V and 0V , respectively. It is observed that the results from CST and the time-domain simulator with capacitor model agree reasonably . The parasitic of the varactor diode shift the resonance frequency higher as in the previous case.

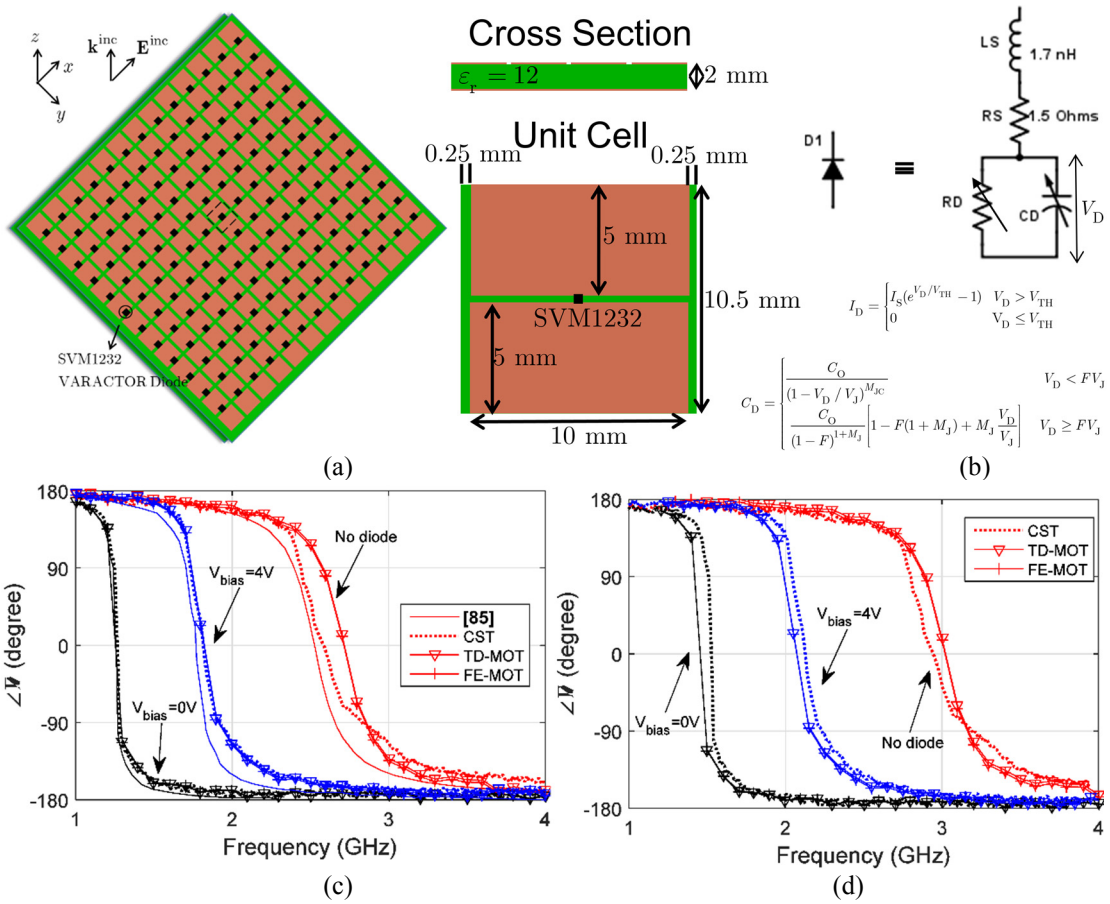

Fig. 6.2. Scattering from tunable metasurface. (a) Varactor loaded metasurface (b) Varactor diode model. Phase of reflection coefficient for (c) normal incidence and (d) oblique incidence.

CHAPTER 7

ENVELOPE TRACKING EM SIMULATOR IN LOSSY MEDIA

In geophysical applications, the background is lossy and transient scattering from objects embedded in this lossy background is of interest. In this chapter, as a preliminary analysis for modeling these applications. an envelope tracking EM simulator is developed for such analysis of scattering from PEC embedded in a lossy medium The formulation is presented in Section 7.1 and numerical. example is described in Section 7.2

7.1 FORMULATION

Consider a PEC structure of surface S residing in a lossy homogeneous background with conductivity σ, permeability μ and permittivity ε. The structure is excited by an electric field $\mathbf{E}^{\text{inc}}(\mathbf{r},t)$ produced due to external impressed sources. The impressed sources are assumed to be essentially bandlimited to the angular frequency band $[\omega_0-\omega_{\text{bw}},\omega_0+\omega_{\text{bw}}]$, where ω_0 is the fundamental carrier frequency and ω_{bw} is the single-sided bandwidth and the incident electric field and the induced currents in this cell are zero for $t\le 0$.Let the incident electric field induce a surface current density $\mathbf{J}(\mathbf{r},t)$ on S .

To model the scattering from the PEC object, zero tangential field are enforced i.e. for $\mathbf{r}\in S$

$$\hat{n}\times\hat{n}\times(\partial_t+\frac{\sigma}{\varepsilon})\mathbf{E}^{\text{inc}}(\mathbf{r},t)=\hat{n}\times\hat{n}\times\iint_S\int_0^{t-R/c}\Big[\mu g(R,t-t')(\partial_t^2+\frac{\sigma}{\varepsilon}\partial_t)\mathbf{J}(\mathbf{r}',t') -\frac{1}{\varepsilon}\nabla g(R,t-t')\nabla'\bullet\mathbf{J}(\mathbf{r}',t')\Big]dt'dS \tag{7.1}$$

Here, $\hat{n}$ is the unit vector normal to S, ∂_t represents the time-derivative operator, $R = \left|\mathbf{r} - \mathbf{r}'\right|$ is the distance between observation point $\mathbf{r}$ and source point $\mathbf{r}'$ and $c = 1/\sqrt{\mu\varepsilon}$ is the speed of light.. The scalar Green function $g(R,\tau)$ is given by [83], [86]

$$g(R,\tau) = \frac{e^{-\sigma\tau/2\varepsilon}}{4\pi}\left[\frac{\delta(t - R/c)}{R} + \frac{\sigma \mathrm{I}_1\left(\frac{\sigma}{2\varepsilon c}\sqrt{c^2\tau^2 - R^2}\right)}{2\varepsilon\sqrt{c^2\tau^2 - R^2}} \cdot u(\tau - R/c_b)\right] \tag{7.2}$$

Here, $\mathrm{I}_1(.)$ is the first-order modified Bessel function of the first kind, and u(.) is the unit step function. Expanding the current and fields in terms of their envelopes,

$$\begin{aligned} \mathbf{E}^{\mathrm{inc}}(\mathbf{r},t) &= \tilde{\mathbf{E}}^{\mathrm{inc}}(r,t)e^{j\omega_0 t} \\ \mathbf{J}(\mathbf{r},t) &= \tilde{\mathbf{E}}^{\mathrm{inc}}(r,t)e^{j\omega_0 t} \end{aligned} \tag{7.3}$$

Here, because the pure envelope simulator is linear, only the fundamental carrier is used. It can be generalized to the multiple harmonic cases described previously. The EFIE can be expressed in terms of the envelopes as

$$\begin{aligned} \hat{n}\times\hat{n}\times(\partial_t + j\omega_0 + \frac{\sigma}{\varepsilon})\tilde{\mathbf{E}}^{\mathrm{inc}}(\mathbf{r},t) = \\ \hat{n}\times\hat{n}\times\iint_S \int_0^{t-R/c}\Big[\mu\tilde{g}(R,t-t')(\partial_t^2 - \omega_0^2 + \frac{\sigma}{\varepsilon}\partial_t + j\omega_0\frac{\sigma}{\varepsilon})\tilde{\mathbf{J}}(\mathbf{r}',t') \\ -\frac{1}{\varepsilon}\nabla\tilde{g}(R,t-t')\nabla'\bullet\tilde{\mathbf{J}}(\mathbf{r}',t')\Big]dt'dS \end{aligned} \tag{7.4}$$

where, $\tilde{g}(R,\tau) = g(R,\tau)e^{-j\omega_0 t}$. To solve the above system of equations numerically, the currents are approximated using $N_{\mathrm{S}}N_{\mathrm{T}}$ space-time basis functions as

$$\tilde{\mathbf{J}}(\mathbf{r},t) \cong \sum_{l'=1}^{N_{\mathrm{T}}}\sum_{k'=1}^{N_{\mathrm{S}}} \mathbf{I}_{l'}^{\mathrm{EM}}[k']\mathbf{S}_{k'}(\mathbf{r}')T_{l'}(t) \tag{7.5}$$

Here $\mathbf{I}_{l'}^{\mathrm{EM}}$ is a $N_{\mathrm{S}} \times 1$ vector of unknown coefficients, $\mathbf{S}_{k'}(\mathbf{r}')$ are RWG functions defined over adjacent triangle edges [71] and $T_{l'}(t) = T(t - l'\Delta t)$ are third order CPPIFs [67]. Substituting (7.5) in (7.4) and Galerkin testing the resulting equations at time instants $t = l\Delta t$ we get a linear system of equation

$$\tilde{\mathbf{Z}}_0 \tilde{\mathbf{I}}_{l'}^{\mathrm{EM}} = \tilde{\mathbf{V}}_l^{\mathrm{EM}} - \sum_{l'=1}^{l-1} \tilde{\mathbf{Z}}_{l-l'} \tilde{\mathbf{I}}_{l'}^{\mathrm{EM}} \text{ for } l = 1,\ldots,N_{\mathrm{T}} \tag{7.6}$$

Here, $\tilde{\mathbf{V}}_l^{\mathrm{EM}}$ is the vector containing the incident electric field tested at all times, and $\tilde{\mathbf{Z}}_{l-l'}$ give the scattered envelopes tested at time $l\Delta t$ due to a current envelope sample at time $l'\Delta t$ .i.e.

$$\begin{aligned}
\tilde{\mathbf{V}}_l^{\mathrm{EM}} &= \iint_S \mathbf{S}_k(\mathbf{r}) \bullet (\partial_t + j\omega_0 + \frac{\sigma}{\varepsilon}) \tilde{\mathbf{E}}^{\mathrm{inc}}(\mathbf{r},t) dS \Big|_{t=l\Delta t} \\
\tilde{\mathbf{Z}}_{l-l'}[k,k'] &= \iint_S \nabla \bullet \mathbf{S}_k(\mathbf{r}) \iint_S \int_0^{t-R/c} \frac{1}{\varepsilon} \tilde{g}(R,t-t') \nabla' \bullet \mathbf{S}_{k'}(\mathbf{r}') T_{l'}(t') dt' dS' dS \Big|_{t=l\Delta t} + \\
&\iint_S \mathbf{S}_k(\mathrm{r}) \bullet \iint_S \int_0^{t-R/c} \mu \tilde{g}(R,t-t') \mathbf{S}_{k'}(\mathrm{r}') (\partial_{\mathrm{t}}^2 - \omega_0^2 + \frac{\sigma}{\varepsilon} \partial_{\mathrm{t}} + \mathrm{j}\omega_0 \frac{\sigma}{\varepsilon}) T_{l'}(t') dt' dS' dS \Big|_{t=l\Delta t}
\end{aligned} \tag{7.7}$$

At each time step $l = 1,\ldots,N_{\mathrm{T}}$, (i) the right hand side of (7.6) is filled. and (ii) (7.6) is solved iteratively At each time step, the right hand side computation requires $O(N_{\mathrm{T}} N_{\mathrm{EM}}^2)$ operations and the iterative solve requires $O(\bar{N}_{\mathrm{I}} N_0)$ operations where $\bar{N}_{\mathrm{I}}$ is the average number of iterations per time step in the linear solver and N_0 is the number of non-zero entries in $\tilde{\mathbf{Z}}_0$. The matrices and current vectors in need $O(N_{\mathrm{T}} N_{\mathrm{EM}}^2)$ bytes of memory and $O(N_{\mathrm{T}} N_{\mathrm{EM}}^2)$ operations to fill. So the dominating cost is the right hand side fill time which scales as $O(N_{\mathrm{T}}^2 N_{\mathrm{EM}}^2)$.

In order to reduce this prohibitive cost, envelope tracking AIM [52] is used. This is similar as the algorithm described in section 5.2 but with a different Green function propagator. approximates the interaction between source and observers (separated by a

distance larger than a threshold) with point sources on a regular grid with N_{C} points. It is formulated by introducing a 3-D regular grid of N_{C} auxiliary nodes that encloses surface S. Using the auxiliary grid, the ET-AIM procedure approximates the $N_{\mathrm{EM}} \times N_{\mathrm{EM}}$ sized impedance matrices $\tilde{\mathbf{Z}}_{l-l'}$ i.e. $\tilde{\mathbf{Z}}_{l-l'} \approx \tilde{\mathbf{Z}}_{l-l'}^{\mathrm{FFT}} + \tilde{\mathbf{Z}}_{l-l'}^{\mathrm{near}}$ where

$$\tilde{\mathbf{Z}}_{l-l'}^{\mathrm{FFT}} = \sum_{i \in \{x,y,z\}} [\Lambda_i^{\dagger} \tilde{\mathbf{G}}_{l-l'}^{\mathrm{A}} \Lambda_i + \Lambda_{\nabla}^{\dagger} \tilde{\mathbf{G}}_{l-l'}^{\phi} \Lambda_{\nabla}] \tag{7.8}$$

Here again, the reduction in the computational cost is obtained by storing and multiplying the sparse anterpolation [54], [75] ($\Lambda_{x,y,z,\nabla}$), propagation matrices ($\tilde{\mathbf{G}}_{l-l'}^{A}, \tilde{\mathbf{G}}_{l-l'}^{\phi}$) and interpolation matrices ($\Lambda_{x,y,z,\nabla}$) instead of explicitly computing $\tilde{\mathbf{Z}}_{l-l'}^{\mathrm{FFT}}$. In (7.8), the anterpolation matrices $\Lambda_{x,y,z,\nabla}$ represent the fields radiated by basis functions in terms of those radiated by point sources on the auxiliary grid; they are obtained using the method followed in [52], [53] by matching the multipole moments of the Cartesian co-ordinate components of $\mathbf{S}_{k'}$ and those of $\nabla \bullet \mathbf{S}_{k'}$, typically to an order of 1 to 5 [52]–[54], [76]. The superscript † represents the transpose operator and the interpolation matrices $\Lambda_{x,y,z,\nabla}^{\dagger}$ represent the fields interpolated from point observers on the auxiliary grid to the testing functions;. The entries of the propagation matrices are

$$\begin{aligned}
\tilde{\mathbf{G}}_{l-l'}^{\mathrm{A}}[u,u'] &= \int_0^{t-R/c} \mu \tilde{g}(\left|\mathbf{r}-\mathbf{r}_{u'}\right|, t-t')(\partial_{\mathrm{t}}^2 - \omega_0^2 + \frac{\sigma}{\varepsilon}\partial_{\mathrm{t}} + \mathrm{j}\omega_0 \frac{\sigma}{\varepsilon}) T_{l'}(t')\, dt' \Big|_{\substack{\mathbf{r}=\mathbf{r}_{\mathrm{n}} \\ t=(l-l')\Delta t}} \\
\tilde{\mathbf{G}}_{l-l'}^{\phi}[u,u'] &= \int_0^{t-R/c} \frac{1}{\varepsilon} \tilde{g}(\left|\mathbf{r}-\mathbf{r}_{u'}\right|, t-t')\, T_{l'}(t')\, dt' \Big|_{\substack{\mathbf{r}=\mathbf{r}_{\mathrm{n}} \\ t=(l-l')\Delta t}}
\end{aligned} \tag{7.9}$$

Here, $\{u, u'\} \in 1, \ldots, N_{\mathrm{C}}$, $\{\mathbf{r}_u, \mathbf{r}_{u'}\}$ represent the observer and source positions on the auxiliary grid. Because of the space-time shift invariance of the free-space Green function [52], [53], the propagation matrices are in block-Toeplitz form and can be multiplied with vectors using FFTs. Blocked 4-D space-time FFTs with varying temporal

FFT sizes [52], [53] are used to multiply the propagation matrices for which $l - l' \neq 0$ during marching in time and 3-D space FFTs are used to multiply $\tilde{\mathbf{G}}_0^A$ and $\tilde{\mathbf{G}}_0^\phi$ during the iterative solution similar to [52], [77].

The near-zone correction matrices $\tilde{\mathbf{Z}}_{l-l'}^{\text{near}}$ are needed to be stored and multiplied at each time-step. The entries of these "pre-corrected" matrices [54], [78] are:

$$\tilde{\mathbf{Z}}_{l-l'}^{\text{near}}[k,k'] = \begin{cases} \tilde{\mathbf{Z}}_{l-l'}^{\text{EM}}[k,k'] - \tilde{\mathbf{Z}}_{l-l'}^{\text{FFT}}[k,k'] & R[k,k'] < \gamma\Delta \\ 0 & \text{otherwise} \end{cases} \tag{7.10}$$

Here, Δ is the grid spacing, and γ is an integer that sets the near-zone size; typically $1 \leq \gamma \leq 6$ [52], $R[k,k']$is the minimum distance between the spatial basis functions k and k'. For narrowband analysis, the distance traveled in one time step ($c\Delta t$) is much larger than the maximum spatial discretization or the near zone size ($\gamma\Delta$). This results in a large number of immediate interactions (matrix entries of $\tilde{\mathbf{Z}}_0^{\text{EM}}$) for source-observer pairs outside the near zone. So $\tilde{\mathbf{Z}}_0^{\text{EM}}$ is also pre-corrected and stored in this scheme similar to [52], [77].

The right hand side fill is computed using 4D FFTs; which requires $O(N_{\text{C}} \log N_{\text{C}} + N_{\text{C}} \log^2 N_{\text{T}})$ operations per time step. Next the linear solve again uses 3D FFTs and hence requires $O(\bar{N}_{\text{I}} N_{\text{C}} \log N_{\text{C}})$ operations per time step. Typically $N_{\text{T}} \gg \bar{N}_{\text{I}}$, and the marching time scales as $O(N_{\text{T}} N_{\text{C}} \log N_{\text{C}} + N_{\text{T}} N_{\text{C}} \log^2 N_{\text{T}})$.The algorithm require $O(N_{\text{T}}(N_{\text{C}} + N_{\text{EM}}))$ bytes to store and matrices and vectors used in the algorithm and $O(N_{\text{T}}(N_{\text{C}} + N_{\text{EM}}))$ operations to fill them. Compared to its time-domain counterpart the costs which are proportional to N_{T} is greatly reduced as bandwidth reduces.

7.2 NUMERICAL EXAMPLE

Here, the EM scattering from a plate due to a plane wave incident is analyzed. The plate is of size $4\ \mathrm{m} \times 4\ \mathrm{m}$ and is set in the x-y plane and residing in a medium with permeability μ_0, permittivity ε_0 and conductivity $\sigma = 0.3\ \mathrm{mS/m}$. The normal plane wave incident on the plate is a modulated Gaussian pulse:

$$\mathbf{E}^{\mathrm{inc}}(\mathbf{r},t) = \hat{x}\, \mathrm{e}^{-(t-t_{\mathrm{d}}+z/c)^2/2\xi^2} \cos(\omega_0(t - t_{\mathrm{d}} + z\,/\,c)) \tag{7.11}$$

Here, $\omega_0\ /\ 2\pi = 300\ \mathrm{MHz}$, $\xi = 0.1\ /\ 2\pi\ \mu\mathrm{s}$ and $t_{\mathrm{d}} = 6.0\xi$. The plane wave has less than 0.1% energy outside the frequency band $\omega_0 \pm \omega_{\mathrm{bw}}$ where $\omega_{\mathrm{bw}} = 30\ \mathrm{MHz}$ .The plate is discretized into 4720 elements (on a 40 x 40 mesh). The current in the center of the plate is found using FE-AIM simulation using $\Delta t = \pi\ /\ \omega_0 \approx 1.6666\ \mathrm{ns}$; compared

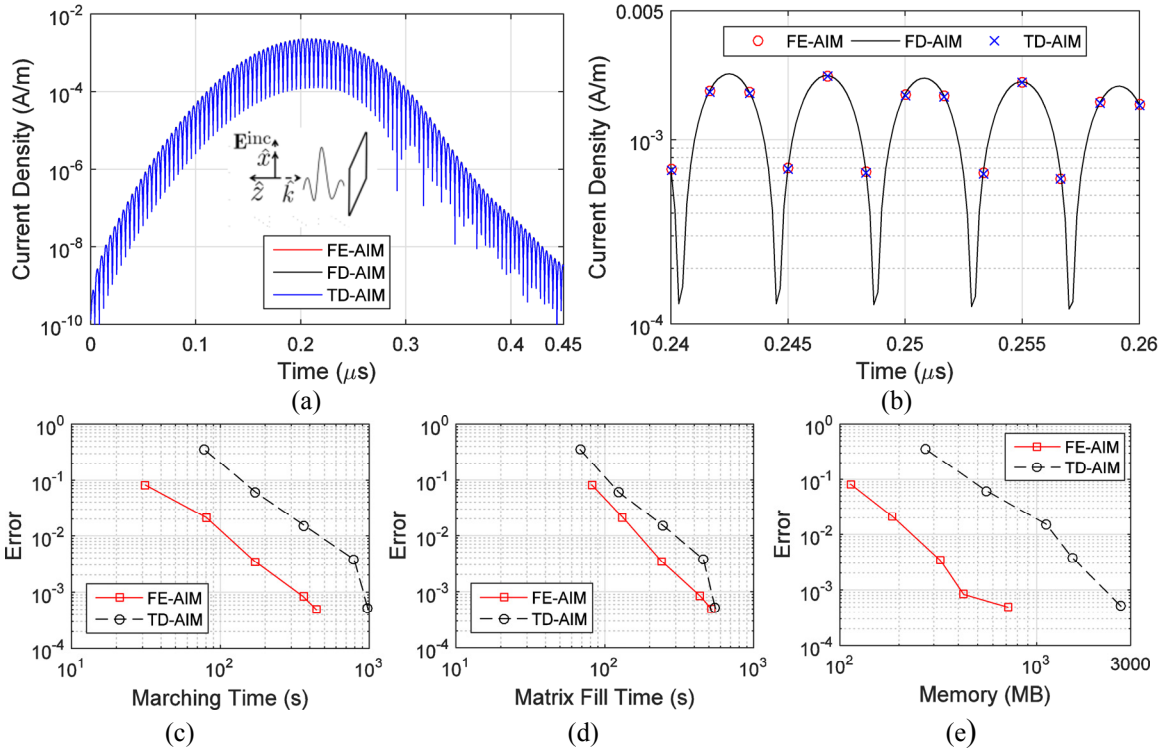

Fig. 7.1. Scattering from a 4m x 4m plate in lossy medium (a) Current density at the center of the plate. (b) Current density near the peak. (c) Error vs. Marching time. (d) Error vs. Matrix fill time. (e) Error vs. Memory

with TD-AIM simulation using $\Delta t = \pi \,/\, 10\omega_0 \approx 0.1666$ ns and FD-AIM simulations.in Figs. 7.1(a) and 7.1(b). FD-AIM results are obtained by solving the system at multiple frequencies and the time-domain response is obtained through Fourier transforms. Figs. 7.1(a) & (b) demonstrate that all three results agree well and there is no late time instabilities. Next the error accrued in the simulation is plotted against the marching time, matrix fill time and memory used in Figs 7.1(c)-7.1(e). Here, the error is computed using (3.18) with $N_{\mathrm{T}}\Delta t = 0.45$ μs and the reference is an inverse Fourier transformed current obtained from frequency domain simulations. Since, all three costs depend on the number of time steps, the envelope tracking scheme has an advantage over the time-domain counterpart as observed here.

CHAPTER 8

CONCLUSIONS AND FUTURE WORK

This dissertation presented envelope-tracking hybrid EM-CKT simulator for analyzing nonlinearly loaded EM modules under various scenarios. This chapter summarizes the conclusions found in each of the scenarios and the future avenues of research.

8.1 CONCLUSIONS

An hybrid EM-CKT simulator was developed for analyzing scattering from wire antennas loaded by nonlinear devices. In the proposed simulator, each signal of interest is expressed as a truncated series of harmonic sinusoids (N_{H} harmonics) modulated by time varying envelopes. Thin-wire EFIE and Kirchhoff's equations are formulated in terms of the envelopes and are enforced on the wires and in the lumped device models, respectively. The resulting EM and CKT equations are coupled at lumped ports and the hybrid system of equations are solved by using a multi-dimensional Newton-Raphson scheme while marching in time. Because CKT models do not generally yield closed-form equations that relate the *envelopes* of currents through nonlinear elements to the *envelopes* of voltages across them, in the proposed simulator, these equations are estimated numerically from the time-domain equations that relate currents and voltages. This requires a three-step procedure, where voltage samples are obtained from voltage-envelope samples, nonlinear equations are evaluated to find current samples, and these samples are used to obtain current-envelope samples. This approximation affects the accuracy and bandwidth of analysis possible. In this dissertation, this procedure is approximated by assuming the envelopes are varying slowly compared to the

fundamental carrier. The computational costs of the proposed envelope-tracking simulator are as follows: It requires N_{H} times larger number of operations/memory for setting up/storing the necessary matrices compared to its time-domain counterpart. It also requires $O(\bar{N}_{\mathrm{N}}\bar{N}_{\mathrm{I}}[N_{\mathrm{H}}N_{\mathrm{EM}}^2 + N_{\mathrm{H}}^2 N_{\mathrm{CKT}}])$ operations per time step rather than $O(N_{\mathrm{EM}}^2 + \bar{N}_{\mathrm{N}}^{\mathrm{TD}}\bar{N}_{\mathrm{I}}^{\mathrm{TD}}(N_0^{\mathrm{TD}} + N_{\mathrm{CKT}}))$ operations per time step. These higher costs are offset by the facts that envelope tracking requires fewer time steps and yields more accurate results. Numerical results showed that the error vs. cost tradeoff of the proposed envelope-tracking simulator is generally better compared to its time-domain counterpart. Simulations for a dipole loaded by a weakly nonlinear Gunn diode or a strongly nonlinear *p-n* junction diode, a rectenna composed of a dipole loaded with a 3-stage voltage multiplier, and a phase conjugating frequency selective surface composed of 100 dipoles loaded with Gunn diodes confirmed that the narrower is the band of excitation or the weaker is the nonlinearity, the more advantageous is the envelope-tracking method.

The two parameters that affect the accuracy of the three-step estimation of the envelope of the current across the nonlinear elements, viz. the time instants at which the time-domain quantities are evaluated and the interpolation scheme used to approximate the envelopes at these time instants, were investigated. Simulations of a *p-n* diode loaded dipole antenna and an 10×10 array of Gunn-diode loaded dipole antennas show that the validity of the three-step procedure can be extended if either the time instants are chosen closer to the present time step or a higher order interpolation scheme is used. These schemes enable broader band envelope-tracking simulations to be performed.

The EM simulator is extended to include PEC and dielectric structures. As in the case of the wires, all the signals are expresses in terms of its envelopes Surface/Volume EFIE and Kirchhoff's equations are formulated in terms of the envelopes and are

enforced on the PEC/dielectrics and in the lumped device models, respectively. The resulting EM and CKT equations are coupled at lumped ports and the hybrid system of equations are solved by using a multi-dimensional Newton-Raphson scheme while marching in time similar to the described in Chapter 3. The computational cost of this vanilla simulator is $O(\bar{N}_{\mathrm{N}}\bar{N}_{\mathrm{I}}[N_{\mathrm{H}}N_{\mathrm{EM}}^2 + N_{\mathrm{H}}^2 N_{\mathrm{CKT}}])$ which is prohibitive due to the large values of N_{EM} and $\bar{N}_{\mathrm{I}}$ Adaptive integral method was used to alleviate the first issue while two sparse near field preconditioners, viz. INF and SAI are proposed to alleviate the second. It was seen that the three step approximation didn't work well when the loads where active devices and the solution did not converge at various time steps. Numerical results analyzing a mixer and rectenna were presented that validate the proposed ETAIM procedure. It demonstrates that FEAIM is more efficient than TDAIM for narrowband problems and the sparse preconditioners can improve the solution time 3.5-5 times with a slight increase in the matrix fill cost compared to the diagonal preconditioner.

An EM-CKT simulator is formulated for periodic structures. The equations were formulated in terms of periodic Green function. Numerical results showing the use for analyzing tunable metasurfaces was demonstrated. Here it was observed that the EM system of equation is non-causal for obliquely incident excitation. Extrapolation was used to find the future samples required. Temporal basis functions were chosen to be BLIFs and the basis-testing scheme was modified to reduce the number of time samples. However, in case of oblique incidence, the matrix fill time is increased due to a very large number of source observer interactions

An envelope tracking simulator solving the scattering of PEC objects embedded in lossy medium is formulated and tested. The costs depend on the number of time steps,

thereby making envelope tracking schemes more efficient than time domain simulations for the example presented

8.2 FUTURE WORK

Using asynchronous time stepping [28] and adaptive time stepping [29] can be further used to do make the method more efficient. Asynchronous time samples each CKT system and EM module at different time steps thereby making it faster. Adaptive time step can be used to reduce the time step size to improve the nonlinear solution convergence.

For the nonlinearly loaded PECs and dielectric bodies, other preconditioners [87] and techniques like inverting the circuit system and using the Schur complement in the EM system to improve the convergence of the solution at each time step need to be developed for employing these hybrid EM-CKT solver to solve real problems involving transistors, and other CKT elements.

In the EM-CKT simulator for periodic structures, is not yet solved. Indeed, as a future work, alternative representations of the Green function like the Ewald scheme or its time-domain equivalents [81], [84], must be used and developed for the above proposed algorithm to be useful for simulating more complex scenarios. In the future, AIM must also be applied to reduce the cost of these simulators.

Careful cost comparisons need to be done for the analysis of objects in lossy media. The formulation has to be extended to include lossy and lossless dispersive dielectrics in order to simulate complex problems arising geoscience applications.

APPENDIX I – ELEMENT STAMPS OF CIRCUIT COMPONENTS

The contributions of each of the circuit components (resistors, capacitor, inductors, independent voltage and current sources, nonlinear VCCS nonlinear resistor and nonlinear capacitors) to the matrix $\tilde{\mathbf{Y}}$ and vectors $\tilde{\mathbf{I}}_l^{\mathrm{nl}}$, $\tilde{\mathbf{I}}_l^{\mathrm{CKT}}$ are described here. The matrices and vectors are sum of all the contributions of the individual element stamps described below. Note that all the active circuit elements like diodes, transistors etc. are modeled as an equivalent circuit comprising of the above components.

RESISTOR

Let a resistor R in the circuit connected between nodes n and n'. The equation relating the current flowing from node n to node n' ($I_R = I_n - I_{n'}$) and the voltage difference is $I_R(t) = (V_n(t) - V_{n'}(t)) \,/\, R$ and their envelopes are given by

$$\tilde{I}_R^h(t) = (\tilde{V}_n^h(t) - \tilde{V}_{n'}^h(t)) \,/\, R \quad \text{for } h = 0,\ldots,N_{\mathrm{H}} - 1 \tag{A.1}$$

The trapezoidal rule applied to the MNA relationship for this resistor yields entries to the matrix $\tilde{\mathbf{Y}}$: for $h = 0,\ldots,N_{\mathrm{H}} - 1$

$$\begin{aligned} \tilde{\mathbf{Y}}^h[n,n] &= \tilde{\mathbf{Y}}^h[n',n'] = 1 \,/\, R \\ \tilde{\mathbf{Y}}^h[n,n'] &= \tilde{\mathbf{Y}}^h[n',n] = -1 \,/\, R \end{aligned} \tag{A.2}$$

LINEAR VCCS

Let the current in the branch connected between nodes b and b' be related to the voltage difference between nodes n and n' as $I_b(t) - I_{b'}(t) = g_{\mathrm{m}}(V_n(t) - V_{n'}(t))$ and their envelopes are given by

$$\tilde{I}_b^h(t) - \tilde{I}_{b'}^h(t) = g_{\mathrm{m}}(\tilde{V}_n^h(t) - \tilde{V}_{n'}^h(t)) \quad \text{for } h = 0,\ldots,N_{\mathrm{H}} - 1 \tag{A.3}$$

The trapezoidal rule applied to the MNA relationship for VCCS yields entries to the matrix $\tilde{\mathbf{Y}}$: for $h = 0,\ldots,N_{\mathrm{H}}-1$

$$\begin{aligned}\tilde{\mathbf{Y}}^h[b,n] &= \tilde{\mathbf{Y}}^h[b',n'] = g_{\mathrm{m}} \\ \tilde{\mathbf{Y}}^h[b',n] &= \tilde{\mathbf{Y}}^h[b,n'] = -g_{\mathrm{m}}\end{aligned} \tag{A.4}$$

INDEPENDENT CURRENT SOURCE

Let there be a current source be in the branch b connected between nodes n and n' with the relationship $\tilde{I}_n^h(t) - \tilde{I}_{n'}^h(t) = \tilde{I}_{\mathrm{in}}^h(t)$ for $h = 0,\ldots,N_{\mathrm{H}}-1$ where $V_{\mathrm{in}}(t)$ is a known voltage source. The trapezoidal rule yields entries to the right hand side vector $\tilde{\mathbf{I}}_l^{\mathrm{CKT}}$: for $h = 0,\ldots,N_{\mathrm{H}}-1$

$$\begin{aligned}\tilde{\mathbf{I}}_l^{\mathrm{CKT},h}[n] &= \tilde{I}_{\mathrm{in}}^h(l\Delta t) \\ \tilde{\mathbf{I}}_l^{\mathrm{CKT},h}[n'] &= -\tilde{I}_{\mathrm{in}}^h(l\Delta t)\end{aligned} \tag{A.5}$$

INDEPENDENT VOLTAGE SOURCE

Let there be a voltage source be in the branch b connected between nodes n and n' with the relationship $\tilde{V}_n^h(t) - \tilde{V}_{n'}^h(t) = \tilde{V}_{\mathrm{in}}^h(t)$ for $h = 0,\ldots,N_{\mathrm{H}}-1$ where $V_{\mathrm{in}}(t)$ is a known voltage source. The trapezoidal rule yields entries to the matrix $\tilde{\mathbf{Y}}$ and the right hand side vector $\tilde{\mathbf{I}}_l^{\mathrm{CKT}}$: for $h = 0,\ldots,N_{\mathrm{H}}-1$

$$\begin{aligned}\tilde{\mathbf{Y}}^h[N_{\mathrm{nod}}-1+b,n] &= \tilde{\mathbf{Y}}^h[n,N_{\mathrm{nod}}-1+b] = 1 \\ \tilde{\mathbf{Y}}^h[N_{\mathrm{nod}}-1+b,n'] &= \tilde{\mathbf{Y}}^h[n',N_{\mathrm{nod}}-1+b] = -1 \\ \tilde{\mathbf{I}}_l^{\mathrm{CKT},h}[N_{\mathrm{nod}}-1+b] &= \tilde{V}_{\mathrm{in}}^h(l\Delta t)\end{aligned} \tag{A.6}$$

CAPACITOR

Let a capacitor C in the circuit be connected between nodes n and n'. The equation relating the current flowing from node n to node n' ($I_C = I_n - I_{n'}$) and the

voltage difference $V_n - V_{n'}$ is $I_C(t) = C\partial_t(V_n(t) - V_{n'}(t))$ and their envelopes are given by

$$\tilde{I}_C^h(t) = C(\partial_t + jh\omega_0)(\tilde{V}_n^h(t) - \tilde{V}_{n'}^h(t)) \quad \text{for } h = 0,\ldots,N_{\mathrm{H}} - 1 \tag{A.7}$$

The trapezoidal rule applied to the MNA relationship for this capacitor yields the entries to the matrix $\tilde{\mathbf{Y}}$ and the right hand side vector $\tilde{\mathbf{I}}_l^{\mathrm{CKT}}$: for $h = 0,\ldots,N_{\mathrm{H}} - 1$

$$\begin{aligned} \tilde{\mathbf{Y}}^h[n,n] &= \tilde{\mathbf{Y}}^h[n',n'] = (\frac{2}{\Delta t} + jh\omega_0)C \\ \tilde{\mathbf{Y}}^h[n,n'] &= \tilde{\mathbf{Y}}^h[n',n] = -(\frac{2}{\Delta t} + jh\omega_0)C \end{aligned} \tag{A.8}$$

$$\begin{aligned} \tilde{\mathbf{I}}_l^{\mathrm{CKT},h}[n] &= -(\frac{2}{\Delta t} - jh\omega_0)C(\tilde{\mathbf{V}}_{l-1}^{\mathrm{CKT}}[n] - \tilde{\mathbf{V}}_{l-1}^{\mathrm{CKT}}[n']) - (\tilde{\mathbf{I}}^{\mathrm{CKT},h}[n] - \tilde{\mathbf{I}}^{\mathrm{CKT},h}[n']) \\ \tilde{\mathbf{I}}_l^{\mathrm{CKT},h}[n'] &= (\frac{2}{\Delta t} - jh\omega_0)C(\tilde{\mathbf{V}}_{l-1}^{\mathrm{CKT}}[n] - \tilde{\mathbf{V}}_{l-1}^{\mathrm{CKT}}[n']) + (\tilde{\mathbf{I}}^{\mathrm{CKT},h}[n] - \tilde{\mathbf{I}}^{\mathrm{CKT},h}[n']) \end{aligned} \tag{A.9}$$

The above expressions is the same as a combination of a complex-valued resistor $1 / (2 / \Delta t + jh\omega_0)C$ in parallel with a current source depending on the past values $-(2 / \Delta t - jh\omega_0)C(\tilde{\mathbf{V}}_{l-1}^{\mathrm{CKT}}[n] - \tilde{\mathbf{V}}_{l-1}^{\mathrm{CKT}}[n'])$ $-(\tilde{\mathbf{I}}^{\mathrm{CKT},h}[n] - \tilde{\mathbf{I}}^{\mathrm{CKT},h}[n'])$

INDUCTOR

Let an inductor L in the circuit be connected between nodes n and n'. The equation relating the current flowing from node n to node n' ($I_L = I_n - I_{n'}$) and the voltage difference $V_n - V_{n'}$ is $V_n(t) - V_{n'}(t) = L\partial_t I_L(t)$ and their envelopes are given by

$$(\tilde{V}_n^h(t) - \tilde{V}_{n'}^h(t)) = L(\partial_t + jh\omega_0)I_L(t) \text{ for } h = 0,\ldots,N_{\mathrm{H}} - 1 \tag{A.10}$$

The trapezoidal rule applied to the MNA relationship for this inductor yields the entries to the matrix $\tilde{\mathbf{Y}}$ and the right hand side vector $\tilde{\mathbf{I}}_l^{\mathrm{CKT}}$: for $h = 0,\ldots,N_{\mathrm{H}} - 1$

$$\tilde{\mathbf{Y}}^h[n,n] = \tilde{\mathbf{Y}}^h[n',n'] = \frac{1}{(\frac{2}{\Delta t} + jh\omega_0)L}$$
$$\tilde{\mathbf{Y}}^h[n,n'] = \tilde{\mathbf{Y}}^h[n',n] = -\frac{1}{(\frac{2}{\Delta t} + jh\omega_0)L} \tag{A.11}$$

$$\tilde{\mathbf{I}}_l^{\mathrm{CKT},h}[n] = \frac{(\tilde{\mathbf{V}}_{l-1}^{\mathrm{CKT}}[n] - \tilde{\mathbf{V}}_{l-1}^{\mathrm{CKT}}[n'])}{(\frac{2}{\Delta t} + jh\omega_0)L} + \frac{(\frac{2}{\Delta t} - jh\omega_0)}{(\frac{2}{\Delta t} + jh\omega_0)}(\tilde{\mathbf{I}}^{\mathrm{CKT},h}[n] - \tilde{\mathbf{I}}^{\mathrm{CKT},h}[n'])$$
$$\tilde{\mathbf{I}}_l^{\mathrm{CKT},h}[n'] = -\frac{(\tilde{\mathbf{V}}_{l-1}^{\mathrm{CKT}}[n] - \tilde{\mathbf{V}}_{l-1}^{\mathrm{CKT}}[n'])}{(\frac{2}{\Delta t} + jh\omega_0)L} - \frac{(\frac{2}{\Delta t} - jh\omega_0)}{(\frac{2}{\Delta t} + jh\omega_0)}(\tilde{\mathbf{I}}^{\mathrm{CKT},h}[n] - \tilde{\mathbf{I}}^{\mathrm{CKT},h}[n']) \tag{A.12}$$

Again, like the capacitor, the above expressions is a combination of a complex valued resistor $(2 / \Delta t + jh\omega_0)L$ and a current source depending on past values.

NONLINEAR VCCS AND NONLINEAR RESISTORS

Let the current flowing through the branch connecting nodes b and b' $I_{\mathrm{nl}}(t)$ be related to the voltage between nodes n and n'.as $I_{\mathrm{nl}}(t) = f(V_n(t) - V_{n'}(t))$. This nonlinear current-voltage relationship do not generally have a closed form expression relating the envelopes of the current and the voltage. It creates nonzero $\tilde{\mathbf{I}}_l^{\mathrm{nl},h}[b]$ and $\tilde{\mathbf{I}}_l^{\mathrm{nl},h}[b']$ which are computed numerically as described in Section 2.2. Also there are non-zero entries in the Jacobian matrices in (2.10) and (2.11). The nonlinear resistor is a special case when the current is in the branch connecting nodes n and n'.

NONLINEAR CAPACITOR

Let a nonlinear capacitor be connected between nodes n and n', The current flowing through the capacitor ($I_{\mathrm{nl}C} = I_n - I_{n'}$) is related to the voltage difference

$V_n - V_{n'}$ by $I_{\mathrm{nl}C}(t) = \partial_t Q((V_n(t) - V_{n'}(t)))$ where Q is a known function. and the envelopes are given by: for $h=0,\ldots,N_{\mathrm{H}}-1$

$$\tilde{I}_n^h(t) - \tilde{I}_{n'}^h(t) = (\partial_t + jh\omega_0)\tilde{Q}_{\mathrm{V}}^h(t) \tag{A.13}$$

Here, $Q(V_n(t) - V_{n'}(t)) \approx \mathrm{Re}(\sum_{h=0}^{N_{\mathrm{H}}-1} \tilde{Q}_{\mathrm{V}}^h e^{jh\omega 0t})$. Note that there are no closed form expressions for $\tilde{Q}_{\mathrm{V}}^h(t)$. The trapezoidal rule applied to the MNA relationship for this capacitor yields the entries to the vector $\tilde{\mathbf{I}}_l^{\mathrm{nl}}$ and the right hand side vector $\tilde{\mathbf{I}}_l^{\mathrm{CKT}}$:

$$\begin{aligned}
\mathbf{I}_l^{\mathrm{nl},h}[n] &= \left(\frac{2}{\Delta t} + j\omega_0 h\right)\tilde{Q}_{\mathrm{V}}^h(l\Delta t) \\
\mathbf{I}_l^{\mathrm{nl},h}[n'] &= -\left(\frac{2}{\Delta t} + j\omega_0 h\right)\tilde{Q}_{\mathrm{V}}^h(l\Delta t)
\end{aligned} \tag{A.14}$$

$$\begin{aligned}
\mathbf{I}_l^{\mathrm{CKT},h}[n] &= \mathbf{I}_{l-1}^{\mathrm{CKT},h}[n'] - \mathbf{I}_{l-1}^{\mathrm{CKT},h}[n] - \left(\frac{2}{\Delta t} - j\omega_0 h\right)\tilde{Q}_{\mathrm{V}}^h((l-1)\Delta t) \\
\mathbf{I}_l^{\mathrm{CKT},h}[n'] &= -\mathbf{I}_{l-1}^{\mathrm{CKT},h}[n'] + \mathbf{I}_{l-1}^{\mathrm{CKT},h}[n] + \left(\frac{2}{\Delta t} - j\omega_0 h\right)\tilde{Q}_{\mathrm{V}}^h((l-1)\Delta t)
\end{aligned} \tag{A.15}$$

for $h = 0,\ldots,N_{\mathrm{H}}-1$. Again, the envelope samples are computed using the method described in Section 2.2. Also there are non-zero entries in the Jacobian matrices in (2.10) and (2.11) corresponding to the entries in $\mathbf{I}_l^{\mathrm{nl},h}[n]$ and $\mathbf{I}_l^{\mathrm{nl},h}[n']$.

APPENDIX II – EM MATRIX AND VECTOR ENTRIES FOR WIRES

In (3.6), the $\tilde{\mathbf{V}}_l^{\mathrm{EM}}$ is an $N_{\mathrm{H}}N_{\mathrm{EM}} \times 1$ vector composed of N_{H} blocks of size $N_{\mathrm{EM}} \times 1$ and $\tilde{\mathbf{Z}}_{l-l'}^{\mathrm{EM}}$ are $N_{\mathrm{H}}N_{\mathrm{EM}} \times N_{\mathrm{H}}N_{\mathrm{EM}}$ matrices composed of $N_{\mathrm{H}} \times N_{\mathrm{H}}$ blocks of size $N_{\mathrm{EM}} \times N_{\mathrm{EM}}$. Each block $\tilde{\mathbf{V}}_l^{\mathrm{EM},h}$ represents the (tested) envelope h of the incident electric field and each block $\tilde{\mathbf{Z}}_{l-l'}^{\mathrm{EM},h,h'}$ represents the contribution of the envelope h' of the current to the (tested) envelope h of the scattered electric field; $\tilde{\mathbf{Z}}_{l-l'}^{\mathrm{EM},h,h'} = 0$ if $h \neq h'$ because of the linearity of EM equations. Because the basis and testing functions are defined over two segments, the entries of these vectors and matrices can be decomposed as $\tilde{\mathbf{V}}_l^{\mathrm{EM},h}[k] = \tilde{V}_{l,k_+}^{\mathrm{EM},h} + \tilde{V}_{l,k_-}^{\mathrm{EM},h}$ and $\tilde{\mathbf{Z}}_{l-l'}^{\mathrm{EM},h,h}[k,k'] = \tilde{Z}_{l-l',k_+,k'_+}^{\mathrm{EM},h,h} + \tilde{Z}_{l-l',k_-,k'_+}^{\mathrm{EM},h,h} + \tilde{Z}_{l-l',k_+,k'_-}^{\mathrm{EM},h,h} + \tilde{Z}_{l-l',k_-,k'_-}^{\mathrm{EM},h,h}$. Here,

$$
\begin{aligned}
\tilde{V}_{l,k_\mp}^{\mathrm{EM},h} &= \int_0^{L_{k_\mp}} \hat{l}_{k_\mp} W_k(\mp\xi) \bullet (\partial_t + jh\omega_0) \tilde{\mathbf{E}}^{\mathrm{inc},h}(\mathbf{r}_k \mp \xi \hat{l}_{k_\mp}, l\Delta t) d\xi \\
\tilde{Z}_{l-l',k_\mp,k'_\mp}^{\mathrm{EM},h,h} &= \int_0^{L_{k_\mp}} \int_0^{L_{k'_\mp}} \left[\frac{\mp 1}{\varepsilon L_{k_\mp}} \frac{\mp 1}{L_{k'_\mp}} T(t - \frac{R_a}{c}) + \mu W_k(\mp\xi) \hat{l}_{k_\mp} \right. \\
&\qquad \bullet \hat{l}_{k'_\mp} W_{k'}(\mp\xi')(\partial_t^2 + 2jh\omega_0 \partial_t - h^2\omega_0^2) \\
&\qquad \left. \times T(t - \frac{R_a}{c}) \right] \frac{e^{-jhk_0 R_a}}{4\pi R_a} d\xi d\xi' \Bigg|_{t=(l-l')\Delta t}
\end{aligned}
\tag{A.16}
$$

for $k, k' = 1, \ldots, N_{\mathrm{EM}}$. In (A.16), $\{k_+, k_-\}$ ($\{k'_+, k'_-\}$) denotes the {first, second} cylindrical segment corresponding to the k^{th} testing (k'^{th} basis) function, and $L_{k_\mp}$ ($L_{k'_\mp}$) denotes the length of the segment $k_\mp$ ($k'_\mp$). Note that the reduced thin-wire kernel is used here, i.e., $R_a = \sqrt{|\, \mathbf{r}_k \mp \xi \hat{l}_{k_\mp} - \mathbf{r}_{k'} \pm \xi' \hat{l}_{k'_\mp} \,|^2 + a_{k'}^2}$ if the source and observer segments are on the same wire and $R_a \approx |\, \mathbf{r}_k \mp \xi \hat{l}_{k_\mp} - \mathbf{r}_{k'} \pm \xi' \hat{l}_{k'_\mp} \,|$ otherwise. Here, $\mathbf{r}_k$ ($\mathbf{r}_{k'}$) denotes the point where the axis of the two segments corresponding to the k^{th} testing (k'^{th} basis) function intersect and $a_{k'}$ denotes the radius of the two wire segments

corresponding to the k'^{th} basis function. The reduced kernel should be replaced with the exact kernel to obtain more accurate results [66], [88], [89].

APPENDIX III – COUPLING MATRIX ENTRIES

In (3.9) (3.10) and (3.11), the coupling matrices $\tilde{\mathbf{C}}^{\mathrm{V}}_{l-l'}$ and $\tilde{\mathbf{C}}^{\mathrm{I}}$ are block-diagonal matrices; their blocks correspond to different devices and are denoted as $\tilde{\mathbf{C}}^{\mathrm{V},1}_{l-l'},\ldots,\tilde{\mathbf{C}}^{\mathrm{V},N_{\mathrm{D}}}_{l-l'}$ and $\tilde{\mathbf{C}}^{\mathrm{I},1},\ldots,\tilde{\mathbf{C}}^{\mathrm{I},N_{\mathrm{D}}}$. Each of these blocks has $N_{\mathrm{H}}\times N_{\mathrm{H}}$ sub-blocks that represent coupling between different envelopes and are denoted by $\tilde{\mathbf{C}}^{\mathrm{V},D,h,h'}_{l-l'}$ and $\tilde{\mathbf{C}}^{\mathrm{I},D,h,h'}$ for device $D=1,\ldots,N_{\mathrm{D}}$. Because of the linear EM-CKT coupling the off-diagonal blocks are zero; i.e., $\tilde{\mathbf{C}}^{\mathrm{V},D,h,h'}_{l-l'}=\tilde{\mathbf{C}}^{\mathrm{I},D,h,h'}=0$ if $h\neq h'$. If device D has one port and is at a gap where the wire radius is a_D then

$$\begin{aligned}\tilde{\mathbf{C}}^{\mathrm{I},D,h,h} &= \mathbf{C}^{D^T}\\ \tilde{\mathbf{C}}^{\mathrm{V},D,h,h}_{0} &= 2\pi a_D(\zeta_0+j\omega_0 h)\mathbf{C}^{D}\\ \tilde{\mathbf{C}}^{\mathrm{V},D,h,h}_{l-l'} &= 2\pi a_D\zeta_{l-l'}\mathbf{C}^{D}\end{aligned} \tag{A.17}$$

for $1\le l-l'\le 3$. Here, the third order backward differential formula coefficients are given as $\{\zeta_0,\zeta_1,\zeta_2,\zeta_3\} = \{11/6,-3,3/2,-1/3\}/\Delta t$. The matrix $\mathbf{C}^D$ is an $N_{\mathrm{EM}}\times N^D_{\mathrm{CKT}}$ connectivity matrix that identifies the port in device D and the wire basis that the device is centered on; it has a single nonzero entry that is 1.

APPENDIX IV – JACOBIAN EQUATION MATRIX/VECTOR ENTRIES

In (3.16), $\tilde{\tilde{\mathbf{s}}}_p$ is a size $(2N_{\mathrm{H}}-1)(N_{\mathrm{EM}}+N_{\mathrm{CKT}})$ vector that stores the real and imaginary parts of the Newton step $\tilde{\mathbf{s}}_p = [\tilde{\mathbf{s}}_p^{\mathrm{EM}^T}, \tilde{\mathbf{s}}_p^{\mathrm{CKT}^T}]^T$, which is a complex vector of size $N_{\mathrm{H}}(N_{\mathrm{EM}}+N_{\mathrm{CKT}})$. The EM part of the Newton step vector is formed by concatenating N_{H} vectors of size N_{EM} as $\tilde{\mathbf{s}}_p^{\mathrm{EM}}[hN_{\mathrm{EM}}+1:(h+1)N_{\mathrm{EM}}] = \tilde{\mathbf{s}}_p^{\mathrm{EM},h}[1:N_{\mathrm{EM}}]$ for $h = 0,\ldots,N_{\mathrm{H}}-1$. The CKT part of it is formed by concatenating the vectors $\tilde{\mathbf{s}}_p^{\mathrm{CKT},1},\ldots,\tilde{\mathbf{s}}_p^{\mathrm{CKT},N_{\mathrm{D}}}$; each of which correspond to a different device and is formed by concatenating N_{H} vectors of size N_{CKT}^D, i.e., $\tilde{\mathbf{s}}_p^{\mathrm{CKT},D}[hN_{\mathrm{CKT}}^D+1:(h+1)N_{\mathrm{CKT}}^D] = \tilde{\mathbf{s}}_p^{\mathrm{CKT},D,h}[1:N_{\mathrm{CKT}}^D]$ for $h = 0,\ldots,N_{\mathrm{H}}-1$. Thus, the Newton step is stored as $\tilde{\tilde{\mathbf{s}}}_p = [\tilde{\tilde{\mathbf{s}}}_p^{\mathrm{EM}^T}, \tilde{\tilde{\mathbf{s}}}_p^{\mathrm{CKT},1^T},\ldots,\tilde{\tilde{\mathbf{s}}}_p^{\mathrm{CKT},N_{\mathrm{D}}{}^T}]^T$, where

$$\tilde{\tilde{\mathbf{s}}}_p^{\mathrm{EM}} = \begin{bmatrix} \tilde{\mathbf{s}}_p^{\mathrm{EM},0} \\ \mathrm{Re}(\tilde{\mathbf{s}}_p^{\mathrm{EM},1}) \\ \mathrm{Im}(\tilde{\mathbf{s}}_p^{\mathrm{EM},1}) \\ \vdots \\ \mathrm{Re}(\tilde{\mathbf{s}}_p^{\mathrm{EM},N_{\mathrm{H}}-1}) \\ \mathrm{Im}(\tilde{\mathbf{s}}_p^{\mathrm{EM},N_{\mathrm{H}}-1}) \end{bmatrix} \quad \tilde{\tilde{\mathbf{s}}}_p^{\mathrm{CKT},D} = \begin{bmatrix} \tilde{\mathbf{s}}_p^{\mathrm{CKT},D,0} \\ \mathrm{Re}(\tilde{\mathbf{s}}_p^{\mathrm{CKT},D,1}) \\ \mathrm{Im}(\tilde{\mathbf{s}}_p^{\mathrm{CKT},D,1}) \\ \vdots \\ \mathrm{Re}(\tilde{\mathbf{s}}_p^{\mathrm{CKT},D,N_{\mathrm{H}}-1}) \\ \mathrm{Im}(\tilde{\mathbf{s}}_p^{\mathrm{CKT},D,N_{\mathrm{H}}-1}) \end{bmatrix} \tag{A.18}$$

for $D = 1,\ldots,N_{\mathrm{D}}$. The real residual vector $\tilde{\tilde{\mathbf{r}}}_{l,p-1}$ is similarly expressed in terms of the complex one $\tilde{\mathbf{r}}_{l,p-1}$.

In (A.18), the matrix $\tilde{\tilde{\mathbf{Z}}}_0^{\mathrm{EM}}$ is a real block-diagonal matrix of size $(2N_{\mathrm{H}}-1)N_{\mathrm{EM}} \times (2N_{\mathrm{H}}-1)N_{\mathrm{EM}}$; its blocks are of size $N_{\mathrm{EM}} \times N_{\mathrm{EM}}$ and store the real and imaginary parts of the complex matrix $\tilde{\mathbf{Z}}_0^{\mathrm{EM}}$, i.e., $\tilde{\tilde{\mathbf{Z}}}_0^{\mathrm{EM},0,0} = \tilde{\mathbf{Z}}_0^{\mathrm{EM},0,0}$, and

$$\tilde{\tilde{\mathbf{Z}}}_0^{\mathrm{EM},h,h} = \begin{bmatrix} \mathrm{Re}(\tilde{\mathbf{Z}}_0^{\mathrm{EM},h,h}) & -\mathrm{Im}(\tilde{\mathbf{Z}}_0^{\mathrm{EM},h.h}) \\ \mathrm{Im}(\tilde{\mathbf{Z}}_0^{\mathrm{EM},h,h}) & \mathrm{Re}(\tilde{\mathbf{Z}}_0^{\mathrm{EM},h.h}) \end{bmatrix} \tag{A.19}$$

for $h = 1,\ldots,N_{\mathrm{H}}-1$. The matrices $\tilde{\tilde{\mathbf{Y}}}^{\mathrm{CKT}}, \tilde{\tilde{\mathbf{C}}}^{\mathrm{I}}, \tilde{\tilde{\mathbf{C}}}_0^{\mathrm{V}}$, and $\tilde{\tilde{\mathbf{J}}}_{l,p}^{\mathrm{nl}}$ are also real block-diagonal matrices; their blocks correspond to different devices and are denoted as $\tilde{\tilde{\mathbf{Y}}}^{D}, \tilde{\tilde{\mathbf{C}}}^{\mathrm{I},D}, \tilde{\tilde{\mathbf{C}}}_0^{\mathrm{V},D}$, and $\tilde{\tilde{\mathbf{J}}}_{l,p}^{\mathrm{nl},D}$ for $D = 1,\ldots,N_{\mathrm{D}}$. These are size $(2N_{\mathrm{H}}-1)N_{\mathrm{CKT}}^{D} \times (2N_{\mathrm{H}}-1)N_{\mathrm{CKT}}^{D}$ matrices; each $N_{\mathrm{CKT}}^{D} \times N_{\mathrm{CKT}}^{D}$ sub-block of these blocks represents interaction between two envelopes; thus, $\tilde{\tilde{\mathbf{Y}}}^{D}, \tilde{\tilde{\mathbf{C}}}^{\mathrm{I},D}$, and $\tilde{\tilde{\mathbf{C}}}_0^{\mathrm{V},D}$ are block-diagonal matrices, while $\tilde{\tilde{\mathbf{J}}}_{l,p}^{\mathrm{nl},D}$ is dense. The first sub-blocks of these matrices are $\tilde{\tilde{\mathbf{Y}}}^{D,0,0} = \tilde{\mathbf{Y}}^{D,0,0}$, $\tilde{\tilde{\mathbf{C}}}^{\mathrm{I},D,0,0} = \mathbf{C}^{D^T}$, $\tilde{\tilde{\mathbf{C}}}_0^{\mathrm{V},D,0,0} = 2\pi a_D \zeta_0 \mathbf{C}^{D}$, and $\tilde{\tilde{\mathbf{J}}}_{l,p}^{\mathrm{nl},D,0,0} = \tilde{\mathbf{J}}_{l,p}^{\mathrm{Rnl},D,0,0}$; the rest are (for $h, h' = 1,\ldots,N_{\mathrm{H}}-1$)

$$\begin{aligned}
\tilde{\tilde{\mathbf{Y}}}^{D,h,h} &= \begin{bmatrix} \mathrm{Re}(\tilde{\mathbf{Y}}^{D,h}) & -\mathrm{Im}(\tilde{\mathbf{Y}}^{D,h}) \\ \mathrm{Im}(\tilde{\mathbf{Y}}^{D,h}) & \mathrm{Re}(\tilde{\mathbf{Y}}^{D,h}) \end{bmatrix} \\
\tilde{\tilde{\mathbf{C}}}^{\mathrm{I},D,h,h} &= \begin{bmatrix} \mathbf{C}^{D} & 0 \\ 0 & \mathbf{C}^{D} \end{bmatrix}^{T} \\
\tilde{\tilde{\mathbf{C}}}_0^{\mathrm{V},D,h,h} &= 2\pi a_D \begin{bmatrix} \zeta_0 \mathbf{C}^{D} & -h\omega_0 \mathbf{C}^{D} \\ h\omega_0 \mathbf{C}^{D} & \zeta_0 \mathbf{C}^{D} \end{bmatrix} \\
\tilde{\tilde{\mathbf{J}}}^{\mathrm{nl},D,0,h'} &= \begin{bmatrix} \mathrm{Re}(\tilde{\mathbf{J}}^{\mathrm{Rnl},D,0,h'}) & -\mathrm{Re}(\tilde{\mathbf{J}}^{\mathrm{Inl},D,0,h'}) \end{bmatrix} \\
\tilde{\tilde{\mathbf{J}}}^{\mathrm{nl},D,h,0} &= \begin{bmatrix} \mathrm{Re}(\tilde{\mathbf{J}}^{\mathrm{Rnl},D,h,0}) \\ \mathrm{Im}(\tilde{\mathbf{J}}^{\mathrm{Rnl},D,h,0}) \end{bmatrix} \\
\tilde{\tilde{\mathbf{J}}}^{\mathrm{nl},D,h,h'} &= \begin{bmatrix} \mathrm{Re}(\tilde{\mathbf{J}}^{\mathrm{Rnl},D,h,h'}) & -\mathrm{Re}(\tilde{\mathbf{J}}^{\mathrm{Inl},D,h,h'}) \\ \mathrm{Im}(\tilde{\mathbf{J}}^{\mathrm{Rnl},D,h,h'}) & -\mathrm{Im}(\tilde{\mathbf{J}}^{\mathrm{Inl},D,h,h'}) \end{bmatrix}
\end{aligned} \tag{A.20}$$

APPENDIX V – EM MATRIX AND VECTOR ENTRIES FOR SURFACES/VOLUMES

In (5.12), the $\tilde{\mathbf{V}}_l^{\mathrm{EM}}$ and $\tilde{\mathbf{V}}_l^{\mathrm{EM}}$ are $N_{\mathrm{H}}N_{\mathrm{EM}} \times 1$ vectors composed of N_{H} blocks of size $N_{\mathrm{EM}} \times 1$ and Each block $\tilde{\mathbf{V}}_l^{\mathrm{EM},h}$ and $\tilde{\mathbf{V}}_l^{\mathrm{port},h}$ represents the different components of (tested) envelope h of the incident electric field. Here, for $h = 0,\ldots,N_{\mathrm{H}} - 1$

$$\tilde{\mathbf{V}}_l^{\mathrm{EM},h}[k] = \begin{cases} \iint\limits_S \mathbf{S}_k(\mathbf{r}) \bullet (\partial_t + jh\omega_0)\mathbf{E}^{\mathrm{inc}}(\mathbf{r},t)dS \Big|_{t=l\Delta t} & k \le N_{\mathrm{S}} \\ \iint\limits_S \mathbf{P}_{k-N_{\mathrm{S}}}(\mathbf{r}) \bullet (\partial_t + jh\omega_0)\mathbf{E}^{\mathrm{inc}}(\mathbf{r},t)dS \Big|_{t=l\Delta t} & N_{\mathrm{S}} < k \le N_{\mathrm{S}} + N_{\mathrm{gap}} \\ \iiint\limits_V \mathbf{V}_{k-N_{\mathrm{S}}-N_{\mathrm{gap}}}(\mathbf{r}) \bullet (\partial_t + jh\omega_0)\mathbf{E}^{\mathrm{inc}}(\mathbf{r},t)dV \Big|_{t=l\Delta t} & N_{\mathrm{S}} + N_{\mathrm{gap}} < k \le N_{\mathrm{EM}} \end{cases} \quad \text{(A.21)}$$

Here, $\tilde{\mathbf{V}}_l^{\mathrm{port},h}$ is composed of the tested electric field in the port gap. So $\tilde{\mathbf{V}}_l^{\mathrm{port},h}[1 : N_{\mathrm{S}}] = 0$ and $\tilde{\mathbf{V}}_l^{\mathrm{port},h}[N_{\mathrm{S}} + N_{\mathrm{P}} + 1 : N_{\mathrm{EM}}] = 0$. The rest of the non-zero entries of the vector are given by

$$\tilde{\mathbf{V}}_l^{\mathrm{port},h}[N_{\mathrm{S}} + k] = \frac{1}{l_{\mathrm{gap},k}} \iint\limits_{S_{\mathrm{gap},k}} (\partial_t + jh\omega_0)\tilde{\mathbf{E}}^{\mathrm{inc},h}(\mathbf{r},t) \bullet \hat{h}_k dh dl \Big|_{t=l\Delta t} \quad 1 < k \le N_{\mathrm{P}} \quad \text{(A.22)}$$

In (5.11) and (5.12), $\tilde{\mathbf{Z}}_{l-l'}^{\mathrm{EM}}$ are $N_{\mathrm{H}}N_{\mathrm{EM}} \times N_{\mathrm{H}}N_{\mathrm{EM}}$ matrices composed of $N_{\mathrm{H}} \times N_{\mathrm{H}}$ blocks of size $N_{\mathrm{EM}} \times N_{\mathrm{EM}}$ .Each block $\tilde{\mathbf{Z}}_{l-l'}^{\mathrm{EM},h,h'}$ represents the contribution of the envelope h' of the current to the (tested) envelope h of the scattered electric field; $\tilde{\mathbf{Z}}_{l-l'}^{\mathrm{EM},h,h'} = 0$ if $h \neq h'$ because of the linearity of EM equations. Here, for $h = 0,\ldots,N_{\mathrm{H}} - 1$

$$
\tilde{\mathbf{Z}}_{l-l'}^{\mathrm{EM},h,h}[k,k'] =
$$

$$
\begin{cases}
\left.\begin{array}{l}\iint_S \mathbf{S}_k(\mathbf{r})\bullet(\partial_t^2 + 2jh\omega_0\partial_t - h^2\omega_0^2)\tilde{\mathbf{A}}_{\mathrm{S},k'}^h(\mathbf{r},t)dS \\ \quad +\nabla\bullet\mathbf{S}_k(\mathbf{r})(\partial_t + jh\omega_0)\tilde{\phi}_{\mathrm{S},k'}^h(\mathbf{r},t)dS\end{array}\right|_{t=(l-l')\Delta t} & k,k' \le N_{\mathrm{S}} \\
\left.\begin{array}{l}\iint_S \mathbf{P}_{k-N_{\mathrm{S}}}(\mathbf{r})\bullet(\partial_t^2 + 2jh\omega_0\partial_t - h^2\omega_0^2)\tilde{\mathbf{A}}_{\mathrm{S},k'}^h(\mathbf{r},t)dS \\ \quad +\nabla\bullet\mathbf{P}_{k-N_{\mathrm{S}}}(\mathbf{r})(\partial_t + jh\omega_0)\tilde{\phi}_{\mathrm{S},k'}^h(\mathbf{r},t)dS\end{array}\right|_{t=(l-l')\Delta t} & \begin{array}{l}N_{\mathrm{S}} < k \le N_{\mathrm{S}} + N_{\mathrm{gap}} \\ k' \le N_{\mathrm{S}}\end{array} \\
\left.\begin{array}{l}\iiint_V \mathbf{V}_{k-N_{\mathrm{S}}-N_{\mathrm{gap}}}(\mathbf{r})\bullet(\partial_t^2 + 2jh\omega_0\partial_t - h^2\omega_0^2)\tilde{\mathbf{A}}_{\mathrm{S},k'}^h(\mathbf{r},t)dV \\ \quad +\nabla\bullet\mathbf{V}_{k-N_{\mathrm{S}}-N_{\mathrm{gap}}}(\mathbf{r})(\partial_t + jh\omega_0)\tilde{\phi}_{\mathrm{S},k'}^h(\mathbf{r},t)dV\end{array}\right|_{t=(l-l')\Delta t} & \begin{array}{l}N_{\mathrm{S}} + N_{\mathrm{gap}} < k \le N_{\mathrm{EM}} \\ k' \le N_{\mathrm{S}}\end{array} \\
\left.\begin{array}{l}\iint_S \mathbf{S}_k(\mathbf{r})\bullet(\partial_t^2 + 2jh\omega_0\partial_t - h^2\omega_0^2)\tilde{\mathbf{A}}_{\mathrm{P},k'}^h(\mathbf{r},t)dS \\ \quad +\nabla\bullet\mathbf{S}_k(\mathbf{r})(\partial_t + jh\omega_0)\tilde{\phi}_{\mathrm{P},k'}^h(\mathbf{r},t)dS\end{array}\right|_{t=(l-l')\Delta t} & \begin{array}{l}k \le N_{\mathrm{S}} \\ N_{\mathrm{S}} < k' \le N_{\mathrm{S}} + N_{\mathrm{gap}}\end{array} \\
\left.\begin{array}{l}\iint_S \mathbf{P}_{k-N_{\mathrm{S}}}(\mathbf{r})\bullet(\partial_t^2 + 2jh\omega_0\partial_t - h^2\omega_0^2)\tilde{\mathbf{A}}_{\mathrm{P},k'}^h(\mathbf{r},t)dS \\ \quad +\nabla\bullet\mathbf{P}_{k-N_{\mathrm{S}}}(\mathbf{r})(\partial_t + jh\omega_0)\tilde{\phi}_{\mathrm{P},k'}^h(\mathbf{r},t)dS\end{array}\right|_{t=(l-l')\Delta t} & \begin{array}{l}N_{\mathrm{S}} < k \le N_{\mathrm{S}} + N_{\mathrm{gap}} \\ N_{\mathrm{S}} < k' \le N_{\mathrm{S}} + N_{\mathrm{gap}}\end{array} \\
\left.\begin{array}{l}\iiint_V \mathbf{V}_{k-N_{\mathrm{S}}-N_{\mathrm{gap}}}(\mathbf{r})\bullet(\partial_t^2 + 2jh\omega_0\partial_t - h^2\omega_0^2)\tilde{\mathbf{A}}_{\mathrm{P},k'}^h(\mathbf{r},t)dV \\ \quad +\nabla\bullet\mathbf{V}_{k-N_{\mathrm{S}}-N_{\mathrm{gap}}}(\mathbf{r})(\partial_t + jh\omega_0)\tilde{\phi}_{\mathrm{P},k'}^h(\mathbf{r},t)dV\end{array}\right|_{t=(l-l')\Delta t} & \begin{array}{l}N_{\mathrm{S}} + N_{\mathrm{gap}} < k \le N_{\mathrm{EM}} \\ N_{\mathrm{S}} < k' \le N_{\mathrm{S}} + N_{\mathrm{gap}}\end{array} \\
\left.\begin{array}{l}\iint_S \mathbf{S}_k(\mathbf{r})\bullet(\partial_t^2 + 2jh\omega_0\partial_t - h^2\omega_0^2)\tilde{\mathbf{A}}_{\mathrm{V},k'}^h(\mathbf{r},t)dS \\ \quad +\nabla\bullet\mathbf{S}_k(\mathbf{r})(\partial_t + jh\omega_0)\tilde{\phi}_{\mathrm{V},k'}^h(\mathbf{r},t)dS\end{array}\right|_{t=(l-l')\Delta t} & \begin{array}{l}k \le N_{\mathrm{S}} \\ N_{\mathrm{S}} + N_{\mathrm{gap}} < k' \le N_{\mathrm{EM}}\end{array} \\
\left.\begin{array}{l}\iint_S \mathbf{P}_{k-N_{\mathrm{S}}}(\mathbf{r})\bullet(\partial_t^2 + 2jh\omega_0\partial_t - h^2\omega_0^2)\tilde{\mathbf{A}}_{\mathrm{V},k'}^h(\mathbf{r},t)dS \\ \quad +\nabla\bullet\mathbf{P}_{k-N_{\mathrm{S}}}(\mathbf{r})(\partial_t + jh\omega_0)\tilde{\phi}_{\mathrm{V},k'}^h(\mathbf{r},t)dS\end{array}\right|_{t=(l-l')\Delta t} & \begin{array}{l}N_{\mathrm{S}} < k \le N_{\mathrm{S}} + N_{\mathrm{gap}} \\ N_{\mathrm{S}} + N_{\mathrm{gap}} < k' \le N_{\mathrm{EM}}\end{array} \\
\left.\begin{array}{l}\iiint_V \mathbf{V}_{k-N_{\mathrm{S}}-N_{\mathrm{gap}}}(\mathbf{r})\bullet(\partial_t^2 + 2jh\omega_0\partial_t - h^2\omega_0^2)\tilde{\mathbf{A}}_{\mathrm{V},k'}^h(\mathbf{r},t)dV \\ \quad +\nabla\bullet\mathbf{V}_{k-N_{\mathrm{S}}-N_{\mathrm{gap}}}(\mathbf{r})(\partial_t + jh\omega_0)\tilde{\phi}_{\mathrm{V},k'}^h(\mathbf{r},t)dV\end{array}\right|_{t=(l-l')\Delta t} & \begin{array}{l}N_{\mathrm{S}} + N_{\mathrm{gap}} < k \le N_{\mathrm{EM}} \\ N_{\mathrm{S}} + N_{\mathrm{gap}} < k' \le N_{\mathrm{EM}}\end{array}
\end{cases}
\tag{A.23}
$$

The envelopes of the time derivatives of the vector potentials and scalar potentials in (A.23) are given by

$$
\begin{aligned}
&(\partial_t^2 + 2jh\omega_0\partial_t - h^2\omega_0^2)\tilde{\mathbf{A}}^h_{\mathrm{S},k'}(\mathbf{r},t) = \\
&\quad\begin{cases}\mu\iint\limits_S \mathbf{S}_{k'}(\mathbf{r}')(\partial_t^2 + 2jh\omega_0\partial_t - h^2\omega_0^2)T(t-R/c)\dfrac{e^{-jhk_0R}}{4\pi R}dS' & 1\le k'\le N_{\mathrm{S}} \\ 0 & \text{otherwise}\end{cases} \\
&(\partial_t^2 + 2jh\omega_0\partial_t - h^2\omega_0^2)\tilde{\mathbf{A}}^h_{\mathrm{P},k'+N_{\mathrm{S}}}(\mathbf{r},t) = \\
&\quad\begin{cases}\mu\iint\limits_S \mathbf{P}_{k'}(\mathbf{r}')(\partial_t^2 + 2jh\omega_0\partial_t - h^2\omega_0^2)T(t-R/c)\dfrac{e^{-jhk_0R}}{4\pi R}dS' & 1\le k'\le N_{\mathrm{gap}} \\ 0 & \text{otherwise}\end{cases} \\
&(\partial_t^2 + 2jh\omega_0\partial_t - h^2\omega_0^2)\tilde{\mathbf{A}}^h_{\mathrm{V},k'+N_{\mathrm{S}}+N_{\mathrm{gap}}}(\mathbf{r},t) = \\
&\quad\begin{cases}\mu\iiint\limits_V \mathbf{V}_{k'}(\mathbf{r}')(\partial_t^2 + 2jh\omega_0\partial_t - h^2\omega_0^2)T(t-R/c)\dfrac{e^{-jhk_0R}}{4\pi R}dV' & 1\le k'\le N_{\mathrm{V}} \\ 0 & \text{otherwise}\end{cases}
\end{aligned}
\tag{A.24}
$$

and

$$
\begin{aligned}
(\partial_t + jh\omega_0)\tilde{\phi}^h_{\mathrm{S},k'}(\mathbf{r},t) &= \begin{cases}-\iint\limits_S \nabla\bullet\mathbf{S}_{k'}(\mathbf{r}')T(t-R/c)\dfrac{e^{-jhk_0R}}{4\pi\varepsilon R}dS' & k\le N_{\mathrm{S}} \\ 0 & \text{otherwise}\end{cases} \\
(\partial_t + jh\omega_0)\tilde{\phi}^h_{\mathrm{P},k'+N_{\mathrm{S}}}(\mathbf{r},t) &= \begin{cases}-\iint\limits_S \nabla\bullet\mathbf{P}_{k'}(\mathbf{r}')T(t-R/c)\dfrac{e^{-jhk_0R}}{4\pi\varepsilon R}dS' & 1< k'\le N_{\mathrm{gap}} \\ 0 & \text{otherwise}\end{cases} \\
(\partial_t + jh\omega_0)\tilde{\phi}^h_{\mathrm{V},k'+N_{\mathrm{S}}+N_{\mathrm{gap}}}(\mathbf{r},t) &= \begin{cases}-\iiint\limits_V \nabla\bullet V_{k'}(\mathbf{r}')T(t-R/c)\dfrac{e^{-jhk_0R}}{4\pi\varepsilon R}dV' & 1< k'\le N_{\mathrm{V}} \\ 0 & \text{otherwise}\end{cases}
\end{aligned}
\tag{A.25}
$$

In (5.11) and (5.12), $\tilde{\mathbf{Z}}^{\mathrm{port}}_{l-l'}$ represent the average line integral of the electric field in the gap. The non-zero entries of the $\tilde{\mathbf{Z}}^{\mathrm{port},h,h'}_{l-l'}$ are given as: for $h = 0,\ldots,N_{\mathrm{H}}-1$ and $1\le k\le N_{\mathrm{gap}}$

$$\tilde{\mathbf{Z}}_{l-l'}^{\text{port},h,h'}[k+N_{\text{S}},k'] =$$

$$\begin{cases} \dfrac{1}{l_{\text{gap},k}} \iint\limits_{S_{\text{gap},k}} (\partial_t^2 + 2jh\omega_0\partial_t - h^2\omega_0^2)\tilde{\mathbf{A}}_{\text{S},k'}^{h}(\mathbf{r},t)\bullet\hat{h}_k dldh\Big|_{t=(l-l')\Delta t} & k' \le N_{\text{S}} \\ \dfrac{1}{l_{\text{gap},k}} \iint\limits_{S_{\text{gap},k}} (\partial_t^2 + 2jh\omega_0\partial_t - h^2\omega_0^2)\tilde{\mathbf{A}}_{\text{P},k'}^{h}(\mathbf{r},t)\bullet\hat{h}_k dldh\Big|_{t=(l-l')\Delta t} & N_{\text{S}} < k' \le N_{\text{S}} + N_{\text{gap}} \\ \dfrac{1}{l_{\text{gap},k}} \iint\limits_{S_{\text{gap},k}} (\partial_t^2 + 2jh\omega_0\partial_t - h^2\omega_0^2)\tilde{\mathbf{A}}_{\text{V},k'}^{h}(\mathbf{r},t)\bullet\hat{h}_k dldh\Big|_{t=(l-l')\Delta t} & N_{\text{S}} + N_{\text{gap}} < k' \le N_{\text{EM}} \end{cases} \quad \text{(A.26)}$$

In (5.12), the coupling matrices $\tilde{\mathbf{C}}_{l-l'}^{\text{V}}$ and $\tilde{\mathbf{C}}^{\text{I}}$ are block-diagonal matrices; their blocks correspond to different port basis denoted as $\tilde{\mathbf{C}}_{l-l'}^{\text{V},1},\ldots,\tilde{\mathbf{C}}_{l-l'}^{\text{V},N_{\text{D}}}$ and $\tilde{\mathbf{C}}^{\text{I},1},\ldots,\tilde{\mathbf{C}}^{\text{I},N_{\text{D}}}$. Each of these blocks has $N_{\text{H}} \times N_{\text{H}}$ sub-blocks that represent coupling between different envelopes and are denoted by $\tilde{\mathbf{C}}_{l-l'}^{\text{V},D,h,h'}$ and $\tilde{\mathbf{C}}^{\text{I},D,h,h'}$ for devices $D = 1,\ldots,N_{\text{D}}$. Because of the linear EM-CKT coupling the off-diagonal blocks are zero; i.e., $\tilde{\mathbf{C}}_{l-l'}^{\text{V},D,h,h'} = \tilde{\mathbf{C}}^{\text{I},D,h,h'} = 0$ if $h \neq h'$. For e.g. let the first two port basis be defined to connect The non-zero entries are given as

$$\begin{aligned} \tilde{\mathbf{C}}^{\text{I},D,h,h} &= \mathbf{C}^{D^T} \\ \tilde{\mathbf{C}}_{0}^{\text{V},D,h,h} &= 2\pi a_D(\zeta_0 + j\omega_0 h)\mathbf{C}^D \\ \tilde{\mathbf{C}}_{l-l'}^{\text{V},D,h,h} &= 2\pi a_D \zeta_{l-l'}\mathbf{C}^D \end{aligned} \quad \text{(A.27)}$$

for $1 \le l - l' \le 3$. Here, the third order backward differential formula coefficients are given as $\{\zeta_0,\zeta_1,\zeta_2,\zeta_3\} = \{11/6,-3,3/2,-1/3\}/\Delta t$. The matrix $\mathbf{C}^D$ is an $N_{\text{EM}} \times N_{\text{CKT}}^D$ connectivity matrix that identifies the port in device D and the wire basis that the device is centered on; it has a single nonzero entry that is 1.

REFERENCES

[1] P. V. Nikitin and K. S. Rao, "Theory and measurement of backscattering from RFID tags," *IEEE Antennas Propag. Mag.*, vol. 48, no. 6, pp. 212–218, 2006.

[2] A. Babakhani, X. Guan, A. Komijani, A. Natarajan, and A. Hajimiri, "A 77-GHz phased-array transceiver with on-chip antennas in silicon: receiver and antennas," *IEEE J. Solid State Circuits*, vol. 41, no. 12, pp. 2795–2806, Dec. 2006.

[3] L. E. Larson, Ed., *RF and microwave circuit design for wireless communications,* Boston: Artech House, 1996.

[4] E. Seok, *et al.*, "Progress and challenges towards terahertz CMOS integrated circuits," *IEEE J. Solid-State Circuits*, vol. 45, no. 8, pp. 1554–1564, Aug. 2010.

[5] C. Mao, S. Sankaran, E. Seok, C. S. Nallani, and K. K. O, "Millimeter wave varistor mode schottky diode frequency doubler in CMOS," *IEEE Microw. Wirel. Compon. Lett.*, vol. 19, no. 3, pp. 173–175, Mar. 2009.

[6] O. Malyuskin, V. Fusco, and A. G. Schuchinsky, "Phase conjugating wire FSS lens," *IEEE Trans. Antennas Propag.*, vol. 54, no. 5, pp. 1399–1404, May 2006.

[7] P.-Y. Chen, C. Argyropoulos, and A. Alù, "Broadening the cloaking bandwidth with non-Foster metasurfaces," *Phys. Rev. Lett.*, vol. 111, no. 23, Dec. 2013.

[8] V. Rizzoli, A. Costanzo, D. Masotti, P. Spadoni, and A. Neri, "Prediction of the end-to-end performance of a microwave/RF link by means of nonlinear/ electromagnetic co-simulation," *IEEE Trans. Microw. Theory Techn.*, vol. 54, no. 12, pp. 4149–4160, Dec. 2006.

[9] Y. Bayram and J. L. Volakis, "Hybrid *S*-parameters for transmission line networks with linear/nonlinear load terminations subject to arbitrary excitations," *IEEE Trans. Microw. Theory Techn.*, vol. 55, no. 5, pp. 941–950, May 2007.

[10] J. E. Schutt-Aine and R. Mittra, "Scattering parameter transient analysis of transmission lines loaded with nonlinear terminations," *IEEE Trans. Microw. Theory Techn.*, vol. 36, no. 3, pp. 529–536, 1988.

[11] D. Winklestein, M. B. Steer, and R. Pomerleau, "Simulation of arbitrary transmission line networks with nonlinear terminations," *IEEE Trans. Circuits Syst.*, vol. 38, no. 4, pp. 418–422, 1991.

[12] I.-T. Chiang and W. C. Chew, "Fast real-time convolution algorithm for transients of nonlinearly-terminated microwave multiport circuits," *Microw. Opt. Technol. Lett.*, vol. 39, no. 4, pp. 280–282, Nov. 2003.

[13] A. Odabasioglu, M. Celik, and L. T. Pileggi, "PRIMA: passive reduced-order interconnect macromodeling algorithm," *IEEE Trans. Comput.-Aided Des. Integr. Circuits Syst.*, vol. 17, no. 8, pp. 645–654, Aug. 1998.

[14] A. C. Cangellaris and L. Zhao, “Model order reduction techniques for electromagnetic macromodelling based on finite methods,” *Int. J. Numer. Model. Electron. Netw. Devices Fields*, vol. 13, no. 2–3, pp. 181–197, Mar. 2000.

[15] R. Mohan *et al.*, “Causal reduced-order modeling of distributed structures in a transient circuit simulator,” *IEEE Trans. Microw. Theory Techn.*, vol. 52, no. 9, pp. 2207–2214, Sep. 2004.

[16] C. S. Saunders and M. B. Steer, “Passivity enforcement for admittance models of distributed networks using an inverse eigenvalue method,” *IEEE Trans. Microw. Theory Techn.*, vol. 60, no. 1, pp. 8–20, Jan. 2012.

[17] M. Kabir and R. Khazaka, “Macromodeling of distributed networks from frequency-domain data using the Loewner matrix approach,” *IEEE Trans. Microw. Theory Techn.*, vol. 60, no. 12, pp. 3927–3938, Dec. 2012.

[18] V. A. Thomas, M. E. Jones, M. Piket-May, A. Taflove, and E. Harrigan, “The use of SPICE lumped circuits as sub-grid models for FDTD analysis,” *IEEE Microw. Guid. Wave Lett.*, vol. 4, no. 5, pp. 141–143, 1994.

[19] P. Ciampolini, P. Mezzanotte, L. Roselli, and R. Sorrentino, “Accurate and efficient circuit simulation with lumped-element FDTD technique,” *IEEE Trans. Microw. Theory Techn.*, vol. 44, no. 12, pp. 2207–2215, 1996.

[20] K.-P. Ma, M. Chen, B. Houshmand, Y. Qian, and T. Itoh, “Global time-domain full-wave analysis of microwave circuits involving highly nonlinear phenomena and EMC effects,” *IEEE Trans. Microw. Theory Techn.*, vol. 47, no. 6, pp. 859–866, 1999.

[21] K. Guillouard, M. F. Wong, V. F. Hanna, and J. Citerne, “A new global time-domain electromagnetic simulator of microwave circuits including lumped elements based on finite-element method,” *IEEE Trans. Microw. Theory Techn.*, vol. 47, no. 10, pp. 2045–2049, 1999.

[22] R. Wang and J.-M. Jin, “A symmetric electromagnetic-circuit simulator based on the extended time-domain finite element method,” *IEEE Trans. Microw. Theory Techn.*, vol. 56, no. 12, pp. 2875–2884, Dec. 2008.

[23] B. Zhao, J. C. Young, and S. D. Gedney, “SPICE lumped circuit subcell model for the discontinuous Galerkin finite-element time-domain method,” *IEEE Trans. Microw. Theory Techn.*, vol. 60, no. 9, pp. 2684–2692, Sep. 2012.

[24] K. Aygun, B. C. Fischer, J. Meng, B. Shanker, and E. Michielssen, “A fast hybrid field-circuit simulator for transient analysis of microwave circuits,” *IEEE Trans. Microw. Theory Techn.*, vol. 52, no. 2, pp. 573–583, Feb. 2004.

[25] A. E. Yilmaz, J.-M. Jin, and E. Michielssen, “A parallel FFT accelerated transient field-circuit simulator,” *IEEE Trans. Microw. Theory Techn.*, vol. 53, no. 9, pp. 2851–2865, Sep. 2005.

[26] C.-C. Huang and T.-H. Chu, "Analysis of wire scatterers with nonlinear or time-harmonic loads in the frequency domain," *IEEE Trans. Antennas Propag.*, vol. 41, no. 1, pp. 25–30, 1993.

[27] D. L. Dault, B. Shanker, A. D. Baczewski, and P. Chahal, "Modeling of dense coupled periodic and non-periodic electromagnetic-circuit systems using harmonic balance and fast solvers," in *Proceedings URSI/USNC Radio Science Meeting*, 2011.

[28] A. E. Yilmaz, J.-M. Jin, and E. Michielssen, "A TDIE-based asynchronous electromagnetic-circuit simulator," *IEEE Microw. Wirel. Compon. Lett.*, vol. 16, no. 3, pp. 122–124, Mar. 2006.

[29] H. Bagci, A. E. Yilmaz, and E. Michielssen, "An FFT-accelerated time-domain multiconductor transmission line simulator," *IEEE Trans. Electromagn. Compat.*, vol. 52, no. 1, pp. 199–214, Feb. 2010.

[30] C. Yang and V. Jandhyala, "Combined circuit-electromagnetic simulation using multiregion time domain integral equation scheme," *IEEE Trans. Electromagn. Compat.*, vol. 48, no. 1, pp. 2–9, Feb. 2006.

[31] S. Grivet-Talocia, "On passivity characterization of symmetric rational macromodels," *IEEE Trans. Microw. Theory Techn.*, vol. 58, no. 5, pp. 1238–1247, May 2010.

[32] R. J. Gilmore and M. B. Steer, "Nonlinear circuit analysis using the method of harmonic balance—a review of the art. Part I. Introductory concepts," *Int. J. Microw. Millim.-Wave Comput.-Aided Eng.*, vol. 1, no. 1, pp. 22–37, 1991.

[33] J. F. Sevic, M. B. Steer, and A. M. Pavio, "Nonlinear analysis methods for the simulation of digital wireless communication systems," *Int. J. Microw. Millim.-Wave Comput.-Aided Eng.*, vol. 6, no. 3, pp. 197–216, 1996.

[34] K. Kundert, "Simulation methods for RF integrated circuits," in *Proc. IEEE/ACM international conference on Computer-aided design*, 1997, pp. 752–765.

[35] G. Kaur and A. E. Yilmaz, "On the performance of envelope-tracking surface-integral equation solvers," in *Proc. IEEE Intl. Antennas Propag. Symp.*, 2011, pp. 2716–2719.

[36] L. Chua and A. Ushida, "Algorithms for computing almost periodic steady-state response of nonlinear systems to multiple input frequencies," *IEEE Trans. Circuits Syst.*, vol. 28, no. 10, pp. 953–971, 1981.

[37] V. Rizzoli, C. Cecchetti, A. Lipparini, and F. Mastri, "General-purpose harmonic balance analysis of nonlinear microwave circuits under multitone excitation," *IEEE Trans. Microw. Theory Techn.*, vol. 36, no. 12, pp. 1650–1660, 1988.

[38] A. Mohan and D. S. Weile, "A hybrid method of moments-marching on in time method for the solution of electromagnetic scattering problems," *IEEE Trans. Antennas Propag.*, vol. 53, no. 3, pp. 1237–1242, Mar. 2005.

[39] J. D. Pursel and P. M. Goggans, "A finite-difference time-domain method for solving electromagnetic problems with bandpass-limited sources," *IEEE Trans. Antennas Propag.*, vol. 47, no. 1, pp. 9–15, 1999.

[40] C. Ma and Z. Chen, "Stability and numerical dispersion analysis of CE-FDTD method," *IEEE Trans. Antennas Propag.*, vol. 53, no. 1, pp. 332–338, Jan. 2005.

[41] H. Rao, R. Scarmozzino, and R. M. Osgood, "An improved ADI-FDTD method and its application to photonic simulations," *IEEE Photonics Technol. Lett.*, vol. 14, no. 4, pp. 477–479, 2002.

[42] K.-Y. Jung, F. L. Teixeira, S. G. Garcia, and R. Lee, "On numerical artifacts of the complex envelope ADI-FDTD Method," *IEEE Trans. Antennas Propag.*, vol. 57, no. 2, pp. 491–498, Feb. 2009.

[43] Y. Wang and T. Itoh, "Envelope-finite-element (EVFE) technique-a more efficient time-domain scheme," *IEEE Trans. Microw. Theory Techn.*, vol. 49, no. 12, pp. 2241–2247, 2001.

[44] H.-P. Tsai, Y. Wang, and T. Itoh, "Efficient analysis of microwave passive structures using 3-D envelope-finite element (EVFE)," *IEEE Trans. Microw. Theory Techn.*, vol. 50, no. 12, pp. 2721–2727, Dec. 2002.

[45] D. Sharrit, "New method of analysis of communication systems," presented at the *MTT-S WMFA: Nonlinear CAD Workshop,* 1996.

[46] V. Rizzoli, A. Neri, and F. Mastri, "A modulation-oriented piecewise harmonic-balance technique suitable for transient analysis and digitally modulated signals," in *Proc. European Microw. Conf.* 1996, pp. 546–550.

[47] E. Ngoya and R. Larcheveque, "Envelop transient analysis: a new method for the transient and steady state analysis of microwave communication circuits and systems," in *Proc. IEEE MTT-S Intl. Microw. Symp.*, 1996, vol. 3, pp. 1365–1368.

[48] V. Rizzoli, A. Neri, F. Mastri, and A. Lipparini, "Modulation-oriented harmonic balance based on Krylov-subspace methods," in *Proc. IEEE MTT-S Intl. Microw. Symp.*, 1999, vol. 2, pp. 771–774.

[49] H.-S. Yap, "Designing to digital wireless specifications using circuit envelope simulation," in *Proc. Asia Pacific Microw. Conf.*, 1997, vol. 1, pp. 173–176.

[50] N. B. Carvalho, J. C. Pedro, W. Jang, and M. B. Steer, "Nonlinear RF circuits and systems simulation when driven by several modulated signals," *IEEE Trans. Microw. Theory Techn.*, vol. 54, no. 2, pp. 572–579, Feb. 2006.

[51] S. A. Maas, *Nonlinear microwave and RF circuits*, 2nd ed. Boston, MA: Artech House, 2003.

[52] G. Kaur and A. E. Yilmaz, "Envelope-tracking adaptive integral method for band-pass transient scattering analysis," *IEEE Trans. Antennas Propag.*, vol. 63, no. 5, pp. 2215–2227, May 2015.

[53] A. E. Yilmaz, J.-M. Jin, and E. Michielssen, "Time domain adaptive integral method for surface integral equations," *IEEE Trans. Antennas Propag.*, vol. 52, no. 10, pp. 2692–2708, Oct. 2004.

[54] E. Bleszynski, M. Bleszynski, and T. Jaroszewicz, "AIM: Adaptive integral method for solving large-scale electromagnetic scattering and radiation problems," *Radio Sci.*, vol. 31, no. 5, pp. 1225–1251, Sep. 1996.

[55] T. Malas and A. E. Yilmaz, "Near-field preconditioners for large-scale AIM-accelerated bioelectromagnetics simulations," in *Proc. USNC/URSI Radio Science meeting*, 2011.

[56] T. Malas and L. Gürel, "Accelerating the multilevel fast multipole algorithm with the sparse-approximate-inverse (SAI) preconditioning," *SIAM J. Sci. Comput.*, vol. 31, no. 3, pp. 1968–1984, Jan. 2009.

[57] L. Gürel and T. Malas, "Iterative near-field preconditioner for the multilevel fast multipole algorithm," *SIAM J. Sci. Comput.*, vol. 32, no. 4, pp. 1929–1949, Jan. 2010.

[58] N.-W. Chen, B. Shanker, and E. Michielssen, "Integral-equation-based analysis of transient scattering from periodic perfectly conducting structures," *IEE Proc.-Microw. Antennas Propag.*, vol. 150, no. 2, pp. 120–124, 2003.

[59] D. S. Weile, G. Pisharody, N.-W. Chen, B. Shanker, and E. Michielssen, "A novel scheme for the solution of the time-domain integral equations of electromagnetics," *IEEE Trans. Antennas Propag.*, vol. 52, no. 1, pp. 283–295, Jan. 2004.

[60] B. C. Fischer, *Incorporation of Arbitrary Linear and Nonlinear Lumped Circuits into a Fast Time-domain Integral Equation Solver*. University of Illinois at Urbana-Champaign, 2002.

[61] L. W. Nagel, *SPICE2: A Computer Program to Simulate Semiconductor Circuits*. Electronics Research Laboratory, College of Engineering, University of California, 1975.

[62] J.-P. Curty, N. Joehl, F. Krummenacher, C. Dehollain, and M. J. Declercq, "A model for μ-power rectifier analysis and design," *IEEE Trans. Circuits Syst. Regul. Pap.*, vol. 52, no. 12, pp. 2771–2779, Dec. 2005.

[63] G. Massobrio and P. Antognetti, *Semiconductor device modeling with SPICE*. New York: McGraw-Hill, 1998.

[64] C.-N. Kuo, B. Houshmand, and T. Itoh, "Full-wave analysis of packaged microwave circuits with active and nonlinear devices: An FDTD approach," *IEEE Trans. Microw. Theory Techn.*, vol. 45, no. 5, pp. 819–826, 1997.

[65] G. Burke, A. Poggio, J. Logan, and J. Rockway, "NEC-Numerical electromagnetics code for antennas and scattering," in *Proc. IEEE. Antennas Propag. Soc. Intl. Symp.*, 1979, vol. 17, pp. 147–150.

[66] D. R. Wilton and N. J. Champagne, "Evaluation and integration of the thin wire kernel," *IEEE Trans. Antennas Propag.*, vol. 54, no. 4, pp. 1200–1206, Apr. 2006.

[67] G. Kaur and A. E. Yilmaz, "Accuracy-efficiency tradeoff of temporal basis functions for time-marching solvers," *Microw. Opt. Technol. Lett.*, vol. 53, no. 6, pp. 1343–1348, Jun. 2011.

[68] W. H. Press, Ed., *FORTRAN Numerical recipes*, 2nd ed. Cambridge [England] ; New York: Cambridge University Press, 1996.

[69] R. W. Ziolkowski and E. Heyman, "Wave propagation in media having negative permittivity and permeability," *Phys. Rev. E*, vol. 64, no. 5, Oct. 2001.

[70] O. Malyuskin, V. Fusco, and A. G. Schuchinsky, "Microwave Phase Conjugation Using Nonlinearly Loaded Wire Arrays," *IEEE Trans. Antennas Propag.*, vol. 54, no. 1, pp. 192–203, Jan. 2006.

[71] S. Rao, D. Wilton, and A. Glisson, "Electromagnetic scattering by surfaces of arbitrary shape," *IEEE Trans. Antennas Propag.*, vol. 30, no. 3, pp. 409–418, May 1982.

[72] D. Schaubert, D. Wilton, and A. Glisson, "A tetrahedral modeling method for electromagnetic scattering by arbitrarily shaped inhomogeneous dielectric bodies," *IEEE Trans. Antennas Propag.*, vol. 32, no. 1, pp. 77–85, Jan. 1984.

[73] Y. H. Lo, L. J. Jiang, and W. C. Chew, "Finite-width feed and load Models," *IEEE Trans. Antennas Propag.*, vol. 61, no. 1, pp. 281–289, Jan. 2013.

[74] W. Ding, G. Wang, F. Liang, and B. Yuan, "An enhanced gap source model," *IEEE Trans. Antennas Propag.*, vol. 61, no. 3, pp. 1266–1272, Mar. 2013.

[75] A. Brandt, "Multilevel computations of integral transforms and particle interactions with oscillatory kernels," *Comput. Phys. Commun.*, vol. 65, no. 1–3, pp. 24–38, Apr. 1991.

[76] K. Yang and A. E. Yilmaz, "Comparison of precorrected FFT/adaptive integral method matching schemes," *Microw. Opt. Technol. Lett.*, vol. 53, no. 6, pp. 1368–1372, Jun. 2011.

[77] A. E. Yilmaz, J.-M. Jin, and E. Michielssen, "Analysis of low-frequency electromagnetic transients by an extended time-domain adaptive integral method," *IEEE Trans. Adv. Packag.*, vol. 30, no. 2, pp. 301–312, May 2007.

[78] J. R. Phillips and J. K. White, "A precorrected-FFT method for electrostatic analysis of complicated 3-D structures," *IEEE Trans. Comput.-Aided Des. Integr. Circuits Syst.*, vol. 16, no. 10, pp. 1059–1072, 1997.

[79] Q.-X. Chu, Y.-P. Lau, and F.-Y. Chang, "Transient analysis of microwave active circuits based on time-domain characteristic models," *IEEE Trans. Microw. Theory Techn.*, vol. 46, no. 8, pp. 1097–1104, 1998.

[80] H. Holter and H. Steyskal, "Infinite phased-array analysis using FDTD periodic boundary conditions-pulse scanning in oblique directions," *IEEE Trans. Antennas Propag.*, vol. 47, no. 10, pp. 1508–1514, 1999.

[81] F. Capolino and L. B. Felsen, "Time-domain green's function for an infinite sequentially excited periodic planar array of dipoles," *IEEE Trans. Antennas Propag.*, vol. 51, no. 2, pp. 160–170, Feb. 2003.

[82] J. Gao and B. Shanker, "Causality trick and the analytical signal formulation of the time domain periodic Green's function," in *Proc. IEEE Antennas Propag. Soc. Intl. Symp.*, 2006, pp. 2839–2842.

[83] A. E. Yilmaz, D. S. Weile, B. Shanker, Jian-Ming Jin, and E. Michielssen, "Fast analysis of transient scattering in lossy media," *IEEE Antennas Wirel. Propag. Lett.*, vol. 1, no. 1, pp. 14–17, 2002.

[84] F. Capolino and L. B. Felsen, "Frequency-and time-domain Green's functions for a phased semi-infinite periodic line array of dipoles," *IEEE Trans. Antennas Propag.*, vol. 50, no. 1, pp. 31–41, 2002.

[85] Z. Hao, S. Saadat, and H. Mosallaei, "FDTD-SPICE for characterizing metamaterials integrated with electronic circuits," *Int. J. Antennas Propag.*, vol. 2012, pp. 1–7, 2012.

[86] P. M. Morse and H. Feshbach, *Methods of theoretical physics*. Boston, Mass: McGraw-Hill, 1999.

[87] J. Aronsson, M. Shafieipour, and V. Okhmatovski, "Study of preconditioners for RWG MoM analysis of large scale scatterers containing junctions with open surfaces and delta-gap voltage sources," in *Proc. Applied Computational Electromagnetics Soc. Conf.*, 2012.

[88] A. Mohan and D. S. Weile, "Convergence properties of higher order modeling of the cylindrical wire kernel," *IEEE Trans. Antennas Propag.*, vol. 55, no. 5, pp. 1318–1324, May 2007.

[89] P. J. Davies, B. P. Rynne, and B. Zubik-Kowal, "The time domain integral equation for a straight thin-wire antenna with the reduced kernel is not well-posed," *IEEE Trans. Antennas Propag.*, vol. 50, no. 8, pp. 1165–1166, Aug. 2002.

VITA

Vivek Subramanian finished his Bachelor of Engineering degree with major in Electronics and Communication Engineering at Sri Krishna College of Engineering and Technology, Coimbatore, India in 2005. He completed his Master of Technology degree from Indian Institute of Technology, Kharagpur, India in 2007. After working for two years at ST Microelectronics as a Design Engineer at STMicroelectronics, Noida, India, he started pursuing his PhD degree at The University of Texas at Austin in 2009.

Email: vivek.s@utexas.edu

This dissertation was typed by Vivek Subramanian.